

GRADUATE AERONAUTICAL LABORATORIES CALIFORNIA INSTITUTE OF TECHNOLOGY

RESEARCH IN HYPERVELOCITY GASDYNAMICS

H. G. Hornung and B. Sturtevant

2 February 1996

Final Technical Report

Grant F49610-92-J-0110

Approved for public release; distribution is unlimited

Prepared for

AIR FORCE OFFICE OF SCIENTIFIC RESEARCH

110 Duncan Avenue, Suite B115, Bolling AFB DC 20332-0001

Firestone Flight Sciences Laboratory

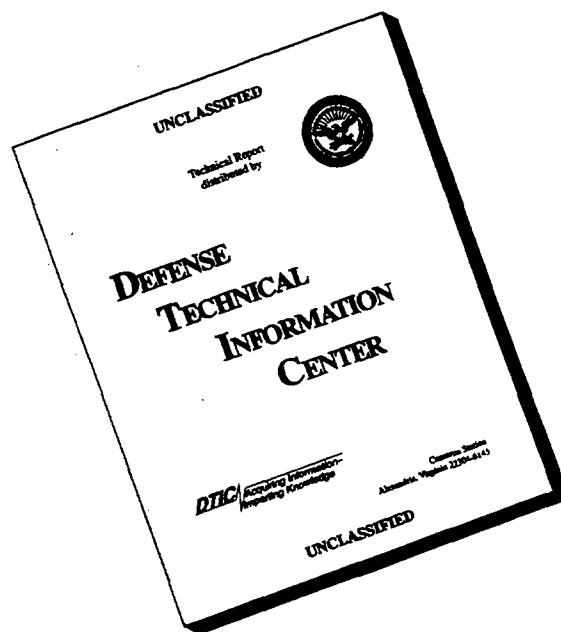
Guggenheim Aeronautical Laboratory

Karman Laboratory of Fluid Mechanics and Jet Propulsion

Pasadena

19960408 133

DISCLAIMER NOTICE



**THIS DOCUMENT IS BEST
QUALITY AVAILABLE. THE
COPY FURNISHED TO DTIC
CONTAINED A SIGNIFICANT
NUMBER OF PAGES WHICH DO
NOT REPRODUCE LEGIBLY.**

REPORT DOCUMENTATION PAGE			Form Approved OMB No. 0704-0188	
Public reporting burden for this collection of information is estimated to average 1 hour per response, including the time for reviewing instructions, searching existing data sources, gathering and maintaining the data needed, and completing and reviewing the collection of information. Send comments regarding this burden estimate or any other aspect of this collection of information, including suggestions for reducing this burden, to Washington Headquarters Services, Directorate for Information Operations and Reports, 1215 Jefferson Davis Highway, Suite 1204, Arlington, VA 22202-4302, and to the Office of Management and Budget, Paperwork Reduction Project (0704-0188), Washington, DC 20503.				
1. AGENCY USE ONLY (Leave blank)		2. REPORT DATE 2 February 1996		3. REPORT TYPE AND DATES COVERED Final Technical Rept. 11/15/95-8/31/95
4. TITLE AND SUBTITLE (U) Research in Hypervelocity Gasdynamics			5. FUNDING NUMBERS PE - PR - SA - G - F49610-92-J-0110	
6. AUTHOR(S) H. G. Hornung and B. Sturtevant Appendix B & C				
7. PERFORMING ORGANIZATION NAME(S) AND ADDRESS(ES) Graduate Aeronautical Laboratories California Institute of Technology 1201 E. California Blvd. Pasadena, CA 91125			AFOSR-TR-96 0143	
9. SPONSORING/MONITORING AGENCY NAME(S) AND ADDRESS(ES) AFOSR/NA 110 Duncan Avenue, Suite B115 Bolling AFB DC 20332-0001 Dr. Len Sakell			10. SPONSORING/MONITORING AGENCY REPORT NUMBER NA 19960408 133	
11. SUPPLEMENTARY NOTES				
12a. DISTRIBUTION/AVAILABILITY STATEMENT Approved for public release; distribution is unlimited			12b. DISTRIBUTION CODE	
13. ABSTRACT (Maximum 200 words) The following important results were obtained from investigations of chemically reacting blunt-body flows and of shock wave interactions in hypervelocity flow: <ul style="list-style-type: none"> • A new view of the binary scaling concept resulted from experimental and theoretical work on flow over spheres, in terms of two dimensionless parameters. • The evolution of the vorticity generated by a curved shock wave could be visualized with resonant enhancement of streak lines. • The effect of recombination in flow along a streamline after a curved shock was explained. • Previous predictions of greatly enhanced heat flux by real-gas effects in shock-on-shock interactions were not borne out. • The study provided extensive corroboration of the computed free-stream conditions in the free-piston shock tunnel T5. • A number of improvements of shock tunnel technology were made, especially regarding diaphragm manufacture, nozzle throat material, and computation of the processes during operation. • Improved diagnostic techniques were generated, including low-noise coaxial thermocouple gauges and inexpensive high-quality holographic interferometry. 				
14. SUBJECT TERMS hypervelocity flow, shock wave, shock interaction, heat transfer, vorticity, dissociation			15. NUMBER OF PAGES 485	
			16. PRICE CODE	
17. SECURITY CLASSIFICATION OF REPORT Unclassified	18. SECURITY CLASSIFICATION OF THIS PAGE Unclassified	19. SECURITY CLASSIFICATION OF ABSTRACT Unclassified	20. LIMITATION OF ABSTRACT UL	

RESEARCH IN HYPERVELOCITY GASDYNAMICS

H. G. Hornung and B. Sturtevant
California Institute of Technology
Pasadena, CA 91125

2 February 1996

Final Technical Report

AFOSR Grant F 49620-92-J-0110

Approved for public release; distribution is unlimited

Prepared for

AIR FORCE OFFICE OF SCIENTIFIC RESEARCH

110 Duncan Avenue, Suite B115, Bolling AFB DC 20332-0001

1. Introduction

The aim of the research was to study the high-enthalpy real-gas effects in the important hypervelocity problems concerned with the influence of shock-generated vorticity in blunt-body flows and shock boundary layer interaction. At the outset of the work, the new free-piston shock tunnel T5 had just been completed, providing a unique opportunity for these investigations. The grant was instrumental in getting the research in T5 started and to provide the first results on these problems in the high-enthalpy regime. It led to a significantly larger research effort funded by the AFOSR as part of a URI Grant.

The impact made by presentations of early results of the work at the 19th International Symposium on Shock Waves at Marseille, France, in 1993, helped to enable the PI's to make a successful case for hosting the 20th International Symposium at Caltech. The AFOSR supported the 20th Symposium through an increase of the total amount of the grant. A separate report on the Symposium will be submitted in the summer of 1996.

2. Achievements

The results of the research have all been documented in publications, conference papers and theses. The publications and conference papers are bound together in Appendix A, and each of the theses is attached as a separate Appendix. The major achievements of the research are summarized in this section.

2.1 Chemically reacting blunt-body flows

An experimental, theoretical and numerical investigation of the flow of nitrogen, air and carbon dioxide over spheres, conducted with different gases at conditions ranging from the perfect-gas regime to near chemical equilibrium led to the following significant results:

1. Stagnation-point heat flux measurements that provide indirect confirmation of the reservoir enthalpy of the flow in the facility over the whole range of reservoir enthalpy. Values ranging up to 120 MW/m^2 were recorded, see [1-6].
2. A new view of the concept of binary scaling in terms of two dimensionless parameters, substantiated through application of differential interferometry experimentally and to numerical computations, see [4].
3. Extensive validation of Candler's reacting flow code, see [1],[2],[4].

4. Computation and first visualization of vorticity generated by curved shock waves in flow over a sphere, see [5].
5. Further development of the theoretical analysis of the flow along a streamline after a curved shock in reacting flow, including recombination reactions, see [1,3].

Techniques developed in this work and in the work described in Section 2.2 led to significant improvement of the results obtained in a study of high-enthalpy transitional boundary layers not directly funded by this grant. For that reason the funding is acknowledged in publications resulting from the study, see [8]. From mid-1993 this work was co-funded by AFOSR grant F49620-93-1-0338.

2.2 Shock wave interactions in hypervelocity flow

The effects of dissociation on the large heat flux induced by the intersection of an oblique shock with a blunt body bow shock was investigated experimentally in T5. Extensive data were obtained at three selected conditions, spanning the enthalpy range of T5 from the perfect-gas regime to rapidly dissociating conditions. This is now an extensive data base giving detailed flow fields in the form of high-resolution interferograms, and surface heat flux distributions from newly developed thermocouple heat flux gauges. The main conclusions were:

1. Previous predictions of greatly enhanced heat flux by real-gas effects were not borne out, see [11].
2. Interference heating in high-enthalpy flows is essentially the same as in low-enthalpy flows, see [11, 12, 13]. These observations greatly reduce the design constraints for hypervelocity vehicles.
3. Good agreement between computed and measured stagnation point fringe shift and heat flux provides further corroboration of the free-stream conditions of the facility, see [11].

2.3 Improvements to high-enthalpy shock tunnel technology

During the course of the project, a number of developments in the technology of shock tunnel operation could be made. The successful conclusion of the work critically depended on these improvements in the following cases;

1. Design and construction of a diaphragm indentation machine that makes the burst pressure more repeatable, reduces the cost from \$180 to \$20 per diaphragm, and reduces the debris lost from the diaphragm to ~ 50 mg.
2. Development of resonantly enhanced shadowgraphy and interferometry for visualization of flows with small optical path differences, see [8].
3. Nozzle throat material technology enabling operation up to 22 MJ/kg at 90 MPa without melting of throats.
4. Development of a computer code for optimization of T5 operation.
5. Design and construction of a second nozzle and a lighter piston for low pressure operation, see [10].

3. Personnel associated with the research

1. Hans G. Hornung, Kelly Johnson Professor of Aeronautics, GALCIT Director
2. Bradford Sturtevant, Hans W. Liepmann Professor of Aeronautics
3. Simon Sanderson, Graduate Research Assistant
4. Chih-Yung Wen, Graduate Research Assistant
5. Bahram Valiferdowsi, Staff Engineer

4. Degrees earned by participating personnel

1. Chih-Yung Wen, Ph. D., 1994
2. Simon Sanderson, Ph. D., 1995, Ballhaus Prize for best thesis at GALCIT

5. Publications resulting from the work

Note: The following publications, with the exception of [1] and [11], are included in this document as Appendix A. [1] and [11] form part of this report in the form of two separately bound volumes, Appendix B and Appendix C.

- [1] Wen, C. 1994 "Hypervelocity flow over spheres." Ph. D. Thesis, California Institute of Technology, Pasadena.
- [2] Hornung, H. G., Wen C., and Candler G. 1994, "Hypervelocity flow over spheres." *Acta Mechanica* [Suppl. 4]: 163-170.
- [3] Wen C.-Y. and Hornung H. G. 1993 "Nonequilibrium recombination after a curved shock" *Proceedings, First Pacific International Conference on Aerospace Science and Technology*, December, 1993, National Cheng-Kung University, Tainan, Taiwan, pp.639-646.
- [4] Wen, C.-Y. and Hornung, H. G. 1995, "Nonequilibrium dissociating flow over spheres", *J. Fluid Mech.* **299**, 1995, 389-405.
- [5] Wen C.-Y. and Hornung, H. G. 1995, "Experiments on hypervelocity dissociating flow over spheres," in *Shock Waves @ Marseille* Vol. I, ed R. Brun, L. Z. Dumitrescu, Springer Verlag, pp. 223-228.
- [6] Hornung, H.G., Wen, C.Y. and Germain, P., "Hypervelocity Flow Simulation" 1994, in *Mechanics USA 1994*, ed. A. S. Kobayashi, Appl. Mech. Rev. **47** pp. S14-S19.
- [7] Rock, S. G., Candler G. V. and Hornung, H.G. "Analysis of thermochemical nonequilibrium models for carbon-dioxide flows." *AIAA J.* **31**, (12): 2255-2262.
- [8] Germain P., Cummings E. and Hornung H. G., 1993 "Transition on a sharp cone at high enthalpy; new measurements in the shock tunnel T5 at GALCIT." AIAA 93-0343, Reno.
- [9] Hornung, H. 1993, "Experimental hypervelocity flow simulation, needs, achievements and limitations." Invited presentation, *Proceedings, First Pacific International Conference on Aerospace Science and Technology*, December, 1993, National Cheng-Kung University, Tainan, Taiwan pp. 1-10.
- [10] Hornung H. G., Cummings E. B., Germain P., Sanderson S. R., Sturtevant B., and Wen C.-Y. 1994 "Recent results from hypervelocity research in T5," AIAA 94-2523, Colorado Springs.

- [11] Sanderson S. R. 1995 "Shock wave interaction in hypervelocity flow" Ph. D. Thesis, California Institute of Technology, Pasadena.
- [12] Sanderson S. R. and Sturtevant B. 1995, "Shock wave interactions in hypervelocity flow," in *Shock Waves @ Marseille* Vol. I, ed R. Brun, L. Z. Dumitrescu, Springer Verlag, pp. 69-74.
- [13] Sanderson S. R. and Sturtevant B. 1996 "Shock-interference heating in hypervelocity flow" Proceedings of the 20th International Symposium on Shock Waves, Pasadena July 1995, to be published.

Appendix A

Publications listed in Section 5, except [1] and [11]

Part 4: Hypersonic Flow

Hypervelocity flow over spheres

H. Hornung, C. Wen, Pasadena, California, and G. Candler, Minneapolis, Minnesota

Summary. Some aspects of the principle of binary scaling of hypervelocity flows with chemical reactions are discussed and tested both numerically and experimentally. The experiments, obtained in a new free-piston shock tunnel, show the value and limitations of binary scaling in very good agreement with the numerical computations. The use of spherical models eliminates end-effect problems previously encountered with cylindrical models. Global quantities, such as the bow shock stand-off distance, follow binary scaling very well. The results include differential interferograms and surface heat transfer measurements of nitrogen, air and carbon dioxide flows.

1 Introduction

The experimental study of the field of high-enthalpy real-gas dynamics, as it applies to transport into and back from space through planetary atmospheres, requires facilities that are at the upper end of the scale of what is possible at universities. The reason for this becomes clear from the features of the problem: Take the atmosphere of earth, where the orbital speed is 8 km/s, and the critical heating rate, the most serious concern of designers, occurs at approximately 6 km/s. The thermal energy per unit mass in the stagnation region of a body traveling at this speed is 18 MJ/kg. This may be compared to the characteristic energies of vibration and dissociation of the molecular components of air:

$$D_{N_2} = 33.6 \text{ MJ/kg} \quad E_{vN_2} = 0.992 \text{ MJ/kg}$$

$$D_{O_2} = 15.5 \text{ MJ/kg} \quad E_{vO_2} = 0.579 \text{ MJ/kg}$$

$$D_{NO} = 20.9 \text{ MJ/kg} \quad E_{vNO} = 0.751 \text{ MJ/kg}.$$

It is clear that very substantial chemical activity will take place and the vibrational energy may often be considered to be in equilibrium with the translational energy. Because of the complex idiosyncrasies of the substance air at such high specific energy, it is not possible to simulate them with other gases, and we are necessarily forced to reproduce the actual flow speed that the body sees.

A second feature of the problem is that in many parts of the flow field around a body, the chemical reactions occur at speeds which are comparable to the local flow speed, so that it is necessary to study not only equilibrium high-enthalpy effects but also those that arise because of the finiteness of the chemical reaction rates. These, by virtue of the flow speed, introduce characteristic lengths into the problem, which depend on the properties of the gases as well as on the flow variables. Two kinds of chemical reactions may broadly be distinguished: Binary and ternary reactions, for which the characteristic lengths vary as the inverse of the density and as the inverse of the square of the density respectively. In a simulation, where one wishes to reproduce

the ratio of body size to characteristic chemical length, it is therefore necessary to reproduce

$$\rho L, \quad \text{or} \quad \rho^2 L$$

depending on whether binary or ternary reactions are dominant in the phenomenon of interest. It is not possible to simulate situations involving both types correctly except at full scale.

Binary reactions dominate the features of blunt body flows, so that for the simulation of the important problems that occur there, we see that the scale of a facility has a lower bound that is dictated by the pressure at which one is prepared to operate. If the scaling ratio (model scale/prototype scale) is 1:100, the density scaling ratio has to be 100:1. Since the temperature has to be simulated correctly (assured by correct speed), the pressure also has to be 100 times that of the real flow. If the pressure is limited by one or more of strength, safety, noise, environment, all of which are concerns at universities, the size of the facility has a lower bound.

The above considerations formed the core of the constraints of the design of a new facility at GALCIT which had the specific aim of studying the fundamental features of high-enthalpy reacting flows. The facility was named T5, because it built heavily on the experience gained in the Australian facilities T1 to T4, which, like T5, use the principle of free-piston adiabatic compression of the driver gas of a shock tunnel to achieve the high shock speeds and densities required to generate the high enthalpy and reaction scaling. The shock tunnel has the additional essential feature that the test duration is sufficiently short to avoid destruction of the machine by melting. A more detailed description of T5 and its performance envelope, flow quality and repeatability may be found in Hornung [1]. The largest facility of this type has been completed in 1992 at Göttingen, see Eitelberg [2].

The features of hypervelocity blunt body flows and of the limits of binary scaling have been studied extensively theoretically. However, only very few experimental results are available. The most detailed of these are the interferometric studies of cylinder flows by Hornung [3]. The reason for the choice of cylinders in those experiments was that the density achievable in the facility used (T3) was insufficient to get good fringe resolution in optical interferograms of flows over spheres. The difficulty with "two-dimensional" flows is that they are an idealization that does not exist in reality. In the blunt body problem, the end effects on cylinder flows manifest themselves in interferograms in just the same manner as the finite-rate effects one wishes to study, and may therefore obscure them seriously. The size and density achievable in T5 has now extended the available parameter range sufficiently to avoid this problem by studying the axisymmetric situation, i.e., by using spheres as models. The following pages present the first steps of an investigation in T5, and of an accompanying theoretical effort, towards gaining more insight into the blunt body problem and the limits of binary scaling.

At the same time, the development of numerical methods for the computation of blunt body flow fields has become very much quicker since the 1970's, so that even interferograms of three-dimensional chemically reacting flows can be computed with reasonable speeds, see e.g., Rock et al. [4]. For laminar flow, the viscous case is also accessible, so that heating rates too may be compared with theoretical models, see e.g. Candler [5]. The experiments with spheres to be described in the following pages therefore are equipped with heat transfer gauges and differential interferometry for the quantitative exploration of the flow field and comparison with computation. Some comparisons of theoretical and experimental results were also made by Macrossan [6] who showed that the simple model of Hornung [7] (which is based on matched asymptotic expansions of the near-equilibrium case at relatively small densities, where the recombination rate may be neglected) has restricted applicability, especially in the tunnel, where the recombination rate is too high if binary scaling is applied.

2 Design of the experiment

Because of the relative ease with which the flow may be computed, a computational exploration of the parameter space affords an excellent method of designing an experiment. With this in mind, the inviscid reacting flow over a sphere was computed with the Candler code. This program uses a finite-volume method and is described in detail in Candler [5]. The flow field is described by coupled partial differential equations for the conservation of species, mass, mass-averaged momentum, vibrational energy of each diatomic species and total energy. The steady-state solution to these fully coupled equations is obtained for different gases characterized by a two-temperature model using an implicit Gauss-Seidel line relaxation technique. The success of this code in reproducing in great detail those experimental results that are available in the form of field measurements is impressive, and extensive documentation of examples exists. The code is actually set up for viscous flow, but was used in the context of this section in the inviscid form. Figure 1 shows an example of such a computation for the case of a nitrogen flow, in the form of the density field and of the infinite-fringe interferogram that would be observed in such a flow. As may be seen, a large number of fringes would be observed, so that even a relatively insensitive differential interferogram would give good quantitative resolution of the flow field. The case shown corresponds to a representative condition achievable in T5.

Computations of this type may be used to plot the dimensionless shock stand-off distance, for example, and this is shown in a plot of this quantity against the dimensionless reaction rate at a point immediately downstream of the normal shock. This is shown in Fig. 2 for the range of values achievable in the tunnel. In the regime where binary scaling is applicable, this curve should not separately depend on q and d , but only on their product. As may be seen from the scatter in the diagram, this is not quite the case, but the stand-off distance does not seem to be strongly affected by the failure of binary scaling.

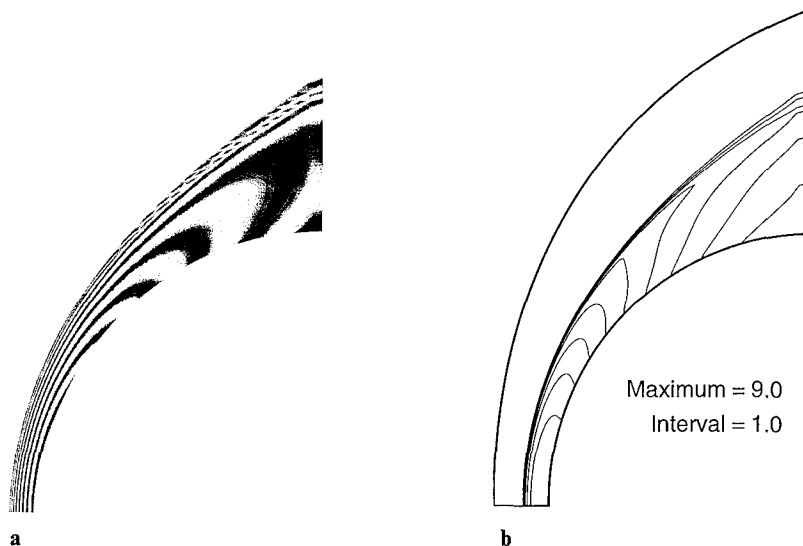


Fig. 1. Result of a computation of the flow field over a sphere. Free stream conditions: 5.08 km/s, nitrogen, 0.04 kg/m³, 16.56 MJ/kg. **a** Infinite fringe interferogram constructed from the numerical solution. **b** Lines of constant density. The numbers on the right indicate the density values as multiples of the free-stream density. The border of the diagram on the right is the edge of the computational domain. The glitch at the right is an artefact of the interpolation routine

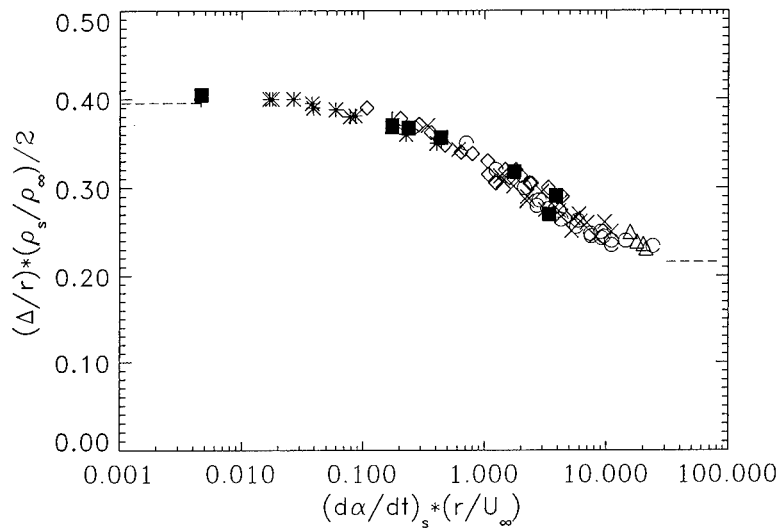


Fig. 2. Stand-off distance variation with reaction rate parameter. The abscissa is the reaction rate parameter, defined as the dissociation rate immediately after the shock scaled by sphere radius and flow speed. The ordinate is the dimensionless stand-off distance scaled by the density ratio at the shock. The square symbols in this diagram represent experimental results in T5, while the other symbols are computational results. The asymptotes shown are for equilibrium and frozen flow respectively

A second, more sensitive test is to plot the reaction rates against the distance along a streamline. If the model of Hornung [7] applies, the reaction stops while the gas is still dissociating, because of the temperature drop brought about by the curvature of the shock. As had been shown by Macrossan [6], this assumption fails in the higher density flows considered here. This may also be seen in Fig. 3, where dissociation rate, recombination rate and dissociation fraction are shown along three streamlines in a nitrogen flow. Clearly, the recombination plays an important role, especially for the streamlines that cross the shock close to the axis. This necessarily leads to failure of binary scaling, although the effect on global variables may be small.

The computations led to choices for the experiment. Since the density of the flow can be varied by changing the reservoir pressure, a number of different-size spheres were made, each equipped with four heat-flux measuring devices (thermocouples that record the time-dependent temperature of the surface of a material with known thermal properties). A series of conditions at different pressures and specific reservoir enthalpies in three different gases were planned: Nitrogen, air and carbon dioxide. The latter gas has the feature that the energy consumed by vibrational excitation and dissociation can reach a considerably larger fraction of the kinetic energy of the flow so that the real-gas effects are more dramatic, than in the case of nitrogen.

3 Experimental results

The experiments are still ongoing at the time of writing, so that the range of parameters studied is still incomplete, and the quality of the interferograms needs improvement. The first interest was the high-density range, where near-equilibrium cases could be studied in contrast to the situation in T3, so that this presentation is limited to that region.

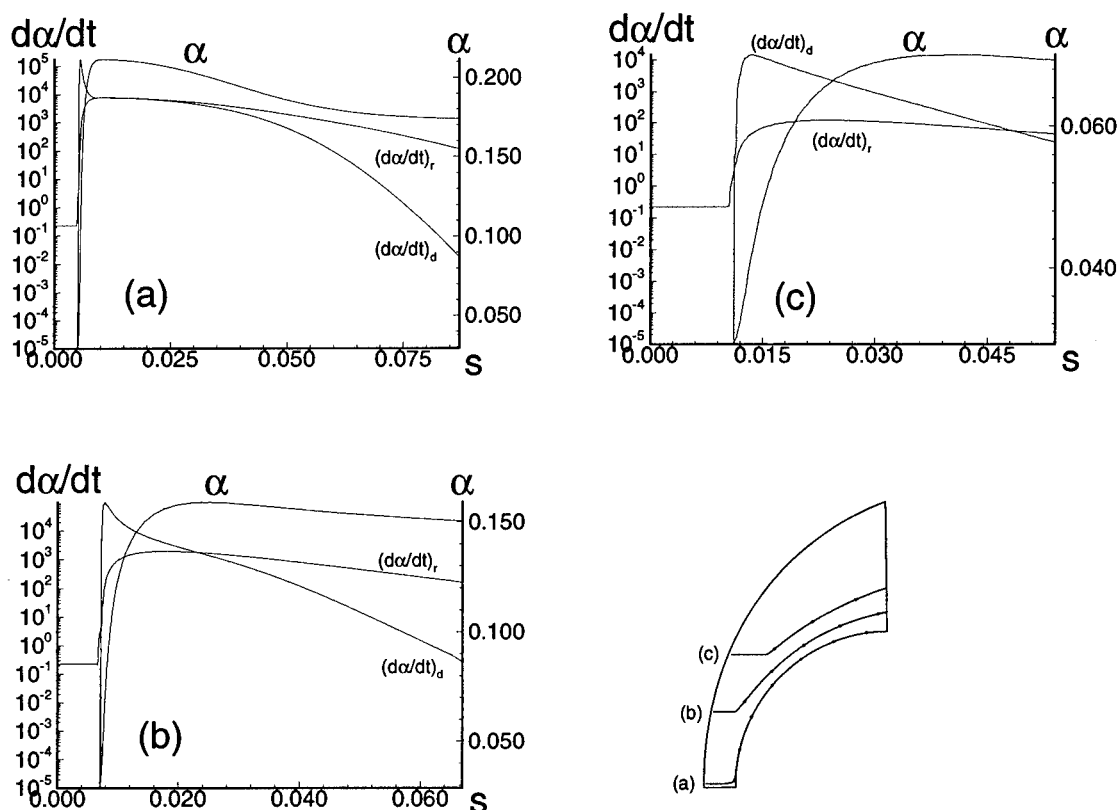


Fig. 3. Reaction rate and composition variation along three selected streamlines. The streamlines are labelled *a*, *b* and *c* in the diagram on the right. The kink in the streamline indicates the shock location. The dissociation rate and recombination rate are plotted separately, and the dissociation fraction, α reaches a maximum at the cross-over point. As may be seen, recombination may not be neglected for the inner streamlines

Figure 4 shows a differential interferogram of the flow of nitrogen over a 10 cm diameter sphere at a specific reservoir enthalpy of 16 MJ/kg and a reservoir pressure of 60 MPa. Differential interferometry measures gradient of optical path length. Specifically, it measures the component of the gradient in the image plane and in a direction that can be chosen by rotating an optical element in the setup. The parallel fringes in the undisturbed free stream of the photograph are oriented at right angles to the direction of this component. In order to translate the fringe shift observed in the flow field behind the shock into a refractive index field, from which the density might be inferred, it would be necessary to perform an inversion of the Abel integral equation using the measured fringe shift as input. While this does not present a problem, the result is still ambiguous, since the refractive index may not be interpreted directly as density in a gas whose composition is not uniform. In nitrogen flow, this problem is relatively mild, but if one deals with air, where some 8 species may be expected to be present, the problem is harder. A better comparison with computed results is to compute the differential interferogram from the calculated flow field, using the computed density and composition and the known refractive indices of the components of the gas mixture.

This was done by first calculating the infinite fringe interferogram and subtracting from it a displaced copy of itself. This gives a double image of the boundaries, such as the body, of course,

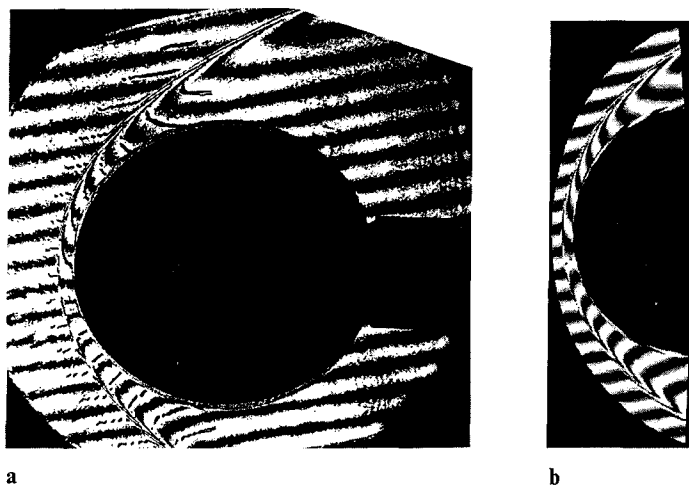


Fig. 4. Comparison of experimental and computed differential interferograms of nitrogen flow over a sphere, at the same conditions as those of Fig. 1. **a** Finite-fringe differential interferogram of nitrogen flow over a sphere. **b** Corresponding computed interferogram at the same conditions as the experiment. Except for a slight difference in the vicinity of the shock, the two pictures are virtually congruent. To show this, a line along the center of the calculated white fringe is superimposed on the photograph

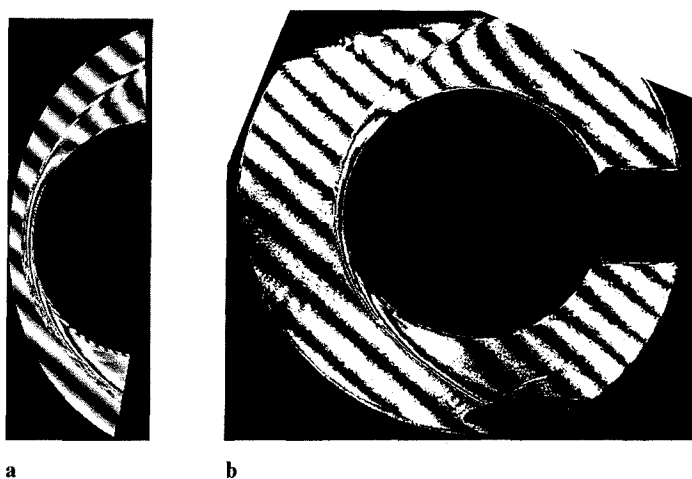


Fig. 5. Comparison of differential interferograms in the case of carbon dioxide flow over a sphere. Free stream: 3.18 km/s, 0.106 kg/m³, 8.52 MJ/kg. In this case advantage has been taken of the symmetry of the flow to get both components of the gradient measured by the differential interferogram, by setting the angle of the fringes at 45 deg. in the free stream. **a** Computation, **b** experiment

just as in the experimental differential interferogram. This computed differential interferogram is also shown in Fig. 4 for comparison with the measured one. As may be seen, the features of the photo are faithfully reproduced by the computation, both qualitatively and quantitatively. It should be noted that if the density of the computation is changed by 10%, this change can be resolved easily in the interferogram. An interesting feature of symmetrical flows is that the differential interferogram can be chosen to measure the component of gradients at 45 deg. to the axis (or plane) of symmetry, so that one half of the photo gives one component, and the other half the orthogonal component of the gradient.

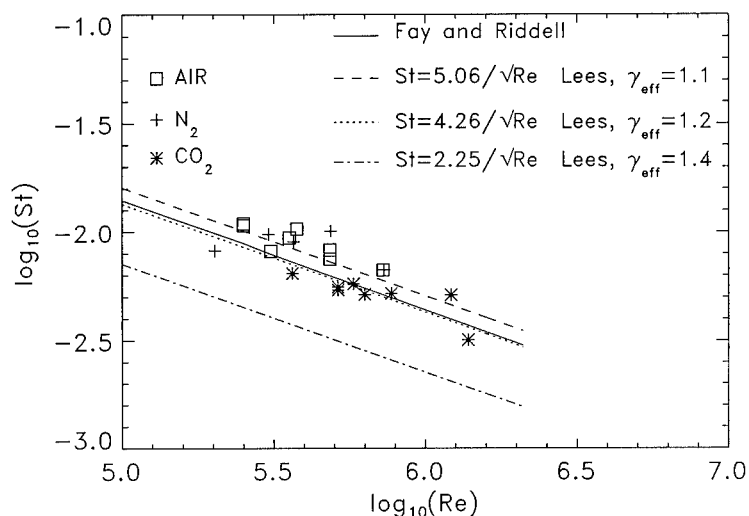


Fig. 6. Stagnation-point heat flux in dimensionless form, and comparison with Lees' theory, and Fay and Riddell's correlation

To show another example, Fig. 5 shows a similar exercise for a carbon dioxide flow. Again, the comparison shows excellent agreement. Clearly, viscous effects are not important in the determination of the major features of the flow field.

Viscous and thermal effects are, however, the main reason for studying these flows in the first place. The heat flux measurements are thus an important component of our study. With the extremely high values of heat flux encountered at the stagnation point of the sphere, the classical thin-film metal gauges are not suitable. Thermocouple gauges were found to serve our purpose very well. The maximum value of the heat flux measured was 60 MW/m^2 . The heat transfer rate was normalized to form the Stanton number, and a plot of this against the Reynolds number based on the sphere diameter is shown in Fig. 6.

4 Conclusions

A free-piston shock tunnel was used to obtain new data on flow over spheres at high enthalpy and Reynolds number, where non-equilibrium dissociation is important. By using spheres, the end effects of previous data on flow over cylinders were eliminated and much better agreement with computations was observed, in interferometric flow-field measurements. Though computations show that recombination is important in parts of the flow field, binary scaling is a satisfactory model for global quantities such as the stand-off distance. Stagnation-point heat flux measurements broadly follow expected behavior, though systematic differences between different gases are apparent.

Acknowledgement

This work was supported by AFOSR Grant No. F49610-92-J-0110 monitored by Dr. L. Sakell.

References

- [1] Hornung, H. G.: Performance data of the new free-piston shock tunnel at GALCIT. AIAA 92-3943 Nashville (1992).
- [2] Eitelberg, G.: The high-enthalpy shock tunnel in Göttingen. AIAA 92-3942 (1992).
- [3] Hornung, H. G.: Nonequilibrium dissociating nitrogen flows over spheres and circular cylinders. *J. Fluid Mech.* **53**, 149–176 (1972).
- [4] Rock, S. G., Candler, G. V., Hornung, H. G.: Analysis of thermochemical nonequilibrium models for carbon dioxide flows. AIAA 92-2852 (1992).
- [5] Candler, G. V.: The computation of weakly ionized hypersonic flows in thermo-chemical nonequilibrium. Ph. D. Thesis, Stanford University 1988.
- [6] Macrossan, M. N.: Hypervelocity flow of dissociating nitrogen downstream of a blunt nose. *J. Fluid Mech.* **217**, 167–202 (1990).
- [7] Hornung, H. G.: Nonequilibrium dissociating flow after a curved shock. *J. Fluid Mech.* **74**, 143–160 (1976).

Authors' addresses: Professor Dr. H. Hornung and Dr. C. Wen, Graduate Aeronautical Labs., California Institute of Technology, Pasadena, CA 91125, and Prof. Dr. G. Candler, Dept. of Aerospace Engineering and Mechanics, University of Minnesota, 110 Union St. S. E., Minneapolis, MN 55455, U.S.A.

Nonequilibrium recombination after a curved shock wave

Chihyung Wen and Hans Hornung
Graduate Aeronautical Laboratories
California Institute of Technology
Pasadena, California 91125, USA

Abstract

The effect of nonequilibrium recombination after a curved two-dimensional shock wave in a hypervelocity dissociating flow of an inviscid Lighthill-Freeman gas is considered. Analytic solutions are obtained with the effective shock values derived by Hornung (1976) and the assumption that the flow is 'quasi-frozen' after a thin dissociating layer near the shock. The solution gives the expression of dissociation fraction as a function of temperature on a streamline. It can then provide a rule of thumb to check the validity of binary scaling for the experimental conditions and a tool to determine the limiting streamline which delineates the validity zone of binary scaling. The effects upon the nonequilibrium chemical reaction of the large difference in free stream temperature between free-piston shock tunnel and equivalent flight conditions are discussed. Numerical examples are presented and the results are compared with solutions obtained with two-dimensional Euler equations using Candler's code.

Keywords: hypervelocity flow, real gas effects, binary scaling, Lighthill-Freeman gas, free-piston shock tunnel.

1. Introduction

In hypervelocity flows the stagnation enthalpy can be large enough to cause dissociation of air after the bow shock ahead of a blunt body. The nature of the chemical nonequilibrium flows about blunt bodies is important in the aerodynamic design of such vehicles. Models using frozen or equilibrium chemistry are unable to predict the nonequilibrium flow field. This was not realized until the Shuttle Orbiter experienced a pitching moment significantly different from the pre-flight predictions (Maus, Griffith & Szema, 1984). These predictions were obtained from extensive 'cold' hypersonic wind-tunnel testing in facilities which could not produce the 'real gas' effects.

At high altitudes of flight, chemical recombination can be neglected for nonequilibrium flows about blunt bodies. Binary scaling provides an important and useful model scaling of nonequilibrium effects for laboratory simulation (Gibson & Marrone, 1964). The free-piston shock tunnel T5 at GALCIT which had the specific aim of studying the fundamental features of high-enthalpy reacting flows was built based on the principle of binary scaling. The facility was named T5 in honor of its Australian predecessors T1 to T4. All these facilities use the principle of free-piston adiabatic compression of the driver gas of a shock tunnel to achieve the high shock speeds and densities required to generate the high enthalpy and reaction scaling. One additional essential feature of the free-piston shock tunnel is that the test duration is sufficiently short to avoid destruction of the machine by melting. A more detailed description of T5 and its performance envelope, flow quality and repeatability may be found in Hornung (1992). The largest facility of this type has been completed in 1992 at Göttingen, see Eitelberg (1992).

Hornung (1976) performed an approximate analysis of the nonequilibrium flow behind a curved shock wave, under the as-

sumption that binary reactions are dominant. He concluded that the flow could be conveniently divided into a region of intense dissociation close to the shock followed by a large region of chemically frozen flow. Macrossan (1990) has shown that the recombination reaction is not negligible at the higher values of the density in the test section of the free-piston shock tunnel, although, further downstream the flow is frozen again. The aim of the work described here is to relax Hornung's binary reaction assumption and to understand the mechanism which 'freezes' the recombination.

The work is concerned with inviscid, adiabatic, hypersonic flow of a diatomic gas after a curved shock wave under conditions where the free stream speed V_∞' is sufficiently high to dissociate the gas. A Lighthill-Freeman gas is considered, for which the reaction rate is given by Freeman (1958)

$$\frac{d\alpha}{dt'} = C' \rho' T'^\eta \left\{ (1 - \alpha) \exp\left(\frac{-\theta_d'}{T'}\right) - \alpha^2 \frac{\rho'}{\rho_d'} \right\}, \quad (1.1)$$

where t' , ρ' , T' and α are time, density, temperature and dissociation fraction, and C' , η , θ_d' and ρ_d' are constants describing the rate and equilibrium properties of the gas. A further simplification of the rate equation is afforded by the fact that, for situations where dissociation is important in gases such as nitrogen or oxygen, T' is much smaller than θ_d' , so that the temperature dependence of the dissociation near the shock is very strongly dominated by the exponential function, and the factor $C' \rho' T'^\eta (1 - \alpha)$ may be considered constant (Freeman, 1958). With the above approximations, the reaction-rate equation is written as

$$\frac{d\alpha}{dt'} = \frac{V_\infty' \kappa_0'}{\epsilon} \left\{ \exp\left(\frac{-\theta_d'}{T'}\right) - \frac{\alpha^2}{1 - \alpha} \frac{\rho'}{\rho_d'} \right\}, \quad (1.2)$$

where ϵ is a small constant parameter ($\epsilon \approx 10^{-5}$) and $1/\kappa_0'$ is a typical length scale, e.g. the radius of curvature of the shock.

Using the above reaction model and the assumption that the flow is 'quasi-frozen' in the region downstream of Hornung's dissociating layer ($\alpha \sim \alpha_0$, where α_0 is the effective frozen dissociation fraction), an approximate equation can be derived that incorporates recombination and can be solved analytically. The analytic solutions are successful in explaining the phenomenon described by Macrossan. The freezing of the flow occurs in the free-piston shock tunnel because of the strong exponential temperature dependence of the dissociation reaction rate and the effect of a pressure gradient on temperature and density for both dissociation and recombination reaction rates. The analytic solutions are compared with results of the state-of-the-art numerical method by Candler (1988). The analytic solutions provide a criterion for determining the limiting streamline which delineates the validity zone of binary scaling. A rule of thumb to check the validity of binary scaling is also presented. Finally, the effects upon the binary scaling of the large difference in free stream temperature between flight and free-piston shock tunnel conditions are discussed.

2. Equations of motion on a streamline

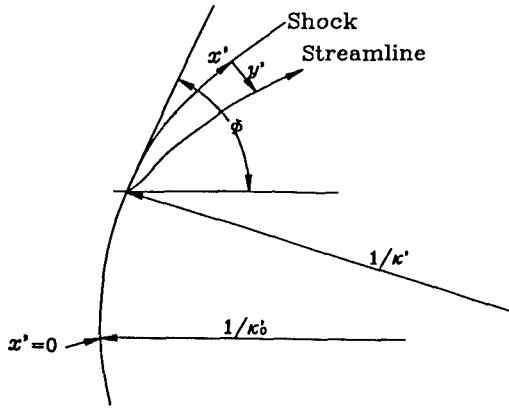


Fig. 1. Notation

To make the content more complete, in this section, the equations of motion on a streamline derived by Hornung (1976) will be reiterated concisely. The coordinate system is illustrated in Fig. 1, where x' and y' are co-ordinates parallel and perpendicular to a shock of curvature $\kappa'(x')$, and $\phi(x')$ is the incident angle to the shock of the uniform free stream, of velocity V_∞' . κ' is taken to be positive if the shock is convex towards the upstream direction. Let u' and v' be the components of velocity in x' and y' directions respectively, p' , T' and ρ' be the pressure, temperature and density, and h' be the specific enthalpy of the gas. The variables are nondimensionized according to

$$\left. \begin{aligned} h &= h'/(V_\infty')^2, \quad T = T'R'/(V_\infty')^2, \quad p = p'/\rho_\infty'(V_\infty')^2, \\ v &= v'/V_\infty', \quad u = u'/V_\infty', \quad \rho = \rho'/\rho_\infty', \\ x &= x'\kappa_0', \quad y = y'\kappa_0', \quad \kappa = \kappa'/\kappa_0', \end{aligned} \right\} \quad (2.1)$$

where the subscript ∞ refers to conditions in the free stream, R' is the specific gas constant and κ_0' is the shock curvature at a representative point.

An ideal dissociating gas is considered (Lighthill 1957; Freeman 1958), for which the equations of state and the reaction-rate equation become

$$\left. \begin{aligned} h &= \frac{4 + \alpha}{1 + \alpha} \frac{p}{\rho} + \alpha \theta, \quad T = \frac{p}{\rho(1 + \alpha)}, \\ \frac{d\alpha}{dt} &= \frac{1}{\epsilon} \left\{ \exp\left(\frac{-\theta_d}{T}\right) - \frac{\alpha^2}{1 - \alpha} \frac{\rho}{\rho_d} \right\}. \end{aligned} \right\} \quad (2.2)$$

α is a nonequilibrium variable (e.g. the dissociation fraction) and θ is the dissociation energy $R'\theta_d'$ per unit mass normalized by $V_\infty'^2$ and is $O(1)$ for situations where dissociation produces significant effects. The conservation equations for momentum, energy and mass are (see Hayes & Probstein 1966, p. 168)

$$\left. \begin{aligned} uu_x + (1 - \kappa y)vu_y - \kappa uv + p_x/\rho &= 0, \\ uv_x + (1 - \kappa y)vv_y + \kappa u^2 + (1 - \kappa y)p_y/\rho &= 0, \\ h_p p_y + h_\rho \rho_y + h_\alpha \alpha_y + vv_y + uu_y &= 0, \\ (\rho u)_x - \kappa \rho v + (1 - \kappa y)(\rho v)_y &= 0. \end{aligned} \right\} \quad (2.3)$$

The subscripts denote partial differentiation.

The boundary conditions at the shock are (see Vincenti & Kruger 1965, p. 180)

$$\left. \begin{aligned} p_1 - p_\infty &= m^2(1 - \rho_1^{-1}), \quad \alpha_1 = \alpha_\infty, \quad v_1 = m/\rho_1, \\ h_1 - h_\infty &= \frac{1}{2}m^2(1 - \rho_1^{-2}), \quad u_1^2 = 1 - m^2, \end{aligned} \right\} \quad (2.4)$$

where $m = \sin \phi$ and the subscript 1 denotes values just downstream of the shock. Boundary conditions are specified only on the shock because experience with inverse numerical techniques applied to blunt-body problems shows that, over a distance which is small compared with the radius of curvature of the shock, the shock boundary conditions are sufficient to specify the problem. By combining x and y derivatives (see Hornung 1976), the time derivatives of p , ρ and V becomes

$$\left. \begin{aligned} F \frac{dp}{dt} &= \rho h_\alpha \frac{d\alpha}{dt} + \kappa \frac{\rho^2 h_\rho}{v} G, \\ F \frac{d\rho}{dt} &= \frac{\rho}{v^2} h_\alpha \frac{d\alpha}{dt} - \kappa \frac{\rho^2}{v} (h_p - \frac{1}{\rho}) G, \\ V \frac{dV}{dt} &= -\frac{1}{\rho} \frac{dp}{dt}, \end{aligned} \right\} \quad (2.5)$$

where $V = (u^2 + v^2)^{1/2}$ is the flow speed, h is considered as $h(p, \rho, \alpha)$, and

$$\left. \begin{aligned} F &= 1 - \rho \left(\frac{h_\rho}{v^2} + h_p \right), \\ G &= \left\{ v^2 + u^2 + \frac{uv_x}{\kappa} - \frac{u}{v} \frac{1}{\rho} \frac{p_x}{\kappa} - v \frac{u_x}{\kappa} \right\} / (1 - \kappa y). \end{aligned} \right\} \quad (2.6)$$

3. The differential equation for $\alpha(T)$ along a streamline

We now proceed as in Hornung (1976) but extend the analysis to include the recombination reaction rate. Differentiating $T(p, \rho, \alpha)$ with respect to t , substituting for the time derivatives of p and ρ from (2.5) and dividing by $d\alpha/dt$ results in the following equations:

$$F \frac{dT}{d\alpha} = \left(\frac{T_\rho}{v^2} + T_p \right) \rho h_\alpha + F T_\alpha + \frac{\kappa \rho^2 G}{v} \left[T_p h_\rho - T_\rho (h_p - \frac{1}{\rho}) \right] \frac{dt}{d\alpha}.$$

The relevant derivatives of T and h , and $d\alpha/dt$ in (2.2) may now be substituted into (3.1), which becomes

$$\frac{dT}{d\alpha} = - \frac{(1 - \rho v^2/p)\theta + T + \epsilon \kappa v G e^{\theta/T}/(1 - A)}{(4 + \alpha) \left(1 - \frac{3}{4 + \alpha} \frac{\rho v^2}{p} \right)}, \quad (3.2)$$

where

$$\left. \begin{aligned} A &= \frac{\alpha^2}{1 - \alpha} \frac{\rho}{\rho_d} e^{\theta/T} = B e^{\theta/T}, \\ B &= \frac{\alpha^2}{1 - \alpha} \frac{\rho}{\rho_d}. \end{aligned} \right\} \quad (3.3)$$

By estimating the order of magnitude of all the terms of (3.2) and retaining only the first-order terms, one gets

$$\frac{dT}{d\alpha} = -\frac{\theta - T\{(1+\alpha)\theta/m^2 - 1\} + b\epsilon(1+\alpha)Te^{\theta/T}/(1-A)}{(4+\alpha)\left\{1 - \frac{3(1+\alpha)}{4+\alpha} \frac{T}{m^2}\right\}}, \quad (3.4)$$

where

$$b = 3(1-m^2)\kappa m^{-1}, \quad (3.5)$$

To demonstrate all the features of the solution with less complexity and good accuracy, we neglect α in the two terms in curly brackets in (3.4), assuming α is negligible compared with 1. The equation (3.4) becomes

$$\frac{d\alpha}{d\xi} = -\frac{(4+\alpha)(1-\lambda\xi)}{1-\mu\xi + \epsilon b\xi(1+\alpha)e^{1/\xi}/(1-A)}, \quad (3.6)$$

where $\xi = T/\theta$ and

$$\mu = (\theta - m^2)/m^2, \quad \lambda = \frac{3}{4}\theta/m^2. \quad (3.7)$$

This model equation (3.6) differs from the one Hornung derived (1976) only in the factor 'A' which is the ratio of recombination rate to dissociation rate of an ideal dissociating gas. A is $O(1)$ right behind the shock, but may become important further downstream.

4. Solution for $\alpha(\xi)$ along a streamline

Near the shock, where T or ξ is relatively large, the term in ϵ in (3.6) is small. As the temperature falls with proceeding dissociation, the ϵ term, which is due to the negative pressure gradient accompanying the curved shock, becomes important and finally dominates. One notices that the factor 'A' will expedite the speed with which $d\alpha/d\xi$ approaches zero as the temperatures falls away from the shock. Three cases are then discussed.

4.1 Case 1: $A \ll 1$ for all ξ of interest.

Hornung's model equation is recovered from (3.6) and binary scaling is appropriate. All the solutions obtained by Hornung (1976) with the method of matched asymptotic expansions will hold. The flow can then be divided into a thin region of intense reaction close to the shock followed by a large region of chemically frozen flow. The thin reacting layer can then be considered to be part of the shock and effective shock conditions on each streamline by extrapolating the frozen-flow solution back to the shock can be defined.

4.2 Case 2: $A = O(1)$ before $\epsilon b\xi(1+\alpha)e^{1/\xi}$ becomes $O(1)$

The effective shock conditions were used to estimate the order of magnitude of A. $A = O(1)$ when $\xi_* = O(1/\log(B_0)^{-1})$, where

$$B_0 = \frac{\alpha_0^2}{1-\alpha_0} \frac{\rho_0}{\rho_d}, \quad (4.2.1)$$

and α_0, ρ_0 are the effective frozen dissociation fraction and effective shock density. In this case, recombination is always important and $\xi_* > \xi_0$, where ξ_0 is the effective shock temperature.

4.3 Case 3: $A = O(1)$ after $\epsilon b\xi(1+\alpha)e^{1/\xi}$ becomes $O(1)$ ($\xi_* < \xi_0$ or $\xi_* \approx \xi_0$)

This case is the one we are most interested in. The flow will tend to reach and maintain the effective frozen dissociation level α_0 and further downstream, recombination will bring α_0 down again. One can simplify the model equation (3.6) even further by observing that $A \gg 1$ and $\epsilon b\xi(1+\alpha)/B \gg 1$ in the region further downstream of the dissociating layer. If we neglect the terms $\lambda\xi$ and $(1-\mu\xi)$, (3.6) becomes

$$\frac{d\alpha}{d\xi} = \frac{4+\alpha}{\epsilon b\xi(1+\alpha)/B}. \quad (4.3.1)$$

Notice that the sign of $d\alpha/d\xi$ has changed from negative (~ -4) near the shock to positive in (4.3.1). To solve (4.3.1) the assumption that the flow is 'quasi-frozen' in the region downstream of the dissociating layer was made. The assumption was made based on observations from Macrossan's (1990) and Hornung, Wen & Candler's (to appear) results that the dissociation fraction varied less than 20% from the maximum value in the free-piston shock tunnel conditions. The assumption gives

$$\rho \sim \rho_0 \left(\frac{\xi}{\xi_0}\right)^{\frac{1}{\gamma-1}}, \quad \gamma = \frac{4+\alpha_0}{3}, \quad (4.3.2)$$

where γ is the ratio of specific heats for the Lighthill-Freeman gas model.

(4.3.1) then becomes

$$\left. \begin{aligned} \frac{d\alpha}{d\xi} &= K \alpha^2 \xi^{\frac{2-\gamma}{\gamma-1}} \\ K &= \frac{4\rho_0}{\epsilon b\rho_d \xi_0^{\frac{1}{\gamma-1}}} \end{aligned} \right\} \quad (4.3.3)$$

assuming that α is small compared to one. (4.3.3) may be integrated to give the 'quasi-frozen' flow solution

$$\alpha = \left[\frac{1}{\alpha_*} - K(\gamma-1)(\xi^{\frac{1}{\gamma-1}} - \xi_*^{\frac{1}{\gamma-1}}) \right]^{-1}, \quad (4.3.4)$$

where $\xi_* = 1/\log(B_0)^{-1}$ and α_* is taken to be α_0 . It is assumed that the initial condition is $\alpha = \alpha_0$ at $\xi = \xi_*$ which is the premise of Case (4.3). The assumption that recombination becomes dominant at $\xi = \xi_*$ in Case (4.2) and Case (4.3) will be justified later, with a numerical example.

5. Calculation method and validation

Candler's code was used to compute the inviscid hypervelocity reacting flow over an axisymmetric or a two-dimensional body and to compare with the analytical solution obtained in section 4. The program uses a finite-volume method and is described in detail in Candler (1988). The flow field is described

by coupled partial differential equations for the conservation of species, mass, mass-averaged momentum, vibrational energy of each diatomic species and total energy. An implicit Gauss-Seidel technique was used to obtain the steady-state solution to these fully coupled equations for different gases. The reaction rates were calculated using Park's (1985) two-temperature model and the flux splitting method was used to maintain the numerical stability. Fig. 2 (a) and 2 (b) show the comparison of experimental differential interferograms obtained with the free-piston shock tunnel T5 and computational differential interferograms constructed from the calculated flow fields, using the computed density and composition and the known refractive indices of the components of the gas mixture. Good agreement of the shock shape and the fringe pattern may be observed. Since the dissociation fraction is not accessible during the experiment, the computational method provides a good way to obtain partial information about it.

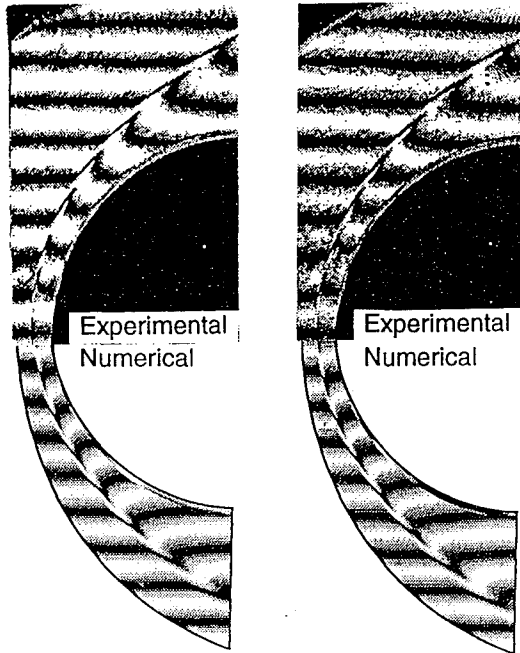


Fig. 2(a)

Fig. 2(b)

Fig. 2 Comparison of experimental and computed differential interferograms of air and N_2 flow over a sphere of 4 in diameter. Fig. 2 (a) air, Free stream: 5.45 km/s, 0.0161 kg/m³, 20.6 MJ/kg. Fig. 2 (b) N_2 , 5.35 km/s, 0.0181 kg/m³, 20.2 MJ/kg.

6. Results and discussion

In this section, one set of typical flow conditions in the shock tunnel T5 was chosen to illustrate the nature of the solutions obtained in section 4. Fig. 3 shows the dissociation rate, recombination rate and dissociation fraction along three streamlines in a nitrogen flow over a circular cylinder of diameter $D' = 4$ in. Free stream conditions are: $V_\infty' = 5.08$ km/s, $\rho_\infty' = 0.04$ kg/m³, $h_0' = 16.0$ MJ/kg, $T_\infty' = 2260$ K and $\alpha_\infty = 0.029$. Clearly, the recombination rate is not negligible compared to the dissociation rate, especially for the streamlines that cross the shock close to the axis. This essentially violates the binary scaling. It is interesting to point out that, while the recombination rate becomes dominant in the downstream region, the flow seems to be frozen again due of the slow recombination rate.

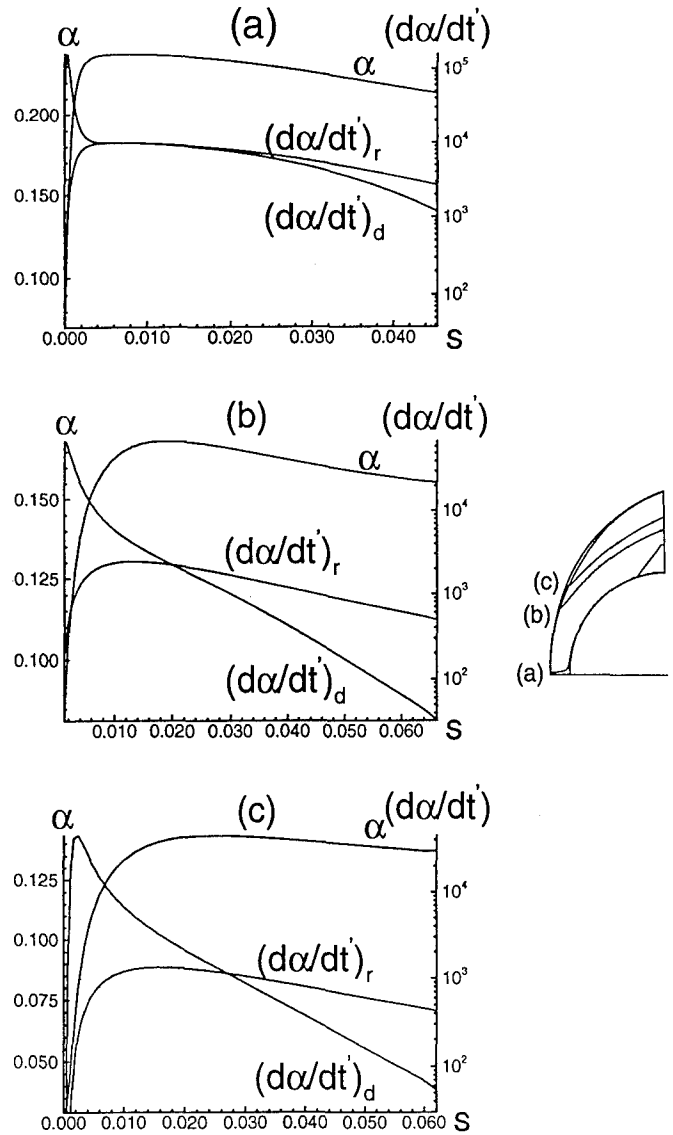


Fig. 3 Reaction rate and dissociation fraction variation along three selected streamlines. The streamlines are labelled a, b, c in the diagram on the right. $(d\alpha/dt)'_d$ and $(d\alpha/dt)'_r$ are dissociation rate and recombination rate respectively. As may be seen, the recombination rate is not negligible for the inner streamlines.

In Table 1, the assumption that recombination becomes dominant at $\xi = \xi_*$ in Case (4.2) and (4.3) is justified. Close to the axis ($\phi = 89^\circ$ and 82°), $\xi_0 < \xi_*$ and the solutions belong to Case (4.2). From streamline (a) ($\phi = 89^\circ$) in Fig. 3, it is clear that recombination becomes important before the flow reaches the frozen solutions of Case (4.1). For the other streamlines in Table 1 where $\xi_0 > \xi_*$, they are classified into Case (4.3). The good agreement between α_0 and $\alpha_{*,num}$ seems to support the assumption of the initial condition of equation (4.3.4). From streamlines (b) ($\phi = 72^\circ$) and (c) ($\phi = 67.5^\circ$) in Fig. 3, they also suggest that the flow tends to reach and maintain Hornung's frozen dissociation level α_0 before recombination brings α_0 down again.

One can also transfer the co-ordinate system of Fig. 3 into (α, ξ) co-ordinate system. Fig. 4 (a) and 4 (b) show the comparison of solution (4.3.4), model equations (3.6) and (4.3.2), and the numerical results from candler's code, where Fig. 4 (a) and

ϕ	ξ_0	α_0	ξ_*	$\xi_{*,num}$	$\alpha_{*,num}$
89.0	0.0470	0.270	0.0669	0.0643	0.240
82.0	0.0589	0.217	0.0637	0.0634	0.222
76.0	0.0628	0.188	0.0621	0.0621	0.199
72.0	0.0644	0.169	0.0610	0.0600	0.168
67.5	0.0652	0.147	0.0597	0.0590	0.137
62.0	0.0662	0.116	0.0577	0.0573	0.110
56.5	0.0662	0.085	0.0553	0.0556	0.085

Table 1. The justification of the assumption that recombination becomes dominant at $\xi = \xi_*$ in Case (4.2) and (4.3). ϕ is the incident angle to the shock of the uniform free stream. ξ_0 and α_0 are Hornung's effective shock temperature and dissociation fraction. ξ_* is defined in (4.3.4). $\alpha_{*,num}$ is the maximum value of the dissociation fraction extracted from the numerical calculation and $\xi_{*,num}$ is the corresponding temperature at $\alpha = \alpha_{*,num}$.

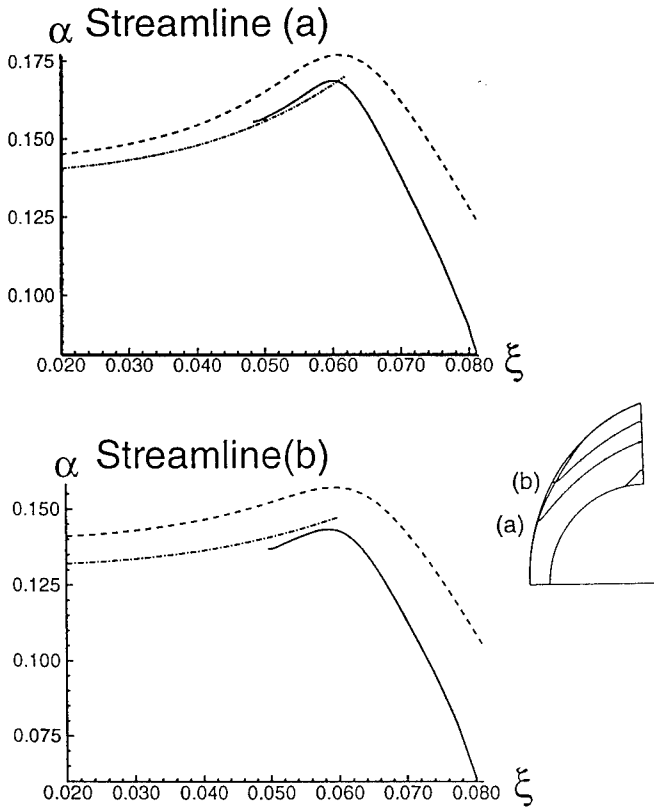


Fig. 4 Plots of dissociation fraction α versus dimensionless temperature ξ along two streamlines a and b over a circular cylinder (see inset on right). Free stream conditions: 5.08 km/s, nitrogen, 0.04 kg/m³, 16.0 MJ/kg. Full line: numerical integration of the model equations (3.6) and (4.3.2). Dashed line: Numerical solution of Euler equations using Candler's code ($\alpha_\infty = 0.029$). Dash-dot line: Analytical solution of the approximate equation (4.3.4).

4 (b) correspond to the streamline (b) and (c) in Fig. 3 respectively. It may be seen that the solutions (4.3.4) start at $\xi = \xi_*$ in good agreement with numerical results. Although the full model equations (3.6) and (4.3.2) with the initial condition $\alpha = \alpha_\infty$ at $\xi = \xi_1$ seems to overestimate the dissociation fraction, the error ($\sim 5\%$ for streamline (a) and 13% for streamline (b) in Fig. 4) is still under acceptable range, considering how simple the model equations are. The most important result is the agreement of the tendency to the final frozen dissociation fraction among the three solutions is favourably good.

With the above results in mind, one is able to use solution (4.3.4) to set a rule of thumb of validity of binary scaling. Equation (4.3.4) can be re-written in the form of

$$\alpha = \alpha_0 \left[1 + \alpha_0 K (\gamma - 1) \xi_*^{\frac{1}{\gamma-1}} \left(1 - \left(\frac{\xi}{\xi_*} \right)^{\frac{1}{\gamma-1}} \right) \right]^{-1}. \quad (6.1)$$

Binary scaling will work if

$$\alpha_0 K (\gamma - 1) \xi_*^{\frac{1}{\gamma-1}} \ll 1. \quad (6.2)$$

The flow will be 'quenched' and $\alpha \rightarrow \alpha_0$. The Case (4.3) degenerates into Case (4.1).

Substituting for K from (4.3.3), (6.2) becomes

$$\frac{\alpha_0 \rho_0}{b \epsilon \rho_d} \frac{4(1 + \alpha_0)}{3} \left(\frac{\xi_*}{\xi_0} \right)^{\frac{3}{1+\alpha_0}} \ll 1. \quad (6.3)$$

Note that

$$\left. \begin{aligned} \frac{4(1 + \alpha_0)}{3} \left(\frac{\xi_*}{\xi_0} \right)^{\frac{3}{1+\alpha_0}} &\sim O(1), \\ \rho_0 &\sim O(10). \end{aligned} \right\} \quad (6.4)$$

(6.3) may then be simplified into

$$G \equiv \frac{\alpha_0}{b \epsilon \rho_d} \ll 0.1. \quad (6.5)$$

(6.5) then presents a rule of thumb to check the validity of binary scaling. Note that $\rho_d = \rho'_d / \rho'_\infty$. Again free stream density has to be low to use binary scaling. Take streamline (a) in Fig. 4 as an example. The shock shape for a flow over a circular cylinder is well approximated by the catenary $\kappa = m^2$, so that $b = 3(1 - m^2)m$. For streamline (a) $\phi = 72^\circ$, $b = 0.272$, $\epsilon = 8.88 \times 10^{-6}$ and $\alpha_0 = 0.169$. A value of $\rho'_d = 130$ gm/cm³ is recommended by Lighthill(1957). $G = 0.021$ and is not much smaller than 0.1. In fact, it implies that as $\xi \rightarrow 0$, $\alpha \sim \alpha_0 / (1 + 10G) = 0.14$, which is consistent with Fig. 4 (a). About 20% of atoms will recombine. If one sets the criterion that the mass fractions should agree to within 5% on the $\phi = 72^\circ$ streamline between the free flight conditions and the shock tunnel environment, the above test conditions with $\rho'_\infty = 0.04$ kg/m³ is certainly not appropriate to simulate the free flight conditions where density

is much lower and the flow will freeze at the frozen dissociation fraction level.

The analytic solution (4.3.4) can also provide a tool to determine the limiting streamline which delineates the validity zone of binary scaling. If one sets the same 5% discrepancy of the mass fractions as the criterion for the limiting streamline and 'guesses' that $\xi \sim 0.05$ at the vertical mid-plane of the circular cylinder, (4.3.4) will provide $\alpha(\xi = 0.05) = 0.14$ for the streamline of $\phi = 67.5^\circ$. Compared to $\alpha_0 = 0.147$, the discrepancy of the mass fraction is about 4.75%. The numerical method (see Fig. 4 (b)) gives us $\alpha_{num}(\xi = 0.05) = 0.132$ and $\alpha_{*,num} = 0.137$. The discrepancy of the mass fraction is about 3.65%. The analytic solution (4.3.4) predicts the limiting streamline at $\phi = 67.5^\circ$ which is very close to the numerical prediction. For streamlines outside the limiting streamline, binary scaling is valid. For those inside the limiting streamline, three body recombination can't be neglected.

The final point to be addressed is the large Mach number difference between the free flight conditions and the shock tunnel flows, pointed out by Macrossan(1990). It is known that the high reservoir temperature and the 'freezing' of the nozzle flow produce high free stream temperature and some free stream dissociation in the shock tunnel environment. In the free flight conditions, where the atmospheric temperature is much lower than the free stream temperature in the shock tunnel and there is no frozen dissociation in the free stream, the Mach number is much higher than produced by the shock tunnel. Typical flight free stream conditions with the same circular cylinder and free stream density ($\rho'_\infty = 0.04 \text{ kg/m}^3$) as in the experiments were considered. This density corresponds to that in the Earth's atmosphere at an altitude of about 25 km. The free stream temperature was taken as 217 K, which is about the atmospheric temperature for that altitude, and the free stream velocity was chosen to give the same stagnation enthalpy ($h'_0 = 16.0 \text{ MJ/kg}$) as in the experiments. The free stream Mach number was then 18.6 as opposed to 5.5 in the experiments. The effective dissociation fraction α_0 on streamlines that have crossed the shock at ϕ , for the shock tunnel and the equivalent flight conditions, as a function of ϕ , are compared in Fig. 5.

The agreement is good for the streamlines with a large incident angle and gets worse as the curved shock gets weaker. The shock tunnel flow has a higher frozen dissociation fraction than the equivalent flight flow, for streamlines that cross the shock away from the axis. This is because of the two different flow velocities which have been chosen. Although the stagnation enthalpy has been chosen to be the same to match the simulation parameter of the ratio of the dissociation energy and the energy of the flow, the binary scaling parameter $\rho'_\infty D'/u'_\infty$ will not be the same, which is the ratio of the dissociation rate and the flow rate. The shock tunnel flow, with the slower speed, will have more 'time' to dissociate than the equivalent flight flow does, before the expansion causes the 'quenching' of the flow. Note that only results with ϕ smaller than 80° were shown because the theory of effective shock values is not valid for ϕ larger than 80° , where the recombination is important. Also shown in Fig. 5 is the other flow condition with $V'_\infty = 5.08 \text{ km/s}$, $\rho'_\infty = 0.04 \text{ kg/m}^3$, $h'_0 = 13.0 \text{ MJ/kg}$ and $T'_\infty = 217 \text{ K}$. As may be seen, the dissociation fraction of the flow is well below the other two cases. In this case, the binary scaling parameter is the same as in the shock tunnel flow and the time scale is matched. However, the

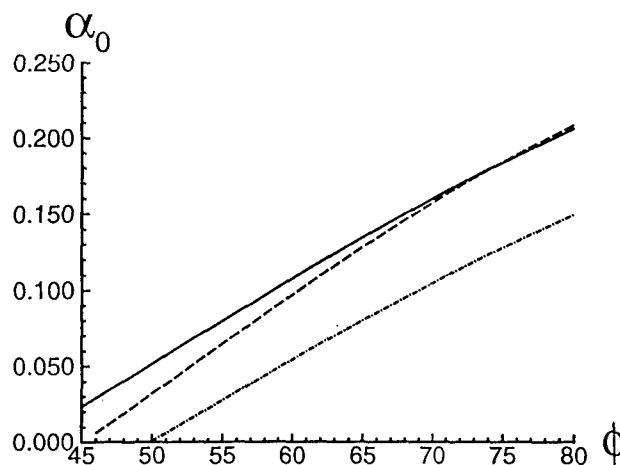


Fig. 5 Comparison of effective frozen dissociation fraction α_0 for the free-piston shock tunnel and equivalent flight conditions. ϕ is the incident angle to the shock of the uniform free stream. Free stream conditions: N_2 , $\alpha_\infty = 0.0$, $D' = 4 \text{ in}$. Full line: Shock tunnel flow with conditions 16.0 MJ/kg, 5.08 km/s, 0.04 kg/m³, 2260 K; Dashed line: Equivalent flight flow with conditions 16.0 MJ/kg, 5.6 km/s, 0.04 kg/m³, 217 K; Dash-dot line: 13.0 MJ/kg, 5.08 km/s, 0.04 kg/m³, 217 K.

energy parameters are not the same. The stagnation enthalpy of the flow is too low to produce the same degree of dissociation of the shock tunnel flow. This suggests that, if one is interested in simulating the chemical nonequilibrium flow over a blunt body with the free-piston shock tunnel facility, it is desirable that the shock tunnel flow has the same stagnation enthalpy as the real flight conditions, although the free stream temperatures will not be the same. Matching the binary scaling $\rho'D'$ and h'_0 is more suitable than matching $\rho'D'$ and u'_∞ .

Fig. 6 (a) and 6 (b) show the comparison of frozen dissociation fraction and the solution (4.3.4) at $\xi = 0.05$ of the shock tunnel and equivalent flight conditions. The solutions (4.3.4) reach a maximum at about $\phi = 75^\circ$ for both flows and gradually merge in the frozen dissociation fractions. Compared to Table 1, one will easily realize that the solution (4.3.4) is not appropriate for ϕ larger than 75° . The solution (4.3.4) manifests itself as the dividing point between the Case (4.2) and (4.3). The limiting streamline can also be easily estimated from Fig. 6 (a) and 6 (b). From Fig. 6 (a) for the shock tunnel flow, one can see that the discrepancy of dissociation fractions will be smaller than 5% for streamlines with the incident angle smaller than 67.5° , which has been mentioned above.

Fig. 7 shows a comparison of the solutions (4.3.4) at $\xi = 0.05$ of shock tunnel and equivalent flight conditions. The dissociation fraction of the equivalent flight condition is lower than that of the shock tunnel flow. Close to the symmetry plane, the discrepancy is small and likely constant. The solutions start to diverge from each other away from the symmetry plane. Compared to Fig. 5 and Fig. 6, it is clear that the difference between two dissociation fractions at $\xi = 0.05$ is just the difference between two effective frozen solutions in the weak portion of the curved shock wave.

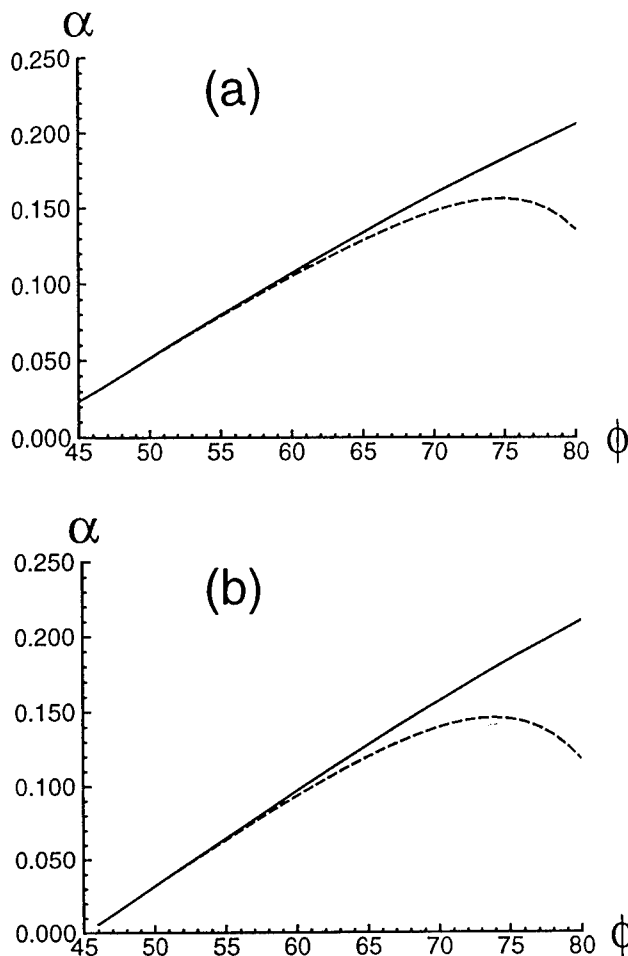


Fig. 6 Plots of effective frozen dissociation fraction α_0 and solution (4.3.4) at $\xi = 0.05$ versus incident angle ϕ for shock tunnel and equivalent flight conditions. Fig. 6 (a): Shock tunnel flow; Fig. 6 (b): Equivalent flight flow. Full line: Effective frozen dissociation fraction α_0 . Dash line: Analytic solution (4.3.4) at $\xi = 0.05$.

Near the stagnation streamline, although the effective frozen dissociation fractions are almost the same for the two flows (see Fig. 5), the solution (4.3.4) at $\xi = 0.05$ of the equivalent flight conditions is lower than that of the shock tunnel flow. This is because the higher density behind the shock, corresponding to the higher Mach number for the equivalent flight conditions, enhances the recombination rate. Note that the recombination rate is proportional to the square of the density, while the dissociation rate is proportional only to the density. This difference in the dissociation fractions may result from the large difference in the Mach number. In the strong shock portion, the influence seems to be small. In the weak shock portion, it may become a problem.

7. Conclusions

The flows considered here were for the case of the hypersonic flow after a curved shock with Lighthill-Freeman ideal dissociation gas under circumstances that the recombination rate is not negligible.

Analytic solutions are obtained for a streamline with the assumptions that the flow is 'quasi-frozen' in the region down-

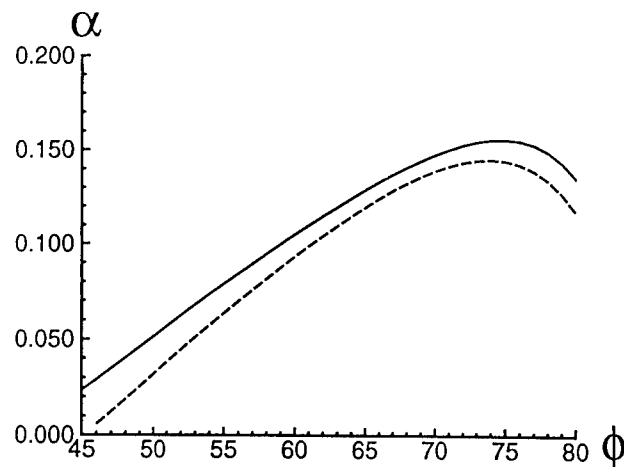


Fig. 7 Plot of solutions (4.3.4) at $\xi = 0.05$ versus incident angle ϕ for shock tunnel and equivalent flight conditions. Full line: Shock tunnel flow. Dashed line: Equivalent flight flow.

stream of a thin dissociating layer near the shock. The theory gives an explicit expression for the dissociation fraction as a function of temperature. The analytic solutions are shown to agree quite well with the results obtained with two-dimensional Euler equations using Candler's method. The dissociation fraction seems to be 'frozen' again in the downstream region of the flow in the free-piston shock tunnel, although the recombination rate is dominant. The freezing of the flow occurs because of the strong exponential temperature dependence of the dissociation reaction rate and the effect of the negative pressure gradient associated with the shock curvature upon temperature and density for both dissociation and recombination reaction rates.

An important result is that the analytic solutions offer an engineer a simple expression as a rule of thumb to check the validity of binary scaling for the experimental conditions, before doing any extensive and expensive numerical calculations and experiments. The analytic solutions can also be used to determine the limiting streamline which delineates the validity zone of binary scaling.

The effects upon the chemical nonequilibrium processes of the large difference in free stream temperature (or Mach number) between free-piston shock tunnel and equivalent flight conditions are discussed. The results indicate that for the strong shock portion, it is not a serious issue, while away from the stagnation point, it may become important. The results support Macrossan's conclusion about the Mach number effect. In many cases one can decouple this effect from the simulation of hypersonic chemical nonequilibrium flow. If one can not remove the effect of large free stream temperature difference, the results suggest the stagnation enthalpy h'_0 is a more important parameter to match than V'_∞ .

Acknowledgement

This work was supported by AFOSR Grant F49610-92-J-0110 (Dr. L. Sakell) and AFOSR grant F49620-93-1-0338 (Dr. J. Tishkoff).

References

- Candler, G.V. 1988 "The Computation of Weakly Ionized Hypersonic Flows in Thermo-Chemical Nonequilibrium," Ph.D. Thesis, Stanford University.
- Freeman, N. C. 1958 "Non-equilibrium flow of an ideal dissociating gas", *J. Fluid Mech.* **3**, 407.
- Gibson, W. E. & Marrone, P. V. 1964 "A similitude for nonequilibrium phenomena in hypersonic flight", AGARDograph **68**, 105-132.
- Hayes, W. D. & Probstein, R. F. 1966 "Hypersonic flow theory," Academic.
- Hornung, H. G. 1976 "Non-equilibrium ideal-gas dissociation after a curved shock wave", *J. Fluid Mech.*, **74**, 143-159.
- Hornung, HG 1992 "Performance data of the new free-piston shock tunnel at GALCIT", AIAA **92-3943** Nashville.
- Hornung, HG, Wen C and Candler, GV 1994 "Hypervelocity flow over spheres", *Acta Mechanica*, to appear.
- Lighthill, M. J. 1957 "Dynamics of a dissociating gas, Part I Equilibrium flow", *J. Fluid Mech.*, **2**, 1-32.
- Macrossan, M. N. 1990 "Hypervelocity flow of dissociating nitrogen downstream of a blunt nose", *J. Fluid Mech.* **217**, 167-202.
- Maus, J. R., Griffith, B. J. & Szema, K. Y. 1984 "Hypersonic Mach number and real gas effects on Space Shuttle Orbiter aerodynamics", *J. Spacecraft* ., **21**, 136.
- Park, C. 1985 "On convergence of computation of chemically reacting flows", AIAA **85-0247**.
- Vincenti, W. G. & Kruger, C. H. 1965 "Introduction to physical Gasdynamics", Wiley.

Non-equilibrium dissociating flow over spheres

By C.-Y. WEN¹ AND H. G. HORNING²

¹ Department of Mechanical Engineering, Da-Yeh Institute of Technology, Taiwan.

² Graduate Aeronautical Laboratories, California Institute of Technology, Pasadena, CA 91125, USA

(Received 27 May 1994 and in revised form 10 May 1995)

Previous work on the correlation of dissociative non-equilibrium effects on the flow field in front of blunt bodies considered the dependence of the dimensionless shock stand-off distance on the dimensionless dissociation rate immediately after the normal shock in the simple case of a diatomic gas with only one reaction. In this paper, the correlation is corrected to take into account the additional parameter of the dimensionless free-stream kinetic energy, and extended to the case of complex gas mixtures with many species and many reactions, by introducing a new reaction rate parameter that has a clear physical meaning, and leads to an approximate theory for the stand-off distance. Extensive new experimental results and numerical computations of air, nitrogen and carbon dioxide flow over spheres were obtained over a large range of total enthalpy. The results comprise surface heat flux measurements and differential interferograms. Both experimental results and numerical computations substantiate the approximate theory.

1. Introduction

When a sphere is placed in a flow at high Mach number and at such high velocity that the ordered kinetic energy of the uniform free stream is comparable with the dissociation energy of the gas, two new parameters (in addition to those of perfect-gas flows) enter the problem. In the simplest case of dissociation of a single diatomic gas, a dimensionless number of the form $K \equiv u_\infty^2/(2D)$ measures the free-stream kinetic energy in terms of the dissociation energy of the gas. Here, u_∞ is the free-stream speed and D is the specific dissociation energy of the gas.

If the gas density is sufficiently large, the collision frequency between the molecules is high and produces a dissociation rate that is fast enough to cause significant dissociation over distances that are comparable with the diameter of the sphere. In the simplest case of dissociation of a single diatomic gas, where the composition may be characterized by a single variable, e.g. the dissociation fraction α , this means that a dimensionless number of the form

$$\Omega \equiv \left(\frac{d\alpha}{dt} \right)_s \frac{d}{2u_\infty}$$

is $O(1)$. Here, the time derivative is the dissociation rate at a representative point, e.g. just after the normal shock wave, and d is the diameter of the sphere. High density is required to satisfy this condition because the dissociation rate is directly proportional to the density. Clearly, this means that the product of density and body size has to be sufficiently large. Hence, the Reynolds number of the flow is also large, and for

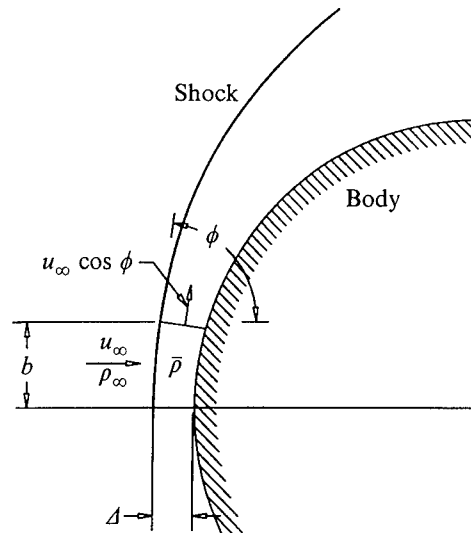


FIGURE 1. Schematic of control volume, and notation.

many purposes the flow may be considered to be inviscid to very good approximation. Infinite Ω corresponds to such a fast reaction that the flow may be considered to be in equilibrium, while zero Ω corresponds to no dissociation, or the frozen limit. For given free-stream conditions, Ω can be varied by changing the size of the body.

A well-known feature of hypervelocity blunt-body flows is that the shock wave stand-off distance Δ is inversely proportional to the average density on the stagnation streamline. This follows from a very simple argument which is presented here because it determines the right dimensionless numbers to choose for the problem. Consider the control volume shown in figure 1. Apply continuity to this control volume. At the left, the rate at which mass enters the control volume is $u_\infty \rho_\infty b$, or $\pi u_\infty \rho_\infty b^2$, depending on whether the flow is plane or axisymmetric. For small b , the rate at which mass leaves the control volume is $u_b \bar{\rho} \Delta$ or $2\pi u_b \bar{\rho} \Delta$, respectively, where $\bar{\rho}$ is the average density in the shock layer. With $u_b \approx u_\infty \cos \phi$ and $b = r_s \cos \phi$, mass balance gives

$$\frac{1}{2} \frac{\Delta}{r_s} \frac{\bar{\rho}}{\rho_\infty} = \frac{1}{4} \quad \text{and} \quad = \frac{1}{2}$$

respectively, for axisymmetric and plane flow. Here, r_s is the radius of curvature of the shock. Since the stand-off distance is small compared to the body radius, $d/2 \approx r_s$ and the dimensionless parameter on the left may be formed with the body radius instead of the shock radius. The importance of this simple argument is not in the numbers on the right, but in the fact that it brings out the importance of the average density in the shock layer.

This topic was studied theoretically and experimentally in some detail by Hornung (1972). By examining a large number of numerical computations of dissociating flow over cylinders, it was found that the dimensionless stand-off distance, in the form

$$\tilde{\Delta} \equiv \frac{\Delta}{d} \frac{\rho_s}{\rho_\infty},$$

could be correlated by plotting it against the parameter Ω . Here, ρ_s is the density immediately after the normal shock. The computed density fields in the shock layer were also shown to be correlated approximately by Ω . However, the experimental

results of that study, obtained in the free-piston shock tunnel, T3, at the Australian National University, did not corroborate the numerical correlation very well.

This earlier study suffered from two main problems. First, the theory was limited to a single diatomic gas, and did not account for the effect of K on \tilde{A} . No derivation of the correlation of \tilde{A} with Ω was given. Second, the unavoidable end-effects in experimental studies of flow over cylinders manifest themselves in just the same manner as non-equilibrium dissociation effects, so that the latter were obscured by them. Also, the facility employed probably suffered from driver-gas contamination at the highest specific enthalpies tested.

Therefore, in the present study, we have the following three aims: to perform a theoretical study to relate the stand-off distance to both Ω and K ; to seek a more general reaction rate parameter, that allows the gas to consist of many species with many reactions; and to test the results experimentally and numerically. In the experiments, the new facility T5, at GALCIT, in which the density is significantly larger than was possible in T3 so that interferograms of flow over spheres give sufficient resolution, permitted the bothersome problems associated with flow over cylinders to be avoided. In the numerical investigation, the code developed by Candler (1988) was employed.

2. Conditions along the stagnation streamline

2.1. Effect of chemical reactions

Consider the stagnation streamline along the symmetry axis between the shock and the stagnation point. The momentum and energy equations for inviscid adiabatic flow take the simple forms

$$dp + \rho u du = 0 = dh + u du,$$

where p , ρ , u , and h are pressure, density, velocity and specific enthalpy respectively. Thus,

$$dp = \rho dh.$$

This equation does not mean that the entropy is constant along the stagnation streamline, but rather that the only entropy change that occurs is that associated with the chemical reaction:

$$T ds = \sum \hat{\mu}_i dc_i,$$

where T , s are temperature and specific entropy, and the $\hat{\mu}_i$ and c_i are the chemical potentials and mass fractions of the constituents. Let the caloric equation of state be given in the form

$$h = h(p, \rho, c_i).$$

Since the mass fractions must satisfy the identity

$$\sum_{i=1}^n c_i = 1,$$

the number of mass fractions that are independent is one less than the total number n of components present. It is usually convenient to choose c_1 as a dependent variable

and the other c_i as independent variables. Thus,

$$dh = h_p d\rho + h_p dp + \sum_{i=2}^n h_{c_i} dc_i = h_p d\rho + \rho h_p dh + \sum_{i=2}^n h_{c_i} dc_i,$$

where the subscripts denote partial differentiation. Solving for $d\rho$,

$$d\rho = \frac{1 - \rho h_p}{h_p} dh - \frac{1}{h_p} \sum_{i=2}^n h_{c_i} dc_i.$$

Note that the coefficient of dh is related to the frozen speed of sound a_f , and that dh may be replaced by $-u du$. Rewriting the first term on the right of this equation accordingly, it becomes

$$\frac{d\rho}{\rho} = -\frac{u^2}{a_f^2} \frac{du}{u} - \frac{1}{\rho h_p} \sum_{i=2}^n h_{c_i} dc_i,$$

where

$$a_f^2 = \frac{-h_p}{h_p - 1/\rho}.$$

The frozen Mach number u/a_f after the normal shock is typically 0.2 or less. This means that, in the absence of dissociation, the density is practically constant along the stagnation streamline, and, with dissociation, the density change along the stagnation streamline is essentially controlled by the chemistry:

$$(d\rho)_s \approx - \left(\frac{1}{h_p} \sum_{i=2}^n h_{c_i} dc_i \right)_s.$$

This approximation makes it possible to relate the average density on the stagnation streamline to the rate at which energy is absorbed by the chemical reactions at the shock. This then appears to be the right quantity to incorporate in a new reaction rate parameter

$$\tilde{\Omega} \equiv -\frac{d}{\rho_s u_\infty} \left(\frac{1}{h_p} \sum_{i=2}^n h_{c_i} \frac{dc_i}{dt} \right)_s.$$

For a given gas mixture,

$$\tilde{\Omega} \sim \rho_s d \left(\sum_{i=2}^n h_{c_i} \frac{dc_i}{dt} \right)_s / (\rho_\infty u_\infty^3),$$

which has the physical significance of

$$\tilde{\Omega} = \frac{\text{Energy absorption rate by chemistry}}{\text{Input rate of free-stream kinetic energy}}.$$

In order to determine the value of $\tilde{\Omega}$ it is necessary to express h_p in terms of the conditions at the shock. This may be done by assuming that the gas mixture obeys the thermal equation of state

$$T = T(p, \rho, c_i) = \frac{p}{\rho R \Gamma},$$

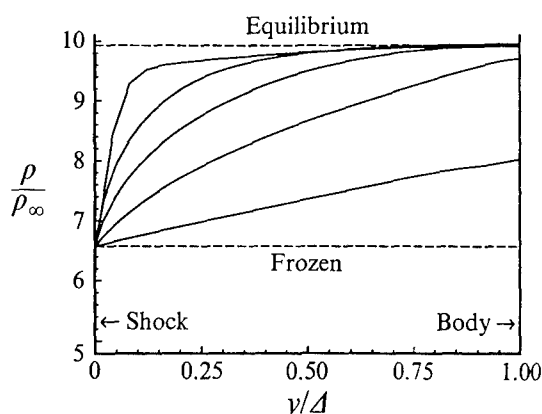


FIGURE 2. Density profile along the stagnation streamline from numerical computations for different values of the reaction rate parameter.

where

$$\Gamma = \sum_{i=1}^n \frac{c_i}{W_i} = \frac{1}{W},$$

and W_i and W are the molecular weights of species i and of the dissociated gas mixture, respectively. This leads to

$$h_p = -\frac{c_p p}{\rho^2 R \Gamma},$$

where

$$c_p = \sum_{i=1}^n c_i c_{pi},$$

and the c_{pi} are the specific heats at constant pressure of the constituents. The value of h_p at the shock can be estimated by approximating the value of p_s with $\rho_\infty u_\infty^2$, so that

$$(h_p)_s = -\frac{c_{ps} \rho_\infty u_\infty^2}{\rho_s^2 R \Gamma}.$$

2.2. Density profile

Figure 2 shows seven density profiles along the stagnation streamline obtained using an inviscid version of Candler's code plotted against y/Δ , where y is the distance from the shock. The free-stream conditions for these different profiles were the same, and the changes are brought about by successively increasing the sphere diameter. As may be seen, the profile changes in a monotonic fashion from the frozen-flow profile, with virtually constant density, to the equilibrium profile, in which all the dissociation, and therefore all the density change, occurs in the shock, and the density is again virtually constant thereafter.

Recall that the quantity that determines the stand-off distance is the average density. In fact, numerous correlations of stand-off distance with average density have been made for non-reacting flow. Upon interpretation into our variables, these give the following result:

$$\frac{\Delta}{d} \frac{\bar{\rho}}{\rho_\infty} = \tilde{\Delta} \frac{\bar{\rho}}{\rho_s} = L.$$

where $L = 0.41$ for spheres.

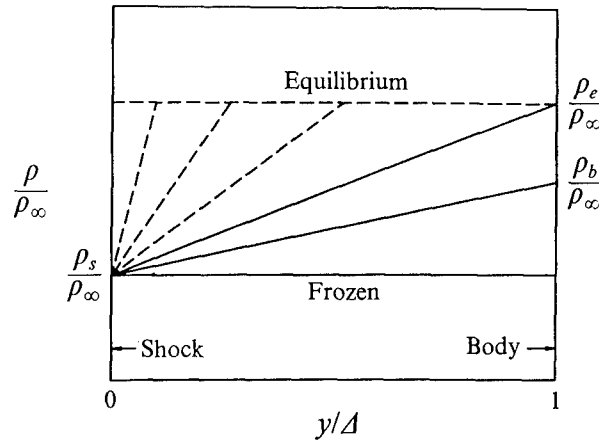


FIGURE 3. Simplified density profiles for the purpose of determining an approximate average value of the density along the stagnation streamline. ρ_b and ρ_e denote the stagnation-point density and the equilibrium density, respectively. By comparing with Fig. 2, it is clear that using this linear approximation will overestimate the average density slightly, because the actual profiles are always convex up.

Because the stand-off distance is related to the average density, the exact details of the density profile are not important and we can proceed in an approximate Kármán-Pohlhausen-type analysis by assuming linear density profiles between the shock and the body, provided that the density on the body ρ_b is smaller than the equilibrium density ρ_e . If the linear profile reaches ρ_e before the stagnation point, the density is taken to be constant thereafter at ρ_e . This clearly requires the equilibrium density to be determined and is evidently the place where the dependence of $\tilde{\Delta}$ on K (and therefore the recombination reaction) enters.

To proceed with the analysis, distinguish the cases where $\rho_b < \rho_e$ from those in which the body density is ρ_e . The slope of the density profile at the shock is determined from the dissociation rate just downstream of the shock. Figure 3 shows the simplified linear profiles.

3. Analytic solution for the stand-off distance

3.1. The case when $\rho_b < \rho_e$

When $\rho_b < \rho_e$, the linear profiles give

$$\left(\frac{d\rho}{dy}\right)_s = \frac{\rho_b - \rho_s}{\Delta} \quad \text{and} \quad \bar{\rho} = \frac{1}{2}(\rho_b + \rho_s) ;$$

$(d\rho/dt)_s$ can then be approximated as

$$\left(\frac{d\rho}{dt}\right)_s = u_s \left(\frac{d\rho}{dy}\right)_s = (\rho_b - \rho_s) \left(\frac{\rho_\infty}{\rho_s} \frac{d}{\Delta}\right) \left(\frac{u_\infty}{d}\right) .$$

Using the definition of $\tilde{\Omega}$ to replace $(d\rho/dt)_s$ leads to the quadratic equation for $\tilde{\Delta}$

$$\tilde{\Delta}^2 - (L - \tilde{\Delta}) \frac{2}{\tilde{\Omega}} = 0 .$$

Only one of the two roots of this equation is physically meaningful. It is

$$\tilde{\Delta} = \frac{1}{\tilde{\Omega}} \left[-1 + \left(1 + 2L\tilde{\Omega} \right)^{1/2} \right] . \quad (3.1)$$

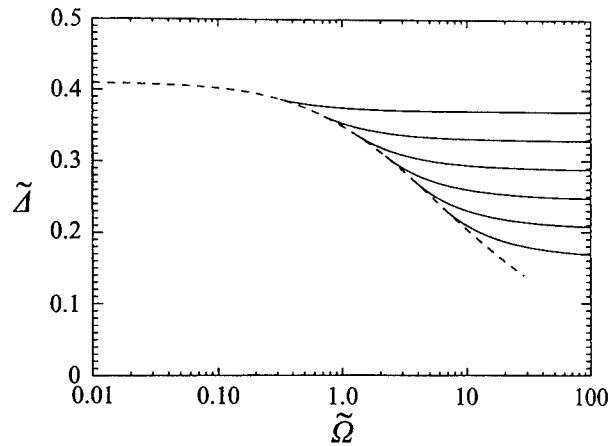


FIGURE 4. Plot of equations (3.1) (dashed line), and (3.2) (full lines) for $\rho_s/\rho_e = 0.4, 0.5, 0.6, 0.7, 0.8$ and 0.9 .

This has the correct limit $\tilde{A} = L$ at $\tilde{\Omega} = 0$, but will clearly fail at large $\tilde{\Omega}$, because we have to proceed differently in calculating $\bar{\rho}$ when the linear profile reaches the equilibrium density within the shock layer.

3.2. The case when $\rho_b = \rho_e$

For values of $\tilde{\Omega}$ that are sufficiently small, so that $\rho_b < \rho_e$, the previous section shows that \tilde{A} depends only on $\tilde{\Omega}$. When $\rho_b = \rho_e$, however, this is no longer true, since the equilibrium value of the density now enters the calculation of $\bar{\rho}$. Thus, a critical value of $\tilde{\Omega}$ exists for each free-stream condition, beyond which \tilde{A} depends on two parameters, changing in form

$$\text{from } \tilde{A} = f(\tilde{\Omega}) \text{ to } \tilde{A} = g(\tilde{\Omega}, \rho_e/\rho_s).$$

By proceeding as in the previous section, but this time forming the average density from the linear profile up to the point where ρ reaches ρ_e and a constant-density part with $\rho = \rho_e$ thereafter, the average density becomes

$$\frac{\bar{\rho}}{\rho_s} = \frac{\rho_e}{\rho_s} - \frac{1}{2\tilde{\Omega}\tilde{A}} \left(1 - \frac{\rho_e}{\rho_s}\right)^2.$$

By using the relation between the average density and the stand-off distance, and solving for \tilde{A} , we obtain

$$\tilde{A} = \frac{\rho_s}{\rho_e} \left[L + \frac{1}{2\tilde{\Omega}} \left(\frac{\rho_e}{\rho_s} - 1 \right)^2 \right]. \quad (3.2)$$

Again, this may be seen to have the correct limiting value $L\rho_s/\rho_e$ when $\tilde{\Omega} = \infty$.

Equations (3.1) and (3.2) are plotted in figure 4. The curves of the two-parameter family of equation (3.2), valid for large $\tilde{\Omega}$, are nearly tangent to the single curve of equation (3.1), valid for small $\tilde{\Omega}$ at the transition point, which is different for different ρ_s/ρ_e .

The coordinates of the transition point $(\tilde{\Omega}_0, \tilde{A}_0)$, can be determined explicitly as

$$\tilde{\Omega}_0 = \frac{(\rho_e/\rho_s)^2 - 1}{2L},$$

and

$$\tilde{\Delta}_0 = \frac{2L}{\rho_e/\rho_s + 1}.$$

The slopes of the two curves are not quite the same at this point. This may be seen from the fact that the average density increases less rapidly with $\tilde{\Omega}$ when the equilibrium density is reached before the stagnation point than if $\rho_e > \rho_b$ (see figure 3).

3.3. Discussion

The approximate theory leading to equations (3.1) and (3.2) takes account of the free-stream kinetic energy K through the appearance of the equilibrium density ρ_e . This is therefore the place where the effect of the recombination reactions enters the picture. For higher values of K , i.e. higher values of the total enthalpy h_0 , the amount of energy absorbed by dissociation to equilibrium is increased, so that ρ_e/ρ_s is increased, and $\tilde{\Delta}$ is decreased. The approximate theory takes all of these effects into account in the simplest approximation. The two-part approximation of the density profile (linear plus constant) makes it necessary to distinguish between the regimes of low and high $\tilde{\Omega}$ with the two equations (3.1) and (3.2).

The two-part approximation also overestimates the average density and therefore underestimates the stand-off distance, as will be seen later. This error may be reduced significantly if the approximation for the density profile is improved, for example, by writing it as

$$\frac{\rho - \rho_s}{\rho_e - \rho_s} = 1 - \exp \left[-\frac{2\tilde{\Omega}\rho_s}{\rho_e - \rho_s} \frac{y}{\tilde{\Delta}} \right].$$

Integrating this to determine the average leads to

$$\frac{\bar{\rho} - \rho_s}{\rho_e - \rho_s} = 1 + \frac{1}{2\tilde{\Omega}\tilde{\Delta}} \left(\frac{\rho_e}{\rho_s} - 1 \right) \left(\exp \left[-\frac{2\tilde{\Omega}\tilde{\Delta}\rho_s}{\rho_e - \rho_s} \right] - 1 \right).$$

This is now a single equation for the average density, from which a single equation for $\tilde{\Delta}$ can be obtained by substituting in

$$\tilde{\Delta} = L \frac{\rho_s}{\bar{\rho}},$$

and solving the resulting equation for $\tilde{\Delta}$. In this case, an explicit solution is not possible, except in the two limiting cases, where the results are, of course, the same as equations (3.1) and (3.2). This refined theory is more accurate in the mid-range of $\tilde{\Omega}$. However, the simple forms of equations (3.1) and (3.2) are surprisingly accurate and the theory is much more transparent in this simpler form.

The manner in which the stand-off distance may be described in terms of the two parameters K and $\tilde{\Omega}$ is, of course, also of wider significance. It may be expected, for example, that, for a given gas, the density field in the shock layer of a blunt body will be the same for all flows in which these two parameters take the same value. The stand-off distance just serves as a convenient variable to test this concept. The success of the simple correlation stems from the fact that the influence of the chemistry on the fluid motion acts through the removal or addition of energy to or from the chemical energy store represented by the dissociated species. Thus, the important step in the

analysis is to express \tilde{Q} in terms of the dimensionless chemical energy absorption rate.

4. Computational method

The code developed by Candler (1988) was used to compute the inviscid reacting flow over a sphere. The flow field is described by coupled partial differential equations for the conservation of species, mass, mass-averaged momentum, vibrational energy of each diatomic species and total energy. A finite-volume method using modified Steger–Warming flux-vector splitting is used to obtain the steady-state solution to these fully coupled equations for different gases. Park's semi-empirical two-temperature model and chemical kinetics model (Park 1988, 1989) was used to calculate the reaction rates for different reactions of air and nitrogen. For carbon dioxide, the chemical kinetics model of Park *et al.* (1991) was used. The scheme is implicit, using Gauss–Seidel line relaxation and is second-order accurate in the tangential direction. A compromise between efficiency in computational time and accuracy led to the use of a (56×100) grid throughout the present work. Extensive documentation of successful examples exists in reproducing experimental results in great detail, see e.g. Candler (1988), Rock, Candler & Hornung (1992), Wen & Hornung (1993), and Hornung *et al.* (1994). Since the shock values of temperature, vibrational temperatures, and density are not accessible during the experiment, the computational method provides a good way to obtain partial information about them.

The stand-off distance and the shock values of the reaction rate and density for the numerical calculation are determined from the point where the vibrational temperature reaches a maximum.

5. Experiment

5.1. Facility

The facility used for all the experiments described here was the free-piston shock tunnel T5 at GALCIT. The facility uses the principle of free-piston adiabatic compression of the driver gas of a shock tunnel to achieve the high shock speeds and densities required to generate high enthalpy and reaction scaling. It is capable of producing flows of air or nitrogen up to specific reservoir enthalpy h_0 of 25 MJ kg^{-1} at reservoir pressure p_0 up to 100 MPa. The shock tunnel has two additional important features. One is that the test duration is sufficiently short to avoid destruction of the machine by melting, yet long enough to provide good measurements during the steady-flow period. The other is that the gas is partially dissociated at the nozzle exit, especially in the cases of air and carbon dioxide at high specific reservoir enthalpies, where these gases also contain, respectively, some nitric oxide and carbon monoxide. A more detailed description of T5 and its performance envelope, flow quality and repeatability may be found in Hornung (1992).

5.2. Free-stream conditions

For the experiments, the flow was generated through a contoured nozzle of 300 mm exit diameter and 30 mm throat diameter. Using an equilibrium calculation, the specific reservoir enthalpy can be determined from the measured shock speed and the measured reservoir pressure. The nozzle flow is then computed by using an axisymmetric inviscid non-equilibrium flow code developed by Rein (1989). The calibration

	p_0 (MPa)	h_0 (MJ kg ⁻¹)	u_∞ (km s ⁻¹)	T_∞ (K)	ρ_∞ (kg m ⁻³)
Nitrogen from	30	10.58	4.2	1390	0.0175
to	90	21.06	5.5	2760	0.0561
Air from	30	9.81	3.9	1340	0.0152
to	90	22.15	5.6	2930	0.0627
Carbon dioxide from	30	4.5	2.5	1130	0.0326
to	90	11.95	3.6	2400	0.162

TABLE 1. Range of reservoir and free-stream conditions

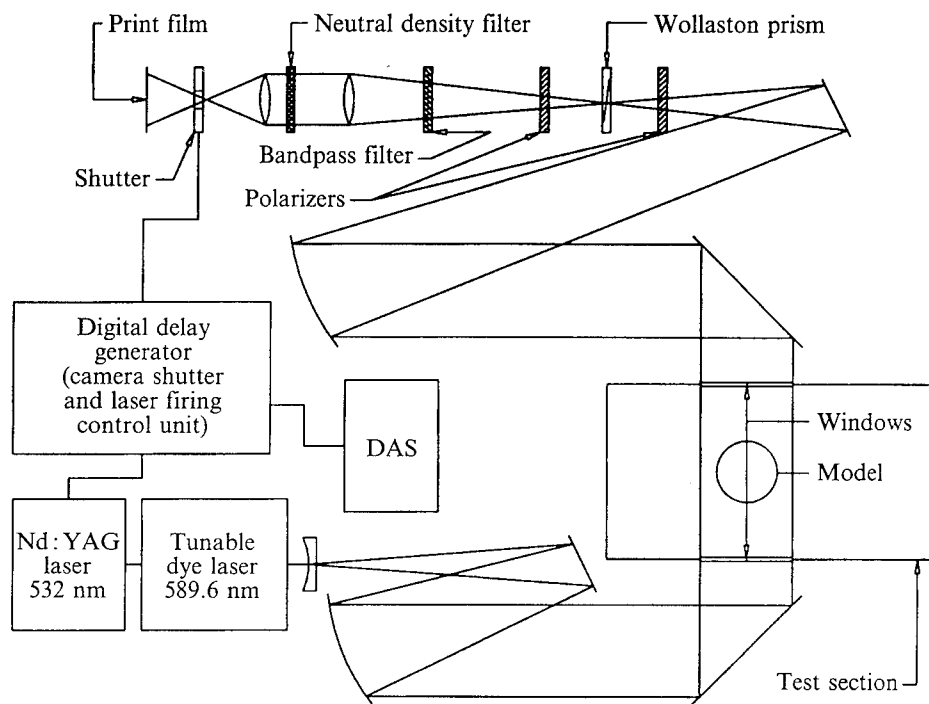


FIGURE 5. Schematic diagram of the optical arrangement. Bandpass and spatial filters are used to reduce the luminosity emitted from the test gas. The bandwidth of the bandpass filter is 10 nm centred at 590 nm for the dye laser and 10 nm centred at 532 nm for the neodymium-YAG laser.

of the free-stream conditions obtained by this method has been accomplished by measuring test section Pitot pressure distribution, see Rousset (1994) and stagnation-point heat flux, see Wen (1994).

Table 1 gives the ranges of values of the reservoir and test section conditions chosen for the present investigation. The Mach number of the free stream is about 5.5 for nitrogen, 5.3 for air and 4.6 for carbon dioxide.

5.3. Models and flow visualization

The models were spheres with diameters 1, 2, 3, 4 and 6 in. in order to vary the reaction rate parameter at a given tunnel condition. This has an upper limit of 6 in.

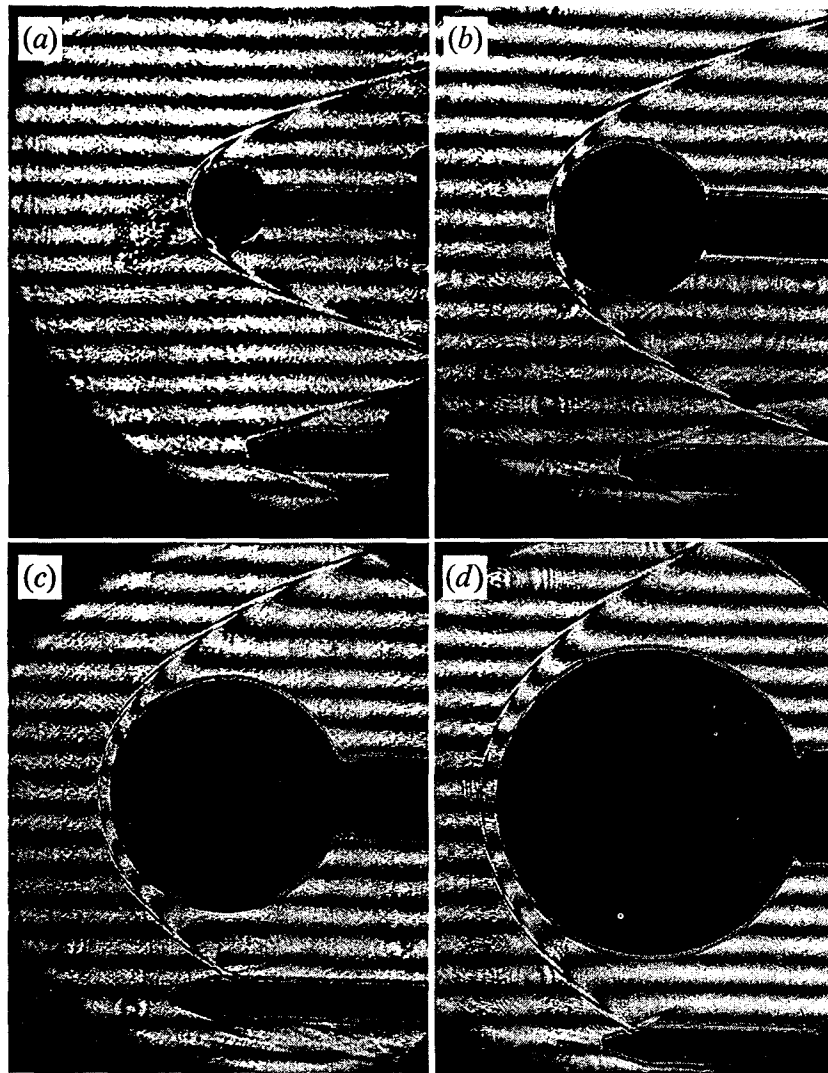


FIGURE 6. Finite fringe differential interferograms of air flow over 1, 2, 3 and 4 in. diameter spheres. $\lambda = 589$ nm. (a) $p_0 = 58$ MPa, $h_0 = 10.7$ MJ kg⁻¹. (b) $p_0 = 25$ MPa, $h_0 = 9.8$ MJ kg⁻¹. (c) $p_0 = 28$ MPa, $h_0 = 10$ MJ kg⁻¹. (d) $p_0 = 27.5$ MPa, $h_0 = 16$ MJ kg⁻¹. The blemish ahead of the bow shock wave in interferograms (a) and (b) is due to a flaw in the optical window.

because of the useful diameter of the flow, and a lower limit of 1 in. because of the resolution of the optical system. The spheres were instrumented with thermocouples to measure the surface temperature history and thus the surface heat flux, in particular at the stagnation point.

The optical system used for flow visualization is a differential interferometer shown schematically in figure 5. This instrument uses a Wollaston prism in a conventional schlieren setup and was used in the finite-fringe mode with a dye laser producing 5 mJ pulses of 6 ns duration.

6. Results

6.1. Density field

As an example of the interferometric results obtained, figure 6 shows a set of four finite-fringe differential interferograms of air flow over four different-size spheres, and figure 7 shows five cases of carbon dioxide flow. A large number of such measurements

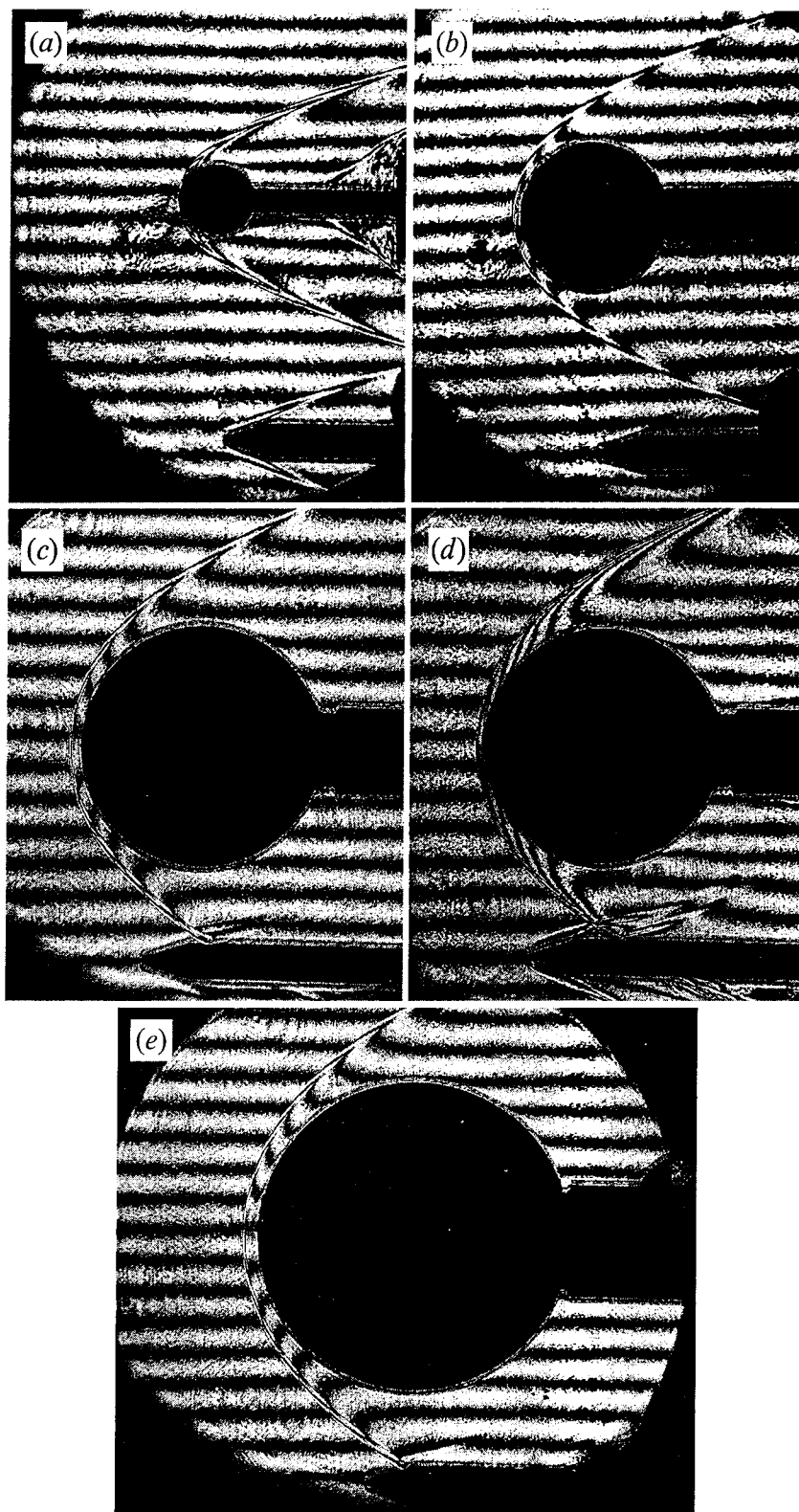


FIGURE 7. Finite fringe differential interferograms of CO₂ flow over 1, 2, 3, 3, and 4 in. diameter spheres. $\lambda = 589$ nm. (a) $p_0 = 55$ MPa, $h_0 = 6$ MJ kg⁻¹. (b) $p_0 = 25$ MPa, $h_0 = 12$ MJ kg⁻¹. (c) $p_0 = 25$ MPa, $h_0 = 9$ MJ kg⁻¹. (d) $p_0 = 55$ MPa, $h_0 = 4.6$ MJ kg⁻¹. (e) $p_0 = 22.5$ MPa, $h_0 = 11.4$ MJ kg⁻¹.

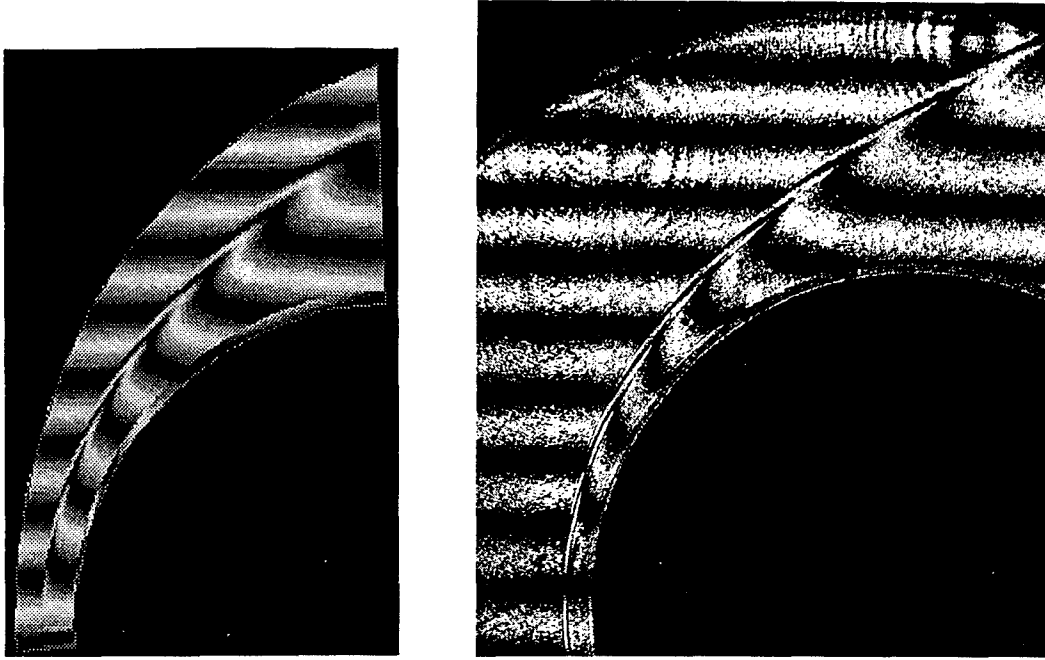


FIGURE 8. Comparison of measured (right) and computed differential interferograms in the case of air flow over a 4 in. sphere, at $p_0 = 27.5$ MPa, $h_0 = 16$ MJ kg⁻¹.

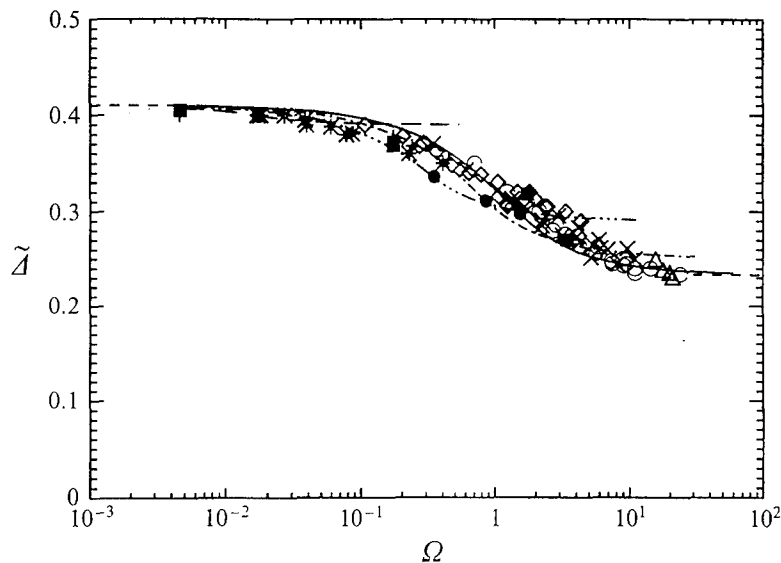


FIGURE 9. Numerical (open symbols) and experimental (full squares) results for nitrogen flow plotted in the old variables, with equations (3.1) and (3.2) superimposed. As may be seen, in these variables, the curves for different ρ_s/ρ_e are shifted relative to each other.

were taken, and compared with numerically computed interferograms. An example of such a comparison is presented in figure 8. Extensive comparisons of this kind have been made. More detail about the results of such comparisons are reported elsewhere, see e.g. Wen (1994) and Hornung, Wen & Candler (1994), Hornung (1994).

6.2. Stand-off distance

If equations (3.1) and (3.2) are plotted in the form \tilde{Z} vs. the old reaction rate parameter Ω , in the only case where Ω can meaningfully be defined, i.e. for nitrogen,

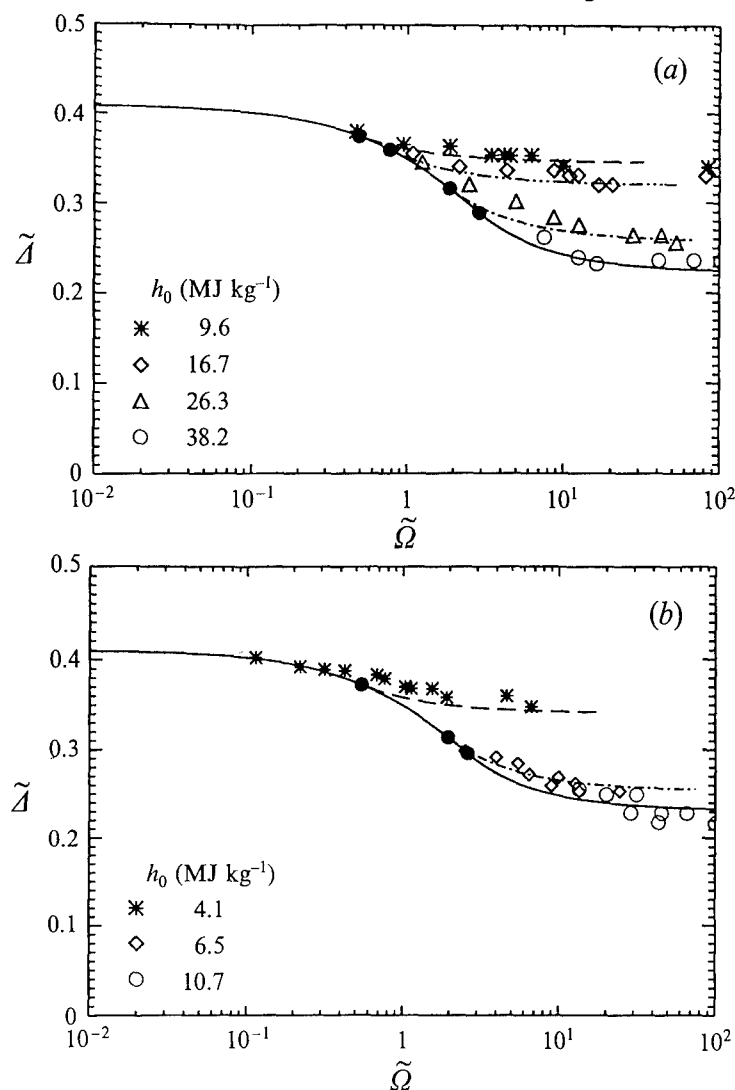


FIGURE 10. Plot of equations (3.1) and (3.2) for selected values of h_0 , resulting in different values of ρ_s/ρ_e . The symbols represent computational results for (a) air (b) carbon dioxide. The full circles are the junction points of equation (3.1) and equation (3.2). Note that the theory underestimates the stand-off distance slightly, consistently with the overestimate of the average density.

the situation presented in figure 9 results. The manner in which this causes the curves for different values of ρ_s/ρ_e to be shifted relative to each other is the reason why the mistake of thinking that only one correlating parameter, $\tilde{\Omega}$, is required, is easily made. The difference becomes clear when the results are plotted against $\tilde{\Omega}$, as in figure 10(a) which presents computational results for the case of air. Note that the value of ρ_s/ρ_e depends on h_0 . Similar results are presented in figure 10(b) for carbon dioxide flows.

In these two plots the slight underestimate of the stand-off distance by the theory that results from the overestimate of the average density is evident in the mid-range of $\tilde{\Omega}$.

Next, we compare the experimentally measured stand-off distance in both these gases with the approximate theory, see figures 11(a) and 11(b). In the case of air, the effect appears to be much smaller than is the case in figure 10(a). This is because the highest value of the enthalpy in the computed cases is 38.2 MJ kg^{-1} , whereas the experiments only range up to 20.6 MJ kg^{-1} . Clearly, the nitrogen in the air is not

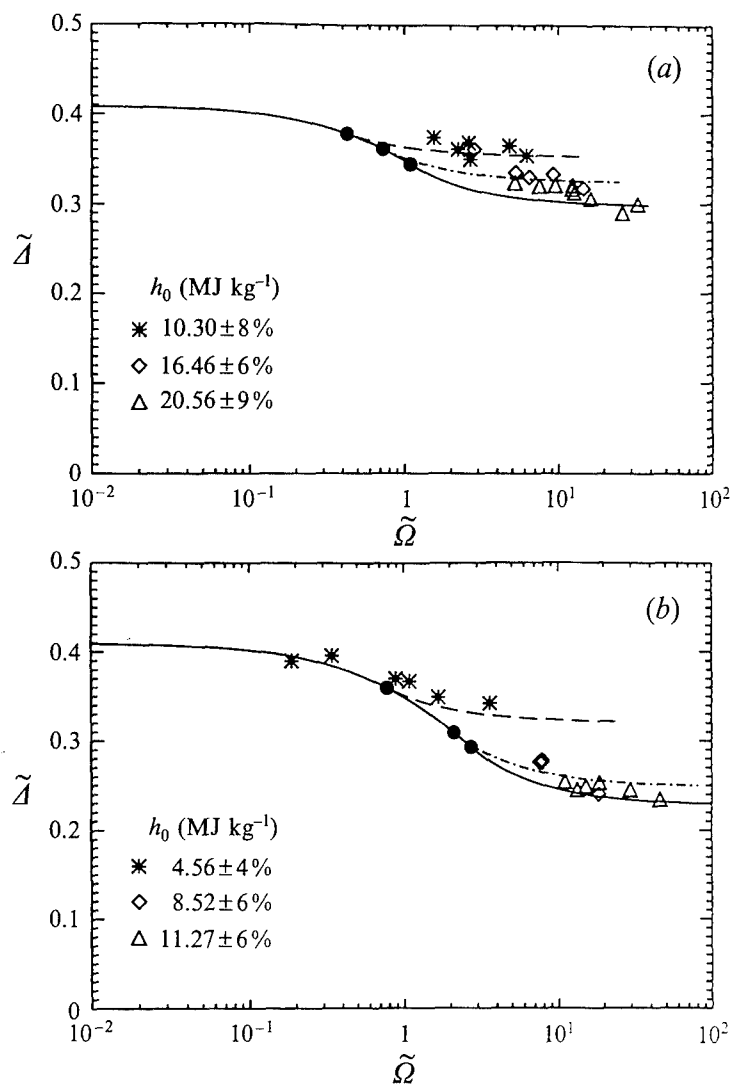


FIGURE 11. Comparison of measured dimensionless stand-off distance with the analytical theory in the case of (a) air flows (b) carbon dioxide flows.

fully dissociated at the latter value. In the case of carbon dioxide, the effect is more dramatic, because it has lower dissociation energies. In the case of air, it may also be seen that most of our experiments were conducted at conditions that are fairly close to equilibrium, since the points all lie on the large- $\tilde{\Omega}$ branch of the theory.

6.3. Stagnation-point heat flux

It remains to present an example of the measured stagnation-point heat flux. The high enthalpies of the flows studied can produce quite substantial values of this quantity. For example, on the small sphere, values up to 30 MW m $^{-2}$ were obtained. The importance of measuring this quantity lies partly in the need to substantiate the reservoir specific enthalpy, h_0 , which is determined indirectly from the measured shock speed in the shock tube. Figure 12 shows measurements of the stagnation-point heat flux in dimensionless form (Stanton number) plotted against the free-stream Reynolds number based on the sphere diameter for three different gases. These are compared with appropriate predictions from the correlation according to Fay & Riddell (1958). The flow and surface conditions are such that full recombination of the dissociated species may be expected to occur. (Catalytic surface.) While the experiments show

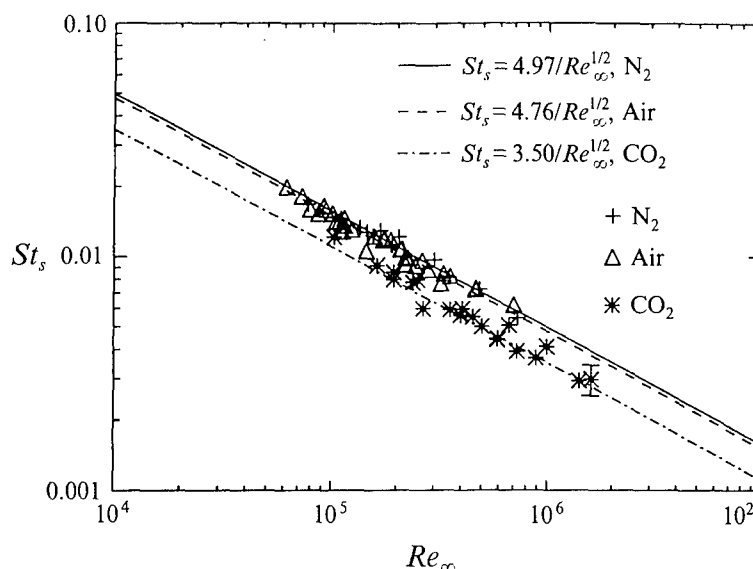


FIGURE 12. Comparison of measured dimensionless stagnation-point heat flux (symbols) with Fay & Riddell's correlation.

substantial scatter, the differences between the different gases are significant and follow the predicted differences. This provides some confirmation of the indirectly determined value of h_0 .

7. Conclusions

Theoretical, numerical and experimental results on the hypervelocity dissociating flow of nitrogen, air and carbon dioxide over spheres have been presented. An approximate theory relating the dimensionless shock stand-off distance to the dimensionless total enthalpy and a reaction rate parameter corrects and extends previous relations of this kind. A previous correlation did not take into account the effects of recombination reactions which appear through the total enthalpy parameter, nor could it deal with mixtures comprising many species with many reactions. By introducing a reaction rate parameter that is a measure of the rate of energy absorption by chemical reactions immediately behind the normal shock, scaled by the rate of input of kinetic energy, it is possible to deal with complex mixtures.

Experimental results from the hypervelocity shock tunnel T5 and numerical computations support the approximate theory and give detailed information about the flow field in the form of measured and computed differential interferograms as well as stagnation-point heat transfer data.

The work leading to the material presented in this paper was sponsored by AFOSR URI grant F49620-93-1-0338 (Dr J. Tishkoff).

REFERENCES

- CANDLER, G. V. 1988 The computation of weakly ionized hypersonic flows in thermo-chemical non-equilibrium. PhD thesis, Stanford University.
- CANDLER, G. V. & MACCORMACK, R. W. 1988 The computation of hypersonic ionized flows in chemical and thermal non-equilibrium. *AIAA Paper* 87-1546.
- FAY, J. A. & RIDDELL, F. R. 1958 Theory of stagnation point heat transfer in dissociated air. *J. Aero. Sci.* **25**, 73-85.

- HORNUNG, H. G. 1972 Non-equilibrium dissociating nitrogen flows over spheres and circular cylinders. *J. Fluid Mech.* **53**, 149–176.
- HORNUNG, H. G. 1992 Performance data of the new free-piston shock tunnel at GALCIT. *AIAA Paper* 92-3943.
- HORNUNG, H. G., CUMMINGS, E. B., GERMAIN, P., SANDERSON, S. R., STURTEVANT, B. & WEN, C.-Y. 1994 Recent results from hypervelocity research in T5. *AIAA Paper* 94-2523.
- HORNUNG, H. G., WEN, C. & CANDLER, G. V. 1994 Hypervelocity flow over spheres. *Acta Mechanica* [Suppl] **4**, 163–170.
- PARK, C. 1988 Assessment of a two-temperature kinetic model for dissociating and weakly ionizing nitrogen. *J. Thermophys. Heat Transfer* **2**, 8–16.
- PARK, C. 1989 Assessment of a two-temperature kinetic model for ionizing air. *J. Thermophys. Heat Transfer* **3**, 233–244.
- PARK, C., JAFFE, J., HOWE, J. & CANDLER, G. V. 1991 Chemical kinetic problems of future NASA missions. *AIAA Paper* 91-0464.
- REIN, M. 1989 SURF: A program for calculating inviscid supersonic reacting flows in nozzles. *GALCIT Rep. FM 89-1* (see also *Phys. Fluids A* **4**, 873–886, 1992).
- ROCK, S. G., CANDLER, G. V. & HORNUNG, H. G. 1992 Analysis of thermo-chemical non-equilibrium models for carbon dioxide flows. *AIAA Paper* 92-2852.
- ROUSSET, B. 1995 Calibration and study of the contoured nozzle of the T5 free-piston hypervelocity shock tunnel. AeE thesis, Graduate Aeronautical Laboratories, Caltech.
- WEN C.-Y. 1994 Hypervelocity flow over spheres. PhD thesis, Graduate Aeronautical Laboratories, Caltech.
- WEN, C. & HORNUNG, H. G. 1993 Experiments on hypervelocity dissociating flow over spheres. *Proc. 19th Intl Symp. on Shock Waves, Marseille*, to appear.

Experiments on Hypervelocity Dissociating Flow over Spheres

Chihyung Wen and Hans Hornung

Graduate Aeronautical Laboratories, California Institute of Technology

Abstract. This paper presents the experimental results of measurements of the stagnation point heat transfer rates experienced by spherical models of 1, 2, 3, 4 and 6 inch diameter in nitrogen, air and carbon dioxide at stagnation enthalpies ranging from 4 to 22 MJ/kg and stagnation pressures from 25 to 80 MPa. The experimental results are compared with existing results obtained in the ballistic range facility at NASA Ames and also with numerical calculations. The experimental results obtained by optical differential interferometry were compared with the images constructed from flowfields computed using the method of Candler (1988). Good agreement of fringe pattern and shock shape was observed. A novel flow visualization technique using sodium seeding to increase the sensitivity of conventional shadowgraphic techniques by resonant enhancement of the refractivity of the medium was also used. The resonantly-enhanced shadowgraph suggests a possible way of visualizing the vortical structure induced by the strong entropy layer.

Key words: Hypervelocity, Blunt body flow, Experiment

1. Introduction

Most of the experimental results on heat transfer rates through highly cooled boundary layers on spheres have been obtained from measurements made in shock tubes. These experiments correctly simulate the stagnation enthalpy which is the parameter of major interest in heat transfer measurements. However, the Reynolds number and Mach number are always low. The free piston shock tunnel T5 can simulate the Reynolds number to about one million and stagnation enthalpy to about 25 MJ/kg. The actual size of the model is also much bigger than that used in the shock tube, so that nonequilibrium effects can be studied without the constraint of the size of the model. Numerical methods for the computation of blunt body flow fields have also become very much quicker, so that even interferograms of three-dimensional chemically reacting flows can be computed with reasonable speeds. For laminar flow, the viscous case is also accessible, so that heating rates may also be compared with experimental measurements and theoretical models, see e.g. Candler (1988).

In the work presented here the aim was to gather new data on blunt body flows and to compare them with numerical computations. In addition, a goal was to look for one of the interesting features of hypervelocity blunt-body flows, namely the vorticity concentration associated with the edge of the high-entropy layer generated in the nose region by the curved shock with resonantly-enhanced shadowgraphy.

2. Experiment

2.1. Facility

The GALCIT free piston shock tunnel T5 was used for the experiments. The facility uses the principle of free-piston adiabatic compression of the driver gas of a shock tunnel to achieve the high shock speeds and densities required to generate high enthalpy and reaction scaling. The shock tunnel has the additional essential feature that the test duration is sufficiently short to avoid destruction of the machine by melting, yet long enough to provide good measurements during the steady-flow period. A more detailed description of T5 and its performance envelope, flow quality and repeatability may be found in Hornung (1992).

2.2. Freestream conditions

For the experiments, the flow was generated through a contoured nozzle of 300 mm exit diameter and 30 mm diameter throat. The reservoir specific enthalpy is determined from the measured shock speed and the measured reservoir pressure, using an equilibrium calculation. The nozzle flow is then computed from this and the measured reservoir pressure by using an axisymmetric inviscid non-equilibrium flow code developed by Rein (1989). For the present experiments, the reservoir enthalpy varied between 4.5 MJ/kg to 22.0 MJ/kg, giving free stream velocities in the range from 2.5 km/s to 5.6 km/s. The Reynolds number based on the model diameter ranged from 7.26×10^4 to 1.60×10^6 . Air, nitrogen and CO₂ were used as test gases. The latter gas is of interest in Martian atmospheric entry, where the atmosphere is composed primarily of CO₂. It also exhibits more dramatic real-gas effects than air or nitrogen, because of the large fraction of energy that goes into vibration and dissociation.

2.3. Instrumentation, data reduction and accuracy

Four Medtherm coaxial thermocouples of type E (chromel-constantan) were mounted flush with the surface of the sphere to measure the heat transfer distribution. They are 1.6 mm in diameter and are mounted at the stagnation point and 20°, 40° and 60° from the stagnation point. Only stagnation point heat transfer rate measurements will be presented here. The junction was formed by gently sanding the surface to be exposed to the flow. The cold junction was the feed-through plate for signal cables between the test section and the laboratory.

The one-dimensional semi-infinite slab theory was used to reduce the time history of the surface temperature to heat flux, given that the test time is short compared to the heat penetration time into the gauge (see Schultz and Jones, 1973):

$$\dot{q}(t) = \sqrt{\frac{\rho c k}{\pi}} \int_0^t \frac{dT(\tau)}{d\tau} \frac{d\tau}{\sqrt{t-\tau}},$$

where the thermal product $\sqrt{\rho c k}$ for the gauge material was determined to be 8919 W/(mK). The indirect method was used to process these data numerically, in which integration was performed first and then the differentiation. The accuracy was assessed to be of the order of 15% and the response time of 0.1 microsecond was advertised by the manufacturer, Medtherm Corp., more than adequate for the test time of T5, which is about 1.5 ms.

2.4. Flow visualization

Two flow visualization techniques were used for the experiment. Differential interferometry using a Wollaston prism with a divergence angle of 34" was used throughout most of the experiments. In the last five shots, resonantly-enhanced shadowgraphy with sodium seeding was used to see the boundary layer structure along the wall of the model in the first place. For more information about the resonantly-enhanced technique see Germain, Cummings and Hornung (1993). The flow was seeded by painting a very thin layer of a saturated saline solution in a small spot at the nose of the sphere. This was then left to dry, so that a thin film of salt was left to be ablated during the test. The light source used was a tunable dye laser pumped by a neodymium-YAG laser. The wavelength is about 589 nm with a bandwidth of 3 GHz which is tuned to be just off the center of one of the sodium D-lines.

3. Computational method

Candler's code was used to construct the inviscid reacting flow over a sphere. This program uses a finite-volume method. The flow field is described by coupled partial differential equations for the conservation of species, mass, mass-averaged momentum, vibrational energy of each diatomic species and total energy. The steady-state solution to these fully coupled equations is obtained

for different gases characterized by a two-temperature model using an implicit Gauss-Seidel line relaxation technique. The code is also set up for viscous flow. The inviscid code was used to obtain the conditions at the edge of the boundary layer for the theoretical heat flux predictions and to construct the computational differential interferograms for comparison with the experimental pictures. For more details, see Hornung, Wen and Candler (1993). The viscous code was used to compute the heat transfer rate along the wall of the model.

4. Results and discussion

Figs.1(a) and 1(b) show the comparison of experimental and computational interferograms for the cases of air and CO₂. The comparison shows excellent agreement.

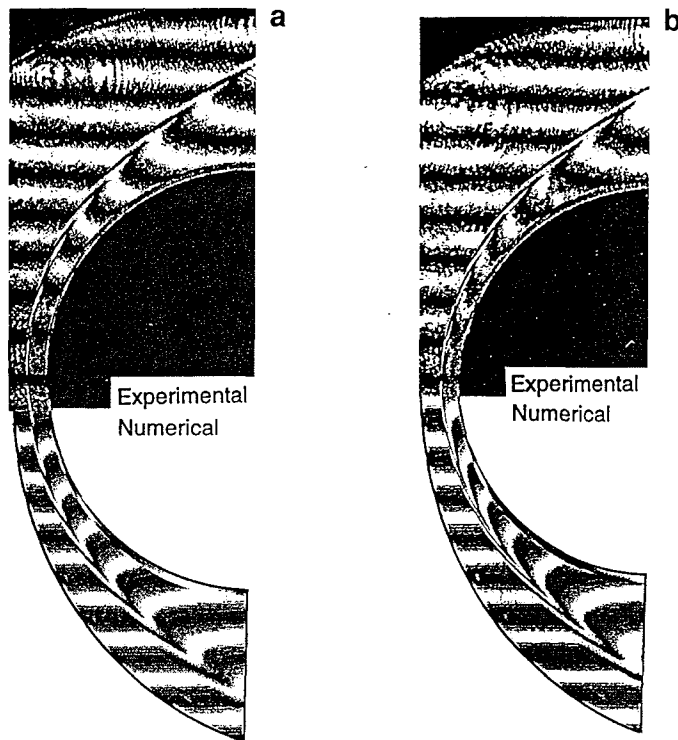


Fig. 1. Comparison of experimental and computed differential interferograms of air and CO₂ flow over a sphere of 4 in diameter. (a): air, freestream: 4.86 km/s, 0.0199 kg/m³, 16.0 MJ/kg. (b): CO₂, 3.49 km/s, 0.0326 kg/m³, 11.35 MJ/kg

One of the main purposes of the present experiments was to measure stagnation point heat transfer rates in air, N₂ and CO₂. For laminar boundary layer flow, Lees (1956) and Fay and Riddell (1958) have predicted the following dependence:

$$St_s \sim \frac{1}{\sqrt{Re_\infty}},$$

where St_s is the Stanton number at the stagnation point and Re_∞ is the freestream Reynolds number based on the model diameter. Stanton number and Reynolds number are defined as:

$$St_s = \frac{q_s}{\rho_\infty u_\infty (h_0 - h_w)},$$

$$Re_{\infty} = \frac{\rho_{\infty} u_{\infty} D}{\mu_{\infty}}$$

A viscosity model for reacting gases developed by Blottner et al. is used to determine species viscosity. The viscosity of the gas mixture is then calculated using Wilke's semi-empirical mixing rule.

The measured stagnation point heat transfer rate was normalized to form the Stanton number, and a plot of this against the Reynolds number is shown in Fig.2. Also shown in Fig.2 are the theoretical predictions of Fay and Riddell's correlation of the equilibrium boundary layer for air, N_2 and CO_2 . The agreement of the present measurements with theoretical predictions of Fay and Riddell is good. In Fig.3(a) and Fig.3(b) the experimental data for air and CO_2 are compared with the numerical results and the existing data obtained by the ballistic range facility in NASA Ames (Yee et al. 1961). In Fig. 3(b), Sutton and Graves' (1971) correlation for CO_2 is also plotted. All the data follow the theoretical predictions though data show more scatter for the CO_2 case. It seems that the experimental data for CO_2 agree better with Fay and Riddell's equilibrium correlation than with Sutton and Graves' correlation.

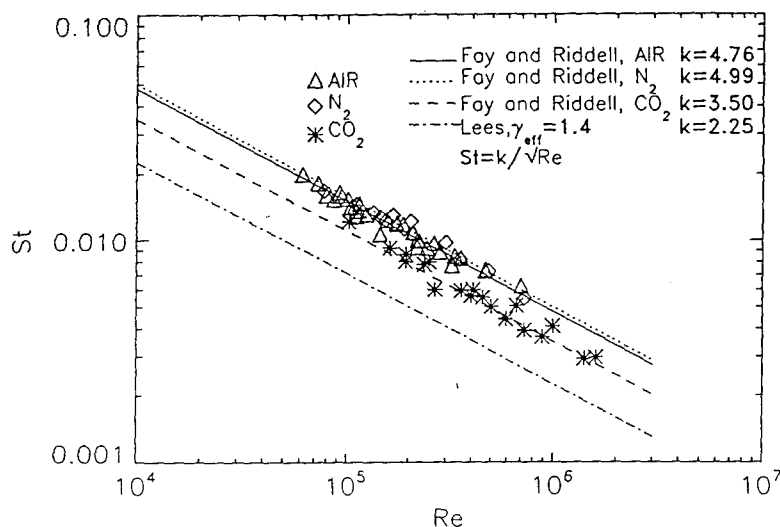


Fig. 2. Stagnation-point heat flux in dimensionless form, and comparison with Lees' theory, and Fay and Riddell's correlation

It is known that there are strong entropy gradients generated in the nose region of a blunt body in hypervelocity flows. The high-entropy layer essentially wets the body as it flows downstream. According to Crocco's theorem, the edge of the entropy layer is also a region of strong vorticity. Fig.4 shows computational vorticity contours of a typical CO_2 run. Strong vorticity gradients are observed. Fig.5(a) shows a resonantly-enhanced shadowgraph of the CO_2 flow with the same conditions of Fig.4. As may be seen, streamlines are marked by the sodium seeding and they are starting to roll up at the side of the sphere. Fig.5(b) shows these vortical structures on a larger scale. These vortical structures may be the by-product of the entropy layer. Further experiments are needed before definite conclusions may be reached.

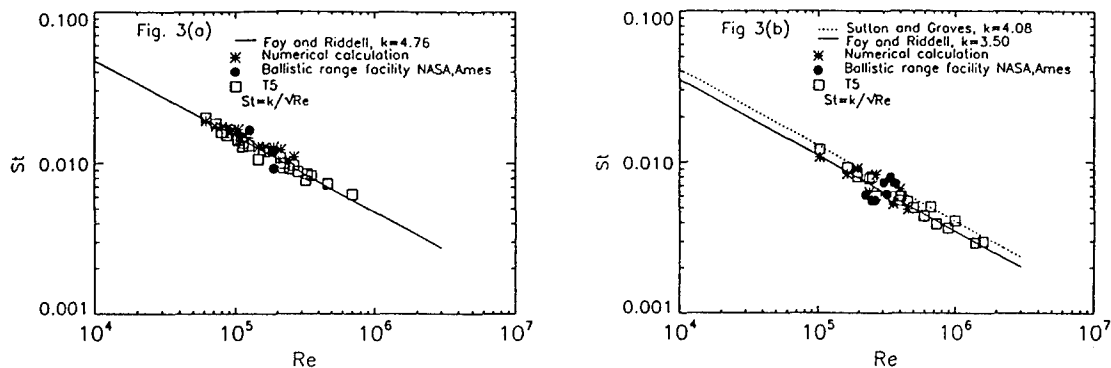


Fig. 3. Comparison of experimental stagnation-point heat flux of T5 and NASA Ames' ballistic range facility, numerical results and theoretical predictions for (a): air, and (b): CO_2

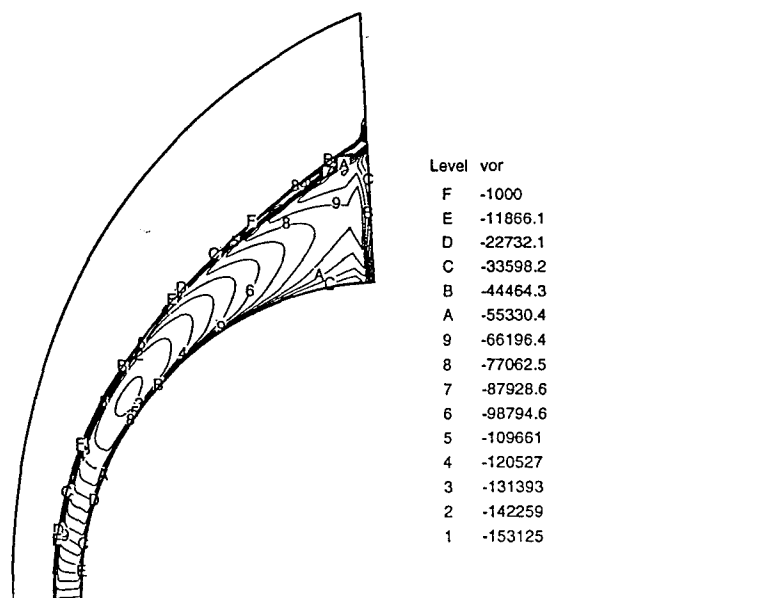


Fig. 4. Result of a computation of the vorticity field over a sphere of 4 in diameter. Freestream condition: CO_2 , 3.55 km/s, 0.081 kg/m³, 11.27 MJ/kg

5. Conclusions

- (1) Very good agreement was observed between the experimental differential interferographic fringe patterns and the numerical ones.
- (2) Good agreement was observed among the measured stagnation point heat transfer rates, numerical computation results and theoretical predictions. This provides another calibration of T5.
- (3) The resonantly-enhanced shadowgraphic technique may provide a promising tool for studying the vorticity-interaction problem in hypervelocity blunt-body flows.

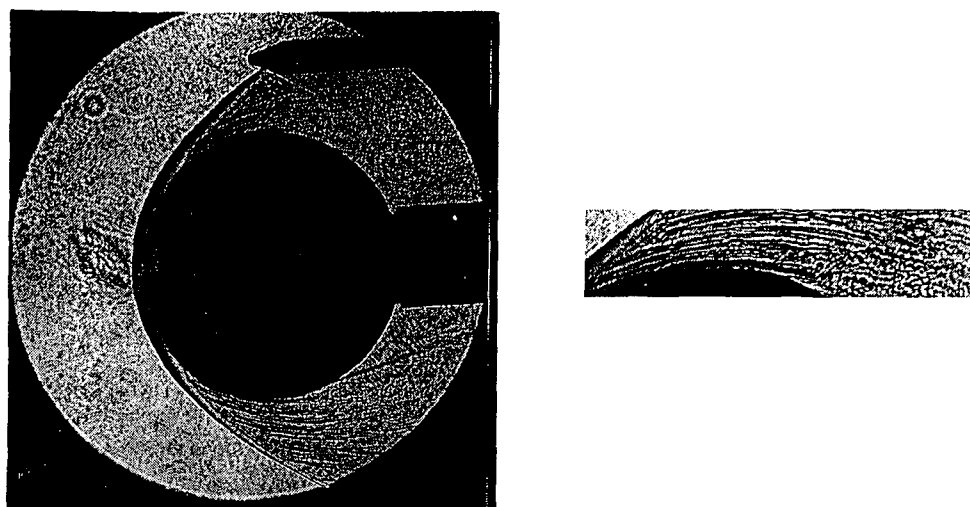


Fig. 5. Resonantly-enhanced shadowgraph of CO_2 flow over a sphere, at the same conditions as those of Fig. 4

Acknowledgement

This work was supported by AFOSR Grant F49610-92-J-0110 (Dr. L. Sakell) and AFOSR grant F49620-93-1-0338 (Dr. J. Tishkoff).

References

- Candler GV (1988) The computation of weakly ionized hypersonic flows in thermo-chemical nonequilibrium. Ph.D. Thesis, Stanford University
- Fay JA, Riddell FR (1958) Theory of stagnation point heat transfer in dissociated air. *Jour. Aero. Sci.* 25, 2, Feb.
- Germain P, Cummings E, Hornung HG (1993) Transition on a sharp cone at high enthalpy; new measurements in the shock tunnel T5 at GALCIT. AIAA Paper 93-0343, Reno
- Hornung HG (1992) Performance data of the new free-piston shock tunnel at GALCIT. AIAA Paper 92-3943, Nashville
- Hornung HG, Wen C, Candler, GV (1993) Hypervelocity flow over spheres. *Acta Mechanica*, to appear
- Lees L (1956) Laminar heat transfer over blunt bodies at hypersonic flight speeds. *Jet Propulsion* 26, 4, April
- Rein M (1989) SURF: A program for calculating inviscid supersonic reacting flows in nozzles. GALCIT Report FM 89-1
- Schultz DL, Jones, TV (1973) Heat transfer measurements in short duration facilities. AGARD Report 165
- Sutton K, Graves, AR (1971) A general stagnation-point convective-heating equation for arbitrary gas mixtures. NASA TR R-376 November
- Yee L, Bailey HE, Woodward HT (1961) Ballistic range measurements of stagnation-point heat transfer in air and in carbon dioxide at velocities up to 18,000 feet per second. NASA TN D-777 March

Hypervelocity flow simulation

Hans Hornung, Chihyung Wen, and Patrick Germain

Graduate Aeronautical Laboratories

California Institute of Technology, Pasadena CA 91125



part of "Mechanics USA 1994" edited by AS Kobayashi
Appl Mech Rev vol 47, no 6, part 2, June 1994

ASME Reprint No AMR146
© 1994 American Society of Mechanical Engineers

Hypervelocity flow simulation

Hans Hornung, Chihyung Wen, and Patrick Germain

Graduate Aeronautical Laboratories, California Institute of Technology, Pasadena CA 91125

Many of the flow problems associated with flight vehicles designed to reach or return from space can not be solved computationally. It is essential to address them by experiment, in particular, by ground simulation of the flow. The requirements and most successful simulation techniques are described, and their important limitations are discussed. Two selected examples are then presented from the free-piston reflected shock tunnel T5 at Caltech: Dissociating flow over spheres and transition from laminar to turbulent flow on a slender cone.

INTRODUCTION

The speed of a vehicle traversing the atmosphere of earth is necessarily of the order of the orbital speed. In the reference frame of the vehicle, the kinetic energy per unit mass of the flow at the most critical heating condition is approximately 18 MJ/kg. This is comparable to the dissociation energies of oxygen (15.5 MJ/kg) and nitrogen (33.6 MJ/kg), so that substantial chemical effects dominate the flow features. It is therefore essential that the flow speed U is reproduced in a simulation.

The chemical reactions proceed at finite rates. The dissociation reaction rates are proportional to the density, while recombination reactions are proportional to the square of the density. It follows that, for proper simulation of the dissociation reactions, it is necessary to reproduce the product of density ρ and model size L . This ensures that the ratio of the characteristic length associated with the reaction (the speed divided by the reaction rate) to the size of the model is the same in the simulation as in the prototype. This so-called binary scaling is thus characterized by precise reproduction of

$$U \text{ and } \rho L,$$

in the simulation. If binary scaling is used, by increasing the density to compensate for smaller scale, the recombination reactions will proceed to quickly. In many flows they play a much less important role than the dissociation reactions, so that binary scaling has a wide range of applicability.

To produce a flow of $U = 6$ km/s for example by a steady expansion from a reservoir at rest, the specific reservoir enthalpy of the gas has to be 18 MJ/kg. To achieve the necessary density in the flow for satisfactory binary scaling, the reservoir pressure has to be about 100 MPa. At these conditions, the reservoir temperature is about 9000 K, so that the heating load of the materials of the simulation facility are extreme, and the only way to avoid boiling them is to have the facility operate only for very short time. To give an appreciation of the problem, the heating rate at the above condition is 2 GW/m^2 , which

is about 50 times the energy flux at the surface of the sun. This is the reason why the shock tube is an essential component of the most successful facility types for this field.

A second reason for short time is the power requirement, which is typically 2 GW per square meter of cross-sectional area of the test section of a hypervelocity wind tunnel. Fortunately the test duration does not need to be long for good steady-flow testing, because of the high flow speed. A good value for the test time is given by $20L/U$, which, with a model length of 0.5 m and a flow speed of 6 km/s gives 1.7 ms. An excellent book on the subject of high-speed flow facilities is Lukasiewicz (1973).

SIMULATION METHODS and LIMITATIONS

The Reflected-Shock Tunnel

The most successful facility type for hypervelocity flow generation is the reflected shock tunnel. The gas is heated and compressed by passing a strong shock wave and its reflection from the end of a shock tube over it. With a shock speed of typically 4 km/s, this achieves the required reservoir conditions. A schematic sketch and wave diagram of the reflected shock tunnel is shown in Fig. 1.

At time zero, the diaphragm between the high-pressure (100 MPa) driver gas and the lower pressure (100 kPa) test gas is broken, and a shock wave travels to the right into the test gas, while an expansion wave travels to the left into the driver gas. The contact surface between the test and driver gases closely follows the shock, because the density ratio across the shock is typically 10. At the end of the tube, the shock reflects and produces a short slug of test gas at the required reservoir conditions. The shock also breaks a very thin diaphragm at a nozzle throat located in the end wall of the shock tube. The throat leads to the evacuated test section via an expansion nozzle.

In order to generate a shock wave of the required speed, it is necessary to heat the driver gas of the shock tube. This may be seen from Fig. 2, which shows the shock Mach num-

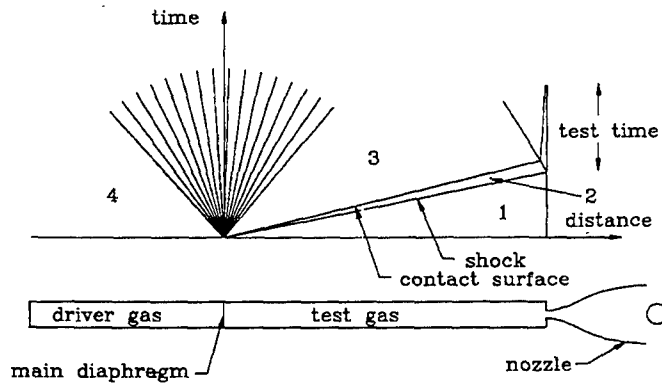


Fig. 1. Schematic sketch of reflected shock tunnel and wave diagram. The separation between the shock wave and contact surface is exaggerated to show it better

ber plotted against the pressure ratio, for different values of the driver/test gas ratio of sound speeds. Here the case of monatomic driver and diatomic test gas is shown. For realistic pressure ratios (< 2000) the diagram shows that the required shock Mach number of 12 (4 km/s) may only be reached if the sound speed ratio is around 10 or greater.

In order to achieve a sound speed of 3400 m/s in the driver gas, it has to be heated to about 3000 K even if helium is used as driver gas. This forces the driver-gas heating to be a transient process too. A particular version of driver-gas heating is the free-piston driver, in which the helium driver gas is compressed adiabatically with a heavy piston in a long compression tube. With a volumetric compression ratio of 50, the pressure is increased by a factor of 680 and the temperature is raised by a factor of 13.5, so that the required driver conditions may be reached from very benign initial conditions. The diaphragm rupture is passive in this set-up, i.e. it breaks when the pressure reaches the strength limit. An example of such a machine is shown in a scale drawing in Fig. 3. Large free-piston shock tunnels exist in Canberra, and Brisbane, Australia, Göttingen, Germany and Tullahoma, Tennessee, see Eitelberg (1992), Maus et al (1992), Bakos et al (1992), Stalker (1987).

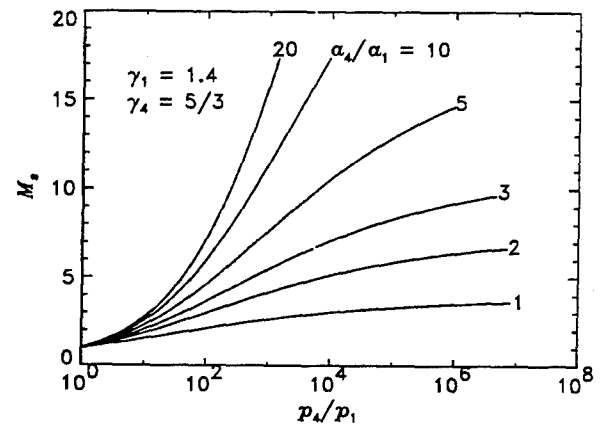


Fig. 2. The shock tube equation for monatomic driver gas and diatomic test gas, both treated as perfect gases. Note the strong dependence of the shock Mach number on the speed of sound ratio. Real-gas effects modify this diagram only slightly.

The Expansion Tube

An undesirable feature of the reflected-shock tunnel is that the test gas is stopped again by the reflected shock after it is accelerated by the primary shock. Since the aim is to produce a fast flow, i.e. to impart kinetic energy to the gas, stopping (and therefore heating) the gas before re-accelerating it in the nozzle expansion unnecessarily adds entropy to the gas. The undesirable effects this brings with it are a reduction in the reservoir pressure, and a partially dissociated state in the free stream.

The desire to avoid stopping the gas again after accelerating it with the primary shock led to the development of the expansion tube principle shown schematically in Fig. 4 together with the corresponding wave diagram. Up to the end of the shock tube, this is the same as the reflected shock tunnel. The shock tube is followed by an acceleration tube of the same diameter as the shock tube, and filled to a much lower pressure. These two tubes are initially separated by a very light di-

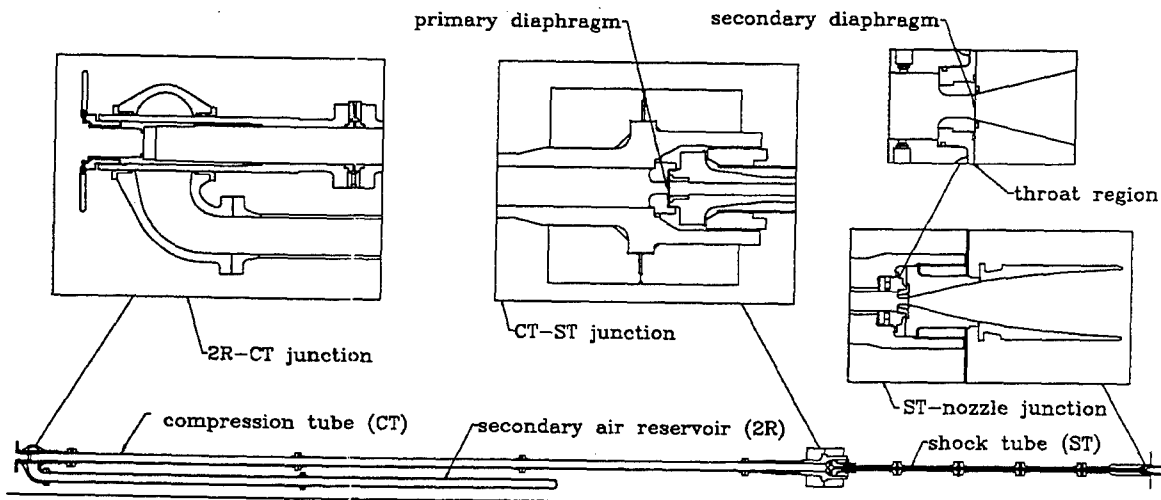


Fig. 3. Sectional view of the free-piston reflected shock tunnel T5 at GALCIT, with blow-ups of some of the parts. On the left is the 30 m long compression tube, joined to the 12 m shock tube and nozzle on the right. The test section and dump tank are not shown.

aphragm. The primary shock ruptures the light diaphragm, and accelerates to a faster speed in the lower density acceleration-tube gas. The test gas is then further accelerated by an unsteady expansion to the required conditions in region 30 of Fig. 4.

The expansion tube can produce flows with lower free-stream dissociation and higher effective reservoir pressure than the reflected-shock tunnel. However, it suffers from a very short test time, which is further reduced by the time taken to break the secondary diaphragm. The test section size is also necessarily limited to the shock tube diameter, while the reflected-shock tunnel can typically triple that. A large expansion tube is being operated by the General Applied Science Laboratory at New York.

A good way to compare the thermodynamic processes in these two facilities is to present them in a Mollier diagram, see Fig. 5. This clearly illustrates the high effective reservoir pressure that can be achieved in the expansion tube (without ever having to contain it). It also shows that the high temperature to which the throat is exposed in the reflected shock tunnel, is avoided. This is, in fact, the most severe limitation on pressure, size, and reservoir enthalpy of the reflected-shock tunnel, as may be seen from Fig. 6. It should be pointed out here that there is a severe penalty for scaling a reflected shock tunnel up to a larger size. This is brought out by the dashed curves in Fig. 6. No such scale penalty seems to exist in the case of the expansion tube.

The Princeton scheme, also shown in Fig. 5, is a proposed device, in which the test gas is expanded from extremely high

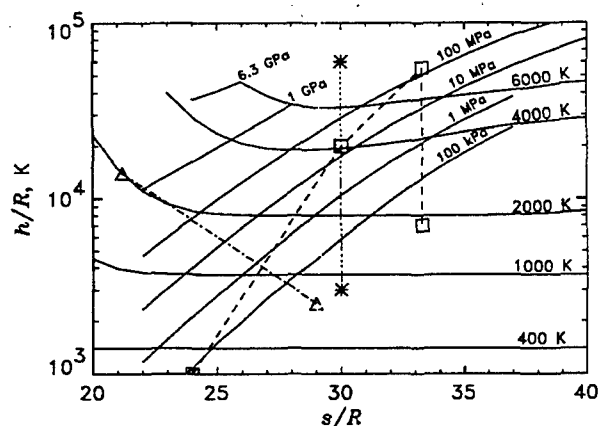


Fig. 5. Mollier diagram for equilibrium air, showing lines of constant pressure and temperature. An example of the processes in a reflected shock tunnel is shown by the dashed line. The lower asterisk represents the exit condition in an expansion tube that starts with the same shock tube conditions as in the reflected shock example. The upper asterisk represents the effective reservoir state of the expansion tube. The triangles show reservoir and exit condition of the facility proposed at Princeton.

pressure at the same time as it is being heated by light absorption. The idea is to avoid temperatures higher than 2000 K, thus preventing the formation of other species than O_2 and N_2 in the free stream. Significant questions regarding the achievabil-

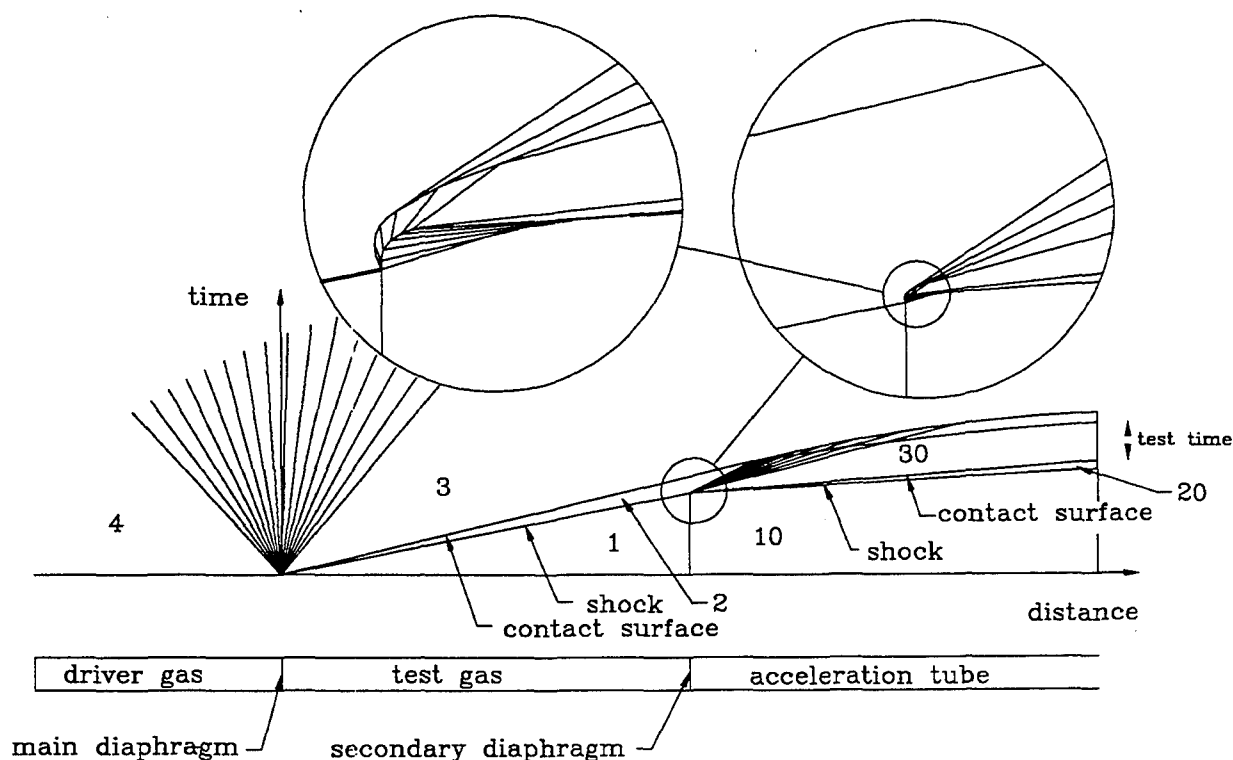


Fig. 4. Schematic sketch and wave diagram of an expansion tube. The detail in the vicinity of the rupture of the secondary diaphragm is shown in two enlarged insets. The diaphragm is accelerated to the contact surface speed over a finite opening time. This causes a reflected shock that is accelerated by the left running expansion wave transmitted from the diaphragm. Clearly, diaphragm opening time reduces the available test time.

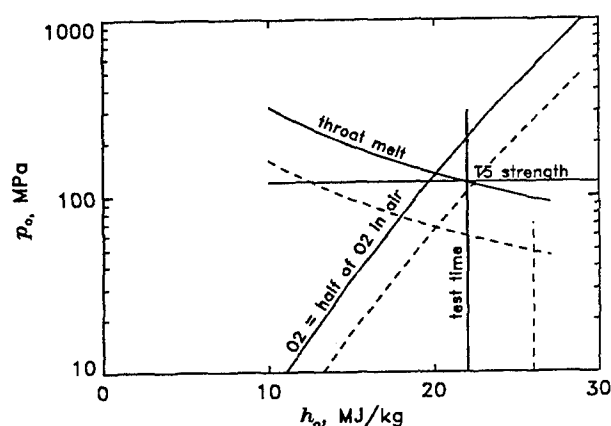


Fig. 6. Limitations on the reservoir pressure and specific enthalpy of reflected shock tunnels. The reservoir pressure is limited by the strength to lie below the horizontal line and by the throat melt limit below the curve. The free-stream dissociation (reduction of O_2) gets worse as the enthalpy is increased. The test time requirements limit the enthalpy to lie to the left of the vertical line. The full lines represent a facility of the size of T5. The dashed lines are for a facility scaled up by a factor of 4.

ity of this process are the high power requirement in the light source (order of 2 GW absorbed), and whether the absorption and redistribution of the energy can occur without producing atomic species and NO. Containment at 2000 K and 2 GPa is, of course, also not a trivial affair.

An indication of the quality of the flow in this free-piston reflected shock tunnel is given by the reservoir pressure records shown in Fig. 7.

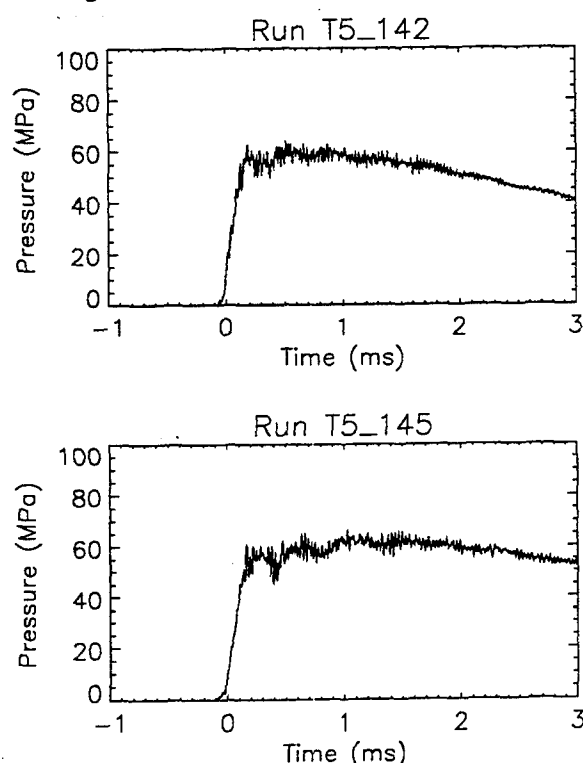


Fig. 7. Nozzle reservoir pressure traces of two runs in T5 at $h_0 = 22$ (TOP) and 11 MJ/kg (BOTTOM).

EXAMPLES of RECENT RESULTS from T5

As can be seen from the preceding section, the correct simulation of hypervelocity flows is fraught with problems. In the reflected shock tunnel, the reservoir pressure is not as high as one would like (constrained by nozzle throat melting) and the free stream contains some atomic species and nitric oxide at high enthalpy. The expansion tube remedies these two problems, but suffers from very short test time and small test section size.

The approach adopted in this field is therefore to study the most serious problems by abstracting the problem from the real situation into a simple form, so that the fundamental questions can be answered, and the general level of understanding can be raised. This involves both exploratory experiments and focussed investigations. An example of each of these is presented in the next two sections from the results obtained in the T5 Laboratory.

Hypervelocity Flow over Spheres

The most dramatic dissociative nonequilibrium effects occur in the front part of a blunt body, where the bow shock is nearly normal so that the temperature reaches very high values for which the equilibrium composition is highly dissociated. Because the dissociation is strongly endothermic, it reduces the temperature and therefore increases the density. This in turn causes the shock stand-off distance to decrease by as much as a factor of 2.

An approximate theoretical analysis of this problem indicated that the important parameters that determine the nonequilibrium behavior of the flow field are the reaction rate parameter immediately after the normal shock

$$\Omega = \frac{\rho_s}{\rho_\infty} \frac{d}{U^3} \left(\sum_{i=2}^n h_{c_i} \frac{dc_i}{dt} \right)_s$$

and ρ_e/ρ_s . Here, d is the diameter of the sphere, the c_i are the mass fractions of the n species, h_{c_i} are the partial derivatives of the enthalpy with respect to the mass fractions, t is time, and ρ_e and ρ_s are the densities that would be reached after an equilibrium shock and that reached after a shock before the dissociation takes place. The subscript s refers to values immediately after the shock. Thus, Ω may be interpreted as the ratio of the rate of energy absorption by the chemical reactions to the kinetic energy of the flow divided by the characteristic time scale of the flow, d/U .

This suggests that there exists a universal relationship of the form

$$\frac{\Delta}{d} \frac{\rho_s}{\rho_\infty} = f(\Omega, \rho_e/\rho_s),$$

which applies to all gases and free-stream conditions, provided that the Mach number is sufficiently high. The form of the function is also determined by the approximate analysis and is presented together with computational results for air in Fig. 8 and together with experimental results from T5 for carbon dioxide in Fig. 9.

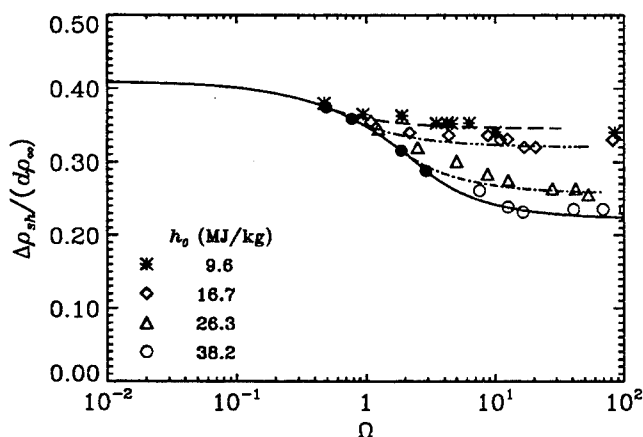


Fig. 8. Dimensionless stand-off distance plotted against reaction rate parameter for different specific reservoir enthalpies in air. The symbols represent computational results. The filled circle is the point at which the curve branches off from the solid line for each ρ_e/ρ_s .

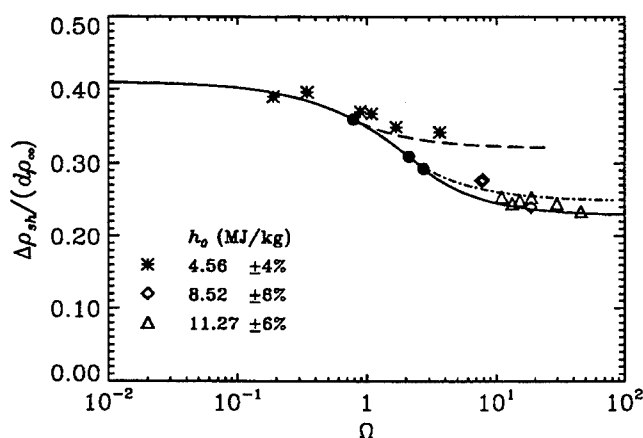


Fig. 9. Dimensionless stand-off distance plotted against reaction rate parameter for different specific reservoir enthalpies in carbon dioxide. The symbols represent experimental results.

As may be seen, the stand-off distance decreases monotonically from the frozen limit $\Omega \rightarrow 0$ to the equilibrium limit $\Omega \rightarrow \infty$. Up to a point, the curve is the same for all values of ρ_e/ρ_s . For different specific reservoir enthalpies, and therefore different ρ_e/ρ_s , the curve peels off from this limiting curve at different places, and approaches the appropriate equilibrium value for this enthalpy. The computational values are obtained using an inviscid form of a code by Candler (1988). As may be seen, the agreement with the approximate theory is excellent. The same applies to the comparison of the correlation with experimental results obtained in T5 with carbon dioxide. If the two figures had been superposed, the curves for equal ρ_e/ρ_s would be identical. The correlation is universal and applies for all gases. Similar results, both computational and experimental, have been obtained by Wen (1994).

The experimental values of the stand-off distance were obtained from differential interferograms of the flow, which give a wealth of additional information about the flow field. An examples of such interferograms is shown in Fig. 10. Comparisons of such interferograms with numerically generated equivalents give valuable insights into the applicability of the chemical model used in the computation, see Hornung et al (1994). The study also yielded a large body of information on heat transfer to the surface of the sphere, which, under the experimental conditions tested, reached values up to 60 MW/m^2 .

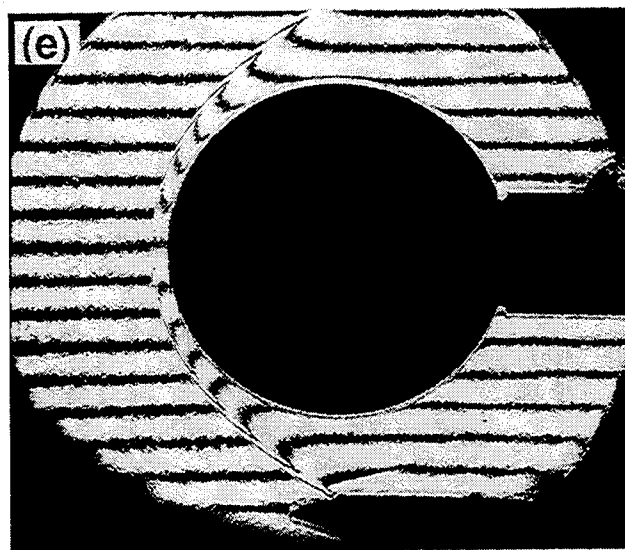


Fig. 10. Differential interferogram of CO_2 flow over a sphere of 4 in. diameter in T5. Flow speed 3.5 km/s, density 0.033 kg/m^3 .

Transition

The second example of results from the reflected shock tunnel is from an exploratory investigation to study the transition from laminar to turbulent flow in the boundary layer of a slender cone, Germain (1994). This topic is of critical importance to both the external flow over a vehicle and the performance of an air-breathing engine. Transition causes the heat transfer to the surface to increase by up to a factor of 4. Since the skin friction is much larger in turbulent than in laminar flow, the transition location is critical to the design of a vehicle and the uncertainty about it is often large enough to make or break a particular design.

Transition is an instability phenomenon. For it to occur, the weak disturbances that are always present in the oncoming flow must be amplified by the behavior of the boundary layer. It therefore depends very much on the spectrum of disturbances present in the free stream. On the face of it, such an investigation in a shock tunnel seems to be bold, not to say foolhardy, since it is very difficult to ascertain the disturbance spectrum in such a facility. However, the high speed provides a saving grace inasmuch as the characteristic frequency of the dominant instability at the conditions in T5 for example, is of the order of 1 MHz, which is well above any possible mechanical noise in the machine. The Tollmien-Schlichting instability mode is, however, in the range ($\approx 150 \text{ kHz}$) where the flow may be expected to be noisy. Consequently it is likely to be possible to single out this mechanism.

One of the most important phenomena discovered in the exploratory study was the dependence of the transition Reynolds number on dissociative real-gas effects. To detect transition, the slender cone was equipped with heat transfer gauges. The dimensionless distance from the tip of the cone formed with the viscous length scale $\mu/(\rho U)$, where μ is the viscosity, ρ is the density, and U is the velocity of the gas is called the transition Reynolds number. It is customary to evaluate the material properties at the maximum temperature that occurs in the boundary layer, in order to eliminate the influence of the Mach number and wall-to-free-stream temperature ratio from comparisons. This was done to form the parameter Re_{tr}^* plotted as the ordinate of Fig. 11 against the specific reservoir enthalpy:

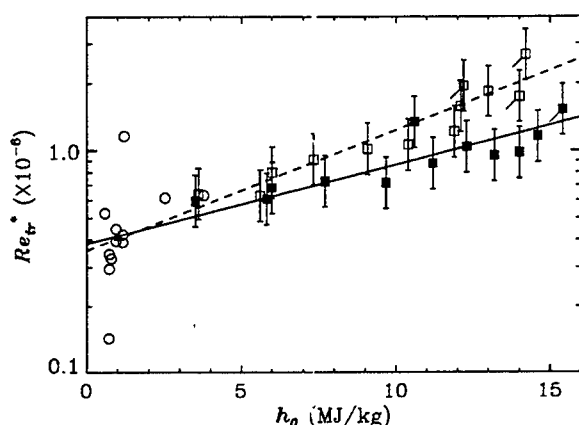


Fig. 11. Transition Reynolds number evaluated at the reference temperature in the boundary layer, plotted against specific reservoir enthalpy. Open squares are experimental results for air, filled squares for nitrogen. Open circles are results from other sources. Flagged symbols indicate cases in which transition was not reached.

A number of interesting features are evident from this plot. First, the results from T5 agree approximately with those from other facilities at low enthalpy. The scatter in these is large, because they come from a number of different facilities. Also, the highest enthalpy of previous results is near the lowest enthalpy tested in T5, so that the enthalpy range of the data has

been very much increased. Second, the plot exhibits a significant increase of the transition Reynolds number with enthalpy. Third, the enthalpy dependence is significantly stronger in the case of air than in nitrogen. This suggests that the enthalpy dependence is not an artifact of the facility (e.g. enthalpy dependence of the noise spectrum) but is related to the enthalpy at which real-gas effects appear in a particular gas. As the dissociation energy of nitrogen is approximately twice that of oxygen (see Introduction), the trend goes in the right relative direction.

CONCLUSION

The most successful methods of hypervelocity flow simulation were presented together with the associated difficulties and limitations. Two examples of results from fundamental research projects carried out in one such facility were given, which show that such facilities can be used successfully for the discovery of new phenomena as well as for focussed investigation for the better understanding and clarification of issues where the phenomena are broadly known.

ACKNOWLEDGEMENTS

This work was supported by AFOSR Grant F49610-92-J-0110 (Dr. L. Sakell) and AFOSR grant F49620-93-1-0338 (Dr. J. Tishkoff).

REFERENCES

- Bakos RJ, Tamagno J, Riszskalla O, Pulsonetti MV, W. Chinitz, and Erdos JI (1992), Hypersonic mixing and combustion studies in the HYPULSE facility, *J Propulsion and Power* 8 900-906.
- Candler GV (1988), The computation of weakly ionized hypersonic flows in thermo-chemical nonequilibrium, PhD Thesis, Stanford University.
- Eitelberg G (1992), The high-enthalpy shock tunnel in Göttingen", AIAA Paper No. 92-3942, Nashville.
- Germain P (1993), The boundary layer on a sharp cone in high-enthalpy flow, PhD Thesis, California Institute of Technology.
- Hornung HG (1992), Performance data of the new free-piston shock tunnel at GALCIT, AIAA Paper No. 92-3943.
- Hornung HG, Wen C, and Candler GV (1994), Hypervelocity flow over spheres, *Acta Mechanica* [Suppl] 4 163-170.
- Lukasiewicz J (1973), *Experimental methods of hypersonics*, Marcel Dekker, Inc. New York.
- Maus, JR, Laster M, and Hornung H (1992), The G-Range impulse facility—a high performance free piston shock tunnel, AIAA Paper No. 92-3946, Nashville.
- Wen C (1994), Hypervelocity flow over spheres, PhD Thesis, California Institute of Technology.

Analysis of Thermochemical Nonequilibrium Models for Carbon Dioxide Flows

Stacey G. Rock*

Center for Space Transportation and Applied Research, Tullahoma, Tennessee 37388

Graham V. Candler†

University of Minnesota, Minneapolis, Minnesota 55455

and

Hans G. Hornung‡

California Institute of Technology, Pasadena, California 91125

The aerothermodynamics of thermochemical nonequilibrium carbon dioxide flows are studied. The chemical kinetics models of McKenzie and Park are implemented in a three-dimensional computational fluid dynamics code. The code incorporates a five-species gas model characterized by translational-rotational and vibrational temperatures. Solutions are obtained for flow over finite-length elliptical and circular cylinders for a freestream condition of $u_\infty = 4.24$ km/s, $T_\infty = 1970$ K, and $h_{0\infty} = 9.0$ MJ/kg. The computed flowfields are then employed to calculate Mach-Zehnder interferograms for comparison with experimental data. The accuracy of the chemical kinetics models is determined through this comparison. Also, the methodology of the three-dimensional thermochemical nonequilibrium code is verified by the reproduction of the experiments.

Introduction

THE accurate modeling of reacting carbon dioxide flows is of importance in Martian atmospheric entry, where the atmosphere is composed primarily of CO₂. Hypersonic flows over vehicles with carbon-based ablators is another area where the chemical kinetics of carbon dioxide become important. The type of chemical kinetics model used directly affects the aerodynamic and heating characteristics of these vehicles. For this and other reasons, there is interest in determining which of the current chemical kinetics models is most accurate.

The two primary chemical kinetics models in use are the ones developed by McKenzie¹ and by Park et al.⁴ The first model was developed by McKenzie¹ in the mid 1960s, and was extended in the work of Evans et al.² and Grose et al.³ who studied the effects of nonequilibrium chemistry on the Viking and Pioneer planetary entry probes. The second model was developed more recently by Park et al.⁴ These models have been implemented in computational fluid dynamics codes to study Martian atmospheric entry. Candler⁵ demonstrated that certain aspects of the flow solutions produced by the McKenzie model, primarily shock stand-off distance, compared well to experiment. Chen et al.⁶ have used both the McKenzie and Park models to predict surface heating rates over Martian entry vehicles. Their findings indicate a significant difference between the heating rates predicted by the two models. However, the shock stand-off distance and shock shape predicted by the two models were similar. Therefore, a more detailed analysis is required to determine which of the models is more accurate, and whether the more accurate model can be further improved.

The detailed analysis of both chemical kinetics models is the purpose of this study. The reaction rate model and vibra-

tional relaxation rate model are tested by comparison to experimental data obtained by Hornung. The data consist of a series of interferograms of dissociating CO₂ flows about circular and elliptical cylinders. The tests were conducted in 1971 in a large free piston shock tunnel, known as T3, located at the Australian National University. The series of Mach-Zehnder interferograms form a very valuable and reliable data base for validating current aerothermodynamic models for reacting CO₂ flows. Also, as compared to air or nitrogen, CO₂ is a gas in which the vibrational component of the energy is an order of magnitude more important in relation to the amount of energy absorbed by the dissociative reactions in the flow. Experiments in CO₂ are therefore a much more sensitive instrument for testing different chemistry and vibration models through experimental comparison to computational fluid dynamics (CFD). By computationally reproducing the interference patterns, the accuracy of current models can be investigated.

Thermophysical Model

The thermophysical model for a reacting CO₂ flow must allow for the presence of chemical and thermal nonequilibrium. Chemical nonequilibrium is accounted for by modeling the dissociating CO₂ flow as a mixture of chemically reacting species. For flows not involving ionization, such as those considered here, there are five primary chemical species, CO₂, CO, O₂, C, and O. The interaction of these species is governed by the chemical kinetics models of McKenzie or Park et al. The adaptation of these models into a CFD code capable of simulating chemical nonequilibrium flows is discussed in this section.

Vibrational Energy Model

Thermal nonequilibrium is accounted for by allowing the translational-rotational and vibrational energies to evolve at different rates. With the current model, the translational and rotational energy modes are assumed to be in equilibrium with each other at the translational-rotational temperature T . It is assumed that a separate vibrational temperature T_v characterizes the vibrational energy of all of the vibrational energy modes of the gas. This assumption requires that the vibrational modes are strongly coupled with one another so that they relax at the same rate. Camac⁷ demonstrates that the three vibrational modes of CO₂ relax at the same rate. This

Presented as Paper 92-2852 at the AIAA 27th Thermophysics Conference, Nashville, TN, July 6-8, 1992; received Oct. 15, 1992; revision received May 17, 1993; accepted for publication May 19, 1993. Copyright © 1993 by the American Institute of Aeronautics and Astronautics, Inc. All rights reserved.

*Research Engineer. Member AIAA.

†Assistant Professor, Department of Aerospace Engineering and Mechanics. Member AIAA.

‡Director, Graduate Aeronautical Laboratories and Clarence L. Johnson Professor of Aeronautics. Member AIAA.

equilibration is due to strong resonance coupling between the different vibrational modes of CO₂.

The total vibrational energy of the CO₂ mixture is the sum of the individual vibrational energies of the molecular species. A simple harmonic oscillator is employed to describe the vibrational potential of each vibrational mode of the molecules. Carbon dioxide has three vibrational modes, one of which is doubly degenerate. With the assumption that there is a unique vibrational temperature at each point in the flowfield, the vibrational energy per unit mass of CO₂ is given by

$$e_{vCO_2} = e_{vCO_2,1} + e_{vCO_2,2} + e_{vCO_2,3} \quad (1)$$

where

$$e_{vCO_2,r} = g_r \frac{R}{M_{CO_2}} \frac{\theta_{vCO_2,r}}{e^{\theta_{vCO_2,r}/T_v} - 1} \quad (2)$$

where $\theta_{vCO_2,r}$ is the characteristic temperature of vibrational mode r , g_r is the degeneracy of that mode, R is the universal gas constant, and M_{CO_2} the atomic weight. The vibrational energy per unit mass of a diatomic species (CO, O₂) is given by

$$e_{vs} = \frac{R}{M_s} \frac{\theta_{vs}}{e^{\theta_{vs}/T_v} - 1} \quad (3)$$

where s represents either diatomic species. See Table 1 for the values of θ_{vs} and g_r .

The rate at which these vibrational energies relax toward the translational energy is assumed to behave according to the Landau-Teller relaxation expression⁸

$$Q_{vs} = \rho_s \frac{e_{vs}^*(T) - e_{vs}}{\tau_s} \quad (4)$$

where Q_{vs} is the rate of energy transfer to species s per unit volume, the term τ_s is the vibrational relaxation time, and $e_{vs}^*(T)$ is the vibrational energy evaluated at the local translational temperature T .

The relaxation time of species s due to collisions with species r , τ_{sr} is determined from an expression due to Millikan and White⁹

$$\ln \tau_{sr} p = 0.00116 \mu_{sr}^{1/2} \theta_{vs}^{4/3} (T^{-1/3} - \mu_{sr}^{1/4}) - 18.42 \quad (5)$$

where μ_{sr} is the reduced mass, p is the pressure in atmospheres, and τ_{sr} is in seconds. The relaxation time of species s is then the number-weighted average of τ_{sr}

$$\tau_s = \frac{\sum_r N_r}{\sum_r N_r / \tau_{sr}} \quad (6)$$

where N_r is the number density of species r . The Millikan-White formulation is in good agreement with experimental data for the diatomic species.^{9,10} The Millikan-White expression for CO₂ predicts that the three vibrational modes of CO₂ will relax at different rates. The results of Camac⁷ indicate that the three modes relax at the same rate, and the vibrational relaxation time of CO₂ can be modeled by

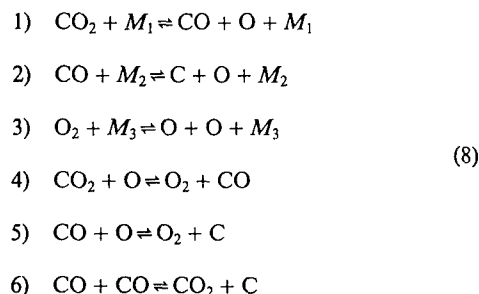
$$\ln \tau_{CO_2} p = 36.5 T^{-1/3} - 17.71 \quad (7)$$

where τ_{CO_2} is in seconds and p is in atmospheres. This relaxation time is similar to the one predicted by Millikan and White for the $\theta_v = 945$ K bending mode.⁵ Therefore, the Millikan-White expression is in good agreement with the Camac expression if all of the modes are assumed to relax according to the $\theta_v = 945$ K bending mode. The expression developed by Camac is a fit to experimental data for $2000 < T < 6000$ K. This is the same temperature range being investigated in this study. Because of the temperature being relatively low and coinciding with the Camac data, the collision-limited value of

the vibrational relaxation time τ_c proposed by Park¹¹ is not required. Both the Camac expression and the Millikan-White expression, modified using $\theta_v = 945$ K for all modes, are investigated in this study.

Chemical Kinetics Model

The chemical reactions considered for this flow are



where M represents any species that acts as a collision partner for the reaction. The six available reactions are governed by forward and backward reaction rate coefficients k_f and k_b , which have the Arrhenius form

$$\begin{aligned} k_f &= C_f T^{\eta_f} \exp(-\theta_f/T) \\ k_b &= C_b T^{\eta_b} \exp(-\theta_b/T) \end{aligned} \quad (9)$$

Table 1 Vibrational energy constants

Species	θ_v , K	g
CO ₂	1903	1
	945	2
	3329	1
CO	3074	—
O ₂	2239	—

Table 2 McKenzie reaction rate coefficients, m³/kmol · s or m⁶/kmol² · s

Reaction no.	C_f	η_f	θ_d	C_b	η_b	θ_b
1	1.20×10^8	0.5	34,340	2.00×10^0	1.25	-28,400
2	4.48×10^{16}	-1.0	128,900	1.00×10^{12}	-1.0	0
3	9.05×10^{15}	-1.0	59,370	9.00×10^9	-0.5	0
4	2.54×10^8	0.5	27,690	5.00×10^5	1.0	23,900
5	2.73×10^9	0.5	69,540	9.40×10^9	0.25	0
6	2.33×10^6	0.5	65,710	4.60×10^9	-0.25	0

Table 3a Park et al. reaction rate coefficients, m³/kmol · s or m⁶/kmol² · s

Reaction no.	C_f	η_f	θ_d	C_b	η_b	θ_b
1	3.70×10^{11}	0.0	52,500	6.10×10^3	0.75	-10,240
2	2.30×10^{16}	-1.0	129,000	5.13×10^{11}	-1.0	0
3	2.00×10^{18}	-1.5	59,500	2.00×10^{12}	-1.0	0
4	1.70×10^{10}	0.0	26,500	3.33×10^7	0.5	22,500
5	3.90×10^{10}	-0.18	69,200	1.34×10^{11}	-0.43	0
6	2.33×10^6	0.5	65,710	4.60×10^9	-0.25	0

Table 3b Park multipliers for third body reactions

Species	M_1	M_2	M_3
CO ₂	1	1	1
CO	1	1.95	1
O ₂	1	1	1
C	1	14.8	5
O	1	14.8	5

where C_f , C_b , η_f , η_b , θ_f , and θ_b are constants. The values of these constants are supplied by either the McKenzie or the Park chemical kinetics model (see Tables 2 and 3). In addition to differences in reaction rate coefficients, the Park model also differs from the McKenzie model by the addition of a multiplier term, the purpose of which is to account for the efficiency of third body collisions. The appropriate reaction rate coefficient is multiplied by this factor.

A comparison of McKenzie and Park forward reaction rate coefficients for the dissociation of CO_2 is presented in Fig. 1. For $T < 5000$ K, McKenzie predicts a faster reaction rate than Park. The discrepancy is as much as an order of magnitude for $T < 2500$ K. However, for $T > 5000$ K, Park predicts reaction rates faster than those of McKenzie. Figure 2 shows the comparison for the dissociation of CO. The two models predict similar rates and trends for the entire temperature range, with the Park rates only slightly lower. The forward reaction rate coefficients for the dissociation of O_2 are shown in Fig. 3. Once again the two models predict similar rates and trends. However, for this reaction Park predicts higher rates. For this study the driving reaction is the dissociation of CO_2 . In addition, the majority of the flow is in the 5000–7000 K range. For this reason, Park predicts an overall faster reaction rate for the cases being studied.

Solution Procedure

The flowfield can be described as the solution of the Euler equations expanded to account for multiple reacting species and nonequilibrium vibrational energy. This set of coupled

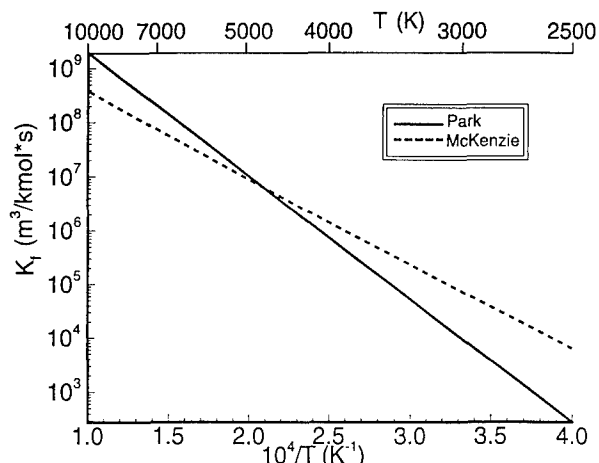


Fig. 1 Comparison of the forward reaction rates of McKenzie¹ and Park⁴ for the dissociation of CO_2 .

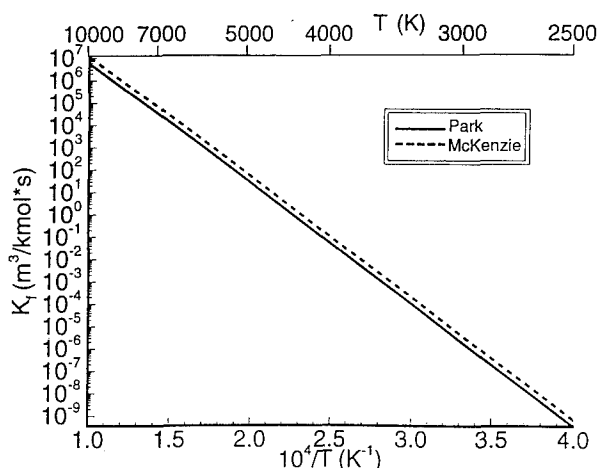


Fig. 2 Comparison of the forward reaction rates of McKenzie¹ and Park⁴ for the dissociation of CO.

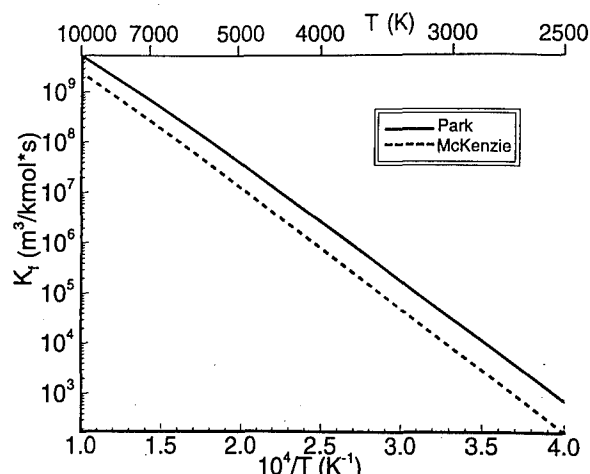


Fig. 3 Comparison of the forward reaction rates of McKenzie¹ and Park⁴ for the dissociation of O_2 .

partial differential equations is approximated in three dimensions using a finite volume, flux-vector splitting method developed by Candler¹² and Candler and McCormack.¹³ The approximate equations are solved using a lower-upper symmetric Gauss Seidel method^{14–16} that has been modified to allow for the efficient treatment of thermochemical nonequilibrium flows.¹⁷ The solution provides values of the thermodynamic variables throughout the flow. The converged solution is then used in conjunction with the multidimensional self adaptive grid (SAGE) code¹⁸ to produce a flow adapted grid. The adapted grid is then used to produce a highly resolved flow solution for use in the computation of interferograms.

Computation of Interferograms

A Mach-Zehnder interferometer is an optical device that makes possible the visualization of density fields in a flow. The interferometer is sensitive to variations in the optical path length of a light beam passing through the flow. The optical path length is a function of the density and index of refraction of a species present. When this light beam is recombined with a reference beam that passes outside of the test section, the two constructively and destructively combine to form an interference pattern. This pattern is manifest through a series of dark and light fringes.

The form of the relation describing the interference patterns has been developed in several references.^{19–21} For a gas composed of multiple species the expression for the optical fringe shift relative to the freestream is given by

$$F = \int_{z_1}^{z_2} \left(\Delta \rho \sum_{i=1}^n \frac{K_i \rho_i}{\lambda \rho} \right) dz \quad (10)$$

where z is the optical path length, λ is the wavelength of the light source, ρ_i/ρ is the mass fraction of species i , K_i is the Gladstone-Dale constant of species i , n is the number of species, and $\Delta \rho$ is the density change relative to the freestream. The limits of integration, z_1 and z_2 , represent the length along the optical path length where the index of refraction is varying. In three dimensions this length is dependent on the region of the flow that the light beam passes through. The quantity actually recorded on the interferogram is the intensity of the interference of the recombined beams. The intensity I is proportional to F by

$$I \sim \cos^2(\pi F) \quad (11)$$

The values of the Gladstone-Dale constant are listed in Table 4.

The integration of Eq. (10) is performed along the optical path length of the light source passing through the flow. This

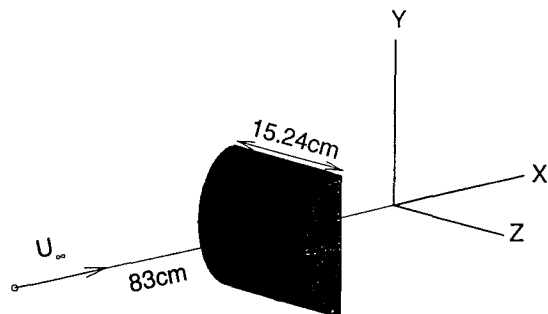


Fig. 4 Schematic of experimental model used in T3 free-piston shock tunnel.

path direction coincides with the z direction of the body-centered Cartesian coordinate system in Fig. 4. Since the flow solution is obtained on a curvilinear coordinate system, a line-of-sight calculation must be performed to evaluate the integral. This calculation is achieved by transforming the physical space into a computational space $(x, y, z) \rightarrow (\xi, \eta, \zeta)$. The ξ , η , and ζ directions correspond to the streamwise, body normal, and spanwise directions, respectively. The line-of-sight calculation can then be performed in the computational space in an efficient manner. The equation that governs this calculation is a function of the integration step dz and the mesh metrics $x_\xi, x_\eta, y_\xi, y_\eta, z_\xi, z_\eta$. The equation is not a function of the ζ metrics because the calculation is performed in the ξ, η plane. The line-of-sight calculation requires that x and y remain constant ($dx = 0$ and $dy = 0$), whereas z (dz) is allowed to vary. Actually, the problem is overspecified. The lengths x and y form the legs of a right triangle with a hypotenuse of fixed length. Therefore, $dx = 0$ implies $dy = 0$ and vice versa and so $dx = 0$ or $dy = 0$ is sufficient. These two conditions lead to the following set of equations that govern the integral calculation:

$$d\xi = \frac{+x_\eta}{J} dz \quad \text{and} \quad d\eta = \frac{-x_\xi}{J} dz \quad (12a)$$

or

$$d\xi = \frac{+y_\eta}{J} dz \quad \text{and} \quad d\eta = \frac{-y_\xi}{J} dz \quad (12b)$$

where $J = z_\xi x_\eta - z_\eta x_\xi$ or $J = z_\xi y_\eta - z_\eta y_\xi$, respectively. A numerical approximation to the integral is performed by setting dz equal to a finite length Δz and marching along the optical path length in physical space for a fixed number of points in the xy plane. Equation (12) provides the corresponding $\Delta\xi$ and $\Delta\eta$ for the marching step in the computational space. The value of the fringe shift for each line of sight in the xy plane is then given by

$$F = \sum_{z_1}^{z_2} \left(\overline{\Delta\rho} \sum_{i=1}^n \frac{K_i \bar{\rho}_i}{\lambda \rho} \right) \Delta z \quad (13)$$

The quantities in Eq. (13) are the same as those in Eq. (10) except that the overbar indicates that the variables have been averaged over the integration step.

Equation (13) shows the dependence of the fringe pattern on density and mass fractions. At each point in the flow, these values are dependent on the chemical kinetics and vibrational energy models. Therefore, changes in the CO_2 thermophysical model are observed in the interferograms and may be directly compared to experimental data.

Experimental Data

A series of circular and elliptical cylinders of varying radii and eccentricities was tested. The geometries of these cases are listed in Table 5. All of the cylinders have a length of 15.24 cm

Table 4 Gladstone-Dale constants for use in Eq. (10) with values from Refs. 20-22

Species	$K, 10^3 \text{ m}^3/\text{kg}$
CO_2	0.230
CO	0.270
O_2	0.190
C	0.404
O	0.182

Table 5 Semimajor and semiminor axes for elliptical geometries and wavelength of interferogram for dissociating CO_2

Case	$a : b$	a, cm	b, cm	λ, nm
1	3:2	6.35	4.23	533
2	3:1	2.54	0.846	533
3	1:1	2.54	2.54	433
4	1:1	5.08	5.08	433
5	2:1	3.81	1.91	533

and are located in a conical flow with a point source 83.0 cm upstream of the leading edge of the model. A schematic of the experiment is shown in Fig. 4. The nominal freestream conditions are $u_\infty = 4.24 \text{ km/s}$, $\rho_\infty = 7.27 \times 10^{-3} \text{ kg/m}^3$, and $T_\infty = 1970 \text{ K}$, with mass fractions of $c_{\text{CO}_2} = 0.268$, $c_{\text{CO}} = 0.445$, $c_{\text{O}_2} = 0.155$, $c_{\text{O}} = 0.133$, and a trace of gaseous carbon. These freestream mass fractions were computed assuming freezing near the nozzle throat. There is some uncertainty in these values, but errors of 10% were found not to affect the results.

These freestream conditions lead to a Mach number on the order of 5. This Mach number is lower than Mach numbers of typical entry conditions. However, an analysis of steady-state, dissociation-dominated flows reveals that the similarity parameters are

$$\left(\frac{r\rho_\infty}{u_\infty} \right)_{\text{exp}} = \left(\frac{r\rho_\infty}{u_\infty} \right)_{\text{flight}} \quad (14)$$

$$(h_{0\infty})_{\text{exp}} = (h_{0\infty})_{\text{flight}}$$

where r is a characteristic length, which was taken to be the nose radius. The terms ρ_∞ , u_∞ , and $h_{0\infty}$ are the freestream density, velocity, and total enthalpy, respectively. This result comes from the binary scaling that governs dissociating flows.²³

The similarity parameters for the experiment performed by Hornung are calculated to be $(r\rho_\infty/u_\infty)_{\text{exp}} = 3.71 \times 10^{-8} \text{ kg s/m}^3$ and $(h_{0\infty})_{\text{exp}} = 9.06 \text{ MJ/kg}$. A comparison to the flight conditions being studied for the Martian environmental survey⁶ (MESUR) aeroshell, $(r\rho_\infty/u_\infty)_{\text{MESUR}} = 4.36 \times 10^{-8} \text{ kg s/m}^3$ and $(h_{0\infty})_{\text{MESUR}} = 10.4 \text{ MJ/kg}$, demonstrate that the experimental data are similar to the flight regimes to be encountered by this entry vehicle in the Martian atmosphere.

Results

Computational interferograms have been produced for five experimental cases using both the Park et al. and the McKenzie chemical kinetics models. The initial solutions were performed on $30 \times 50 \times 30$ computational grids. Figures 5 and 6 show the experimental comparison for case 1. The two models produce similar solutions, and it is only through a detailed comparison to the interferogram fringe patterns that the accuracy of each model can be assessed. The Park chemical kinetics model produces an interferogram in excellent agreement with the experiment, whereas the McKenzie model produces a less accurate result. The Park model slightly underpredicts the shock stand-off distance, but the computational stand-off distance would be increased slightly with the inclusion of the

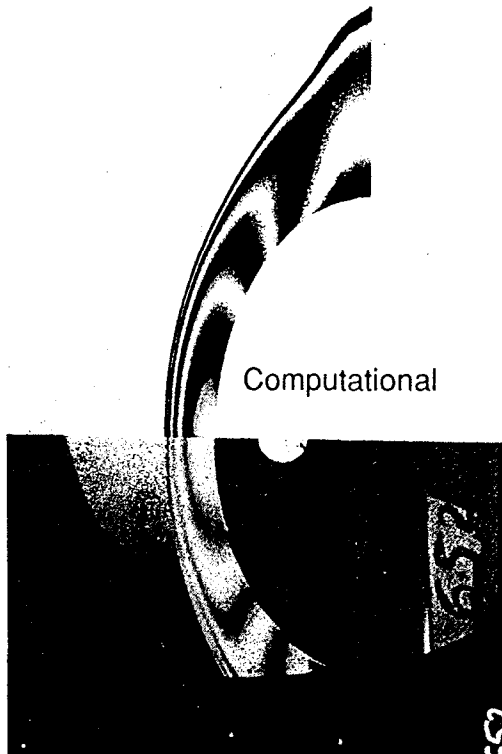


Fig. 5 Comparison of case 1 experimental and computational interferograms for the McKenzie¹ rate model on $30 \times 50 \times 30$ grid.

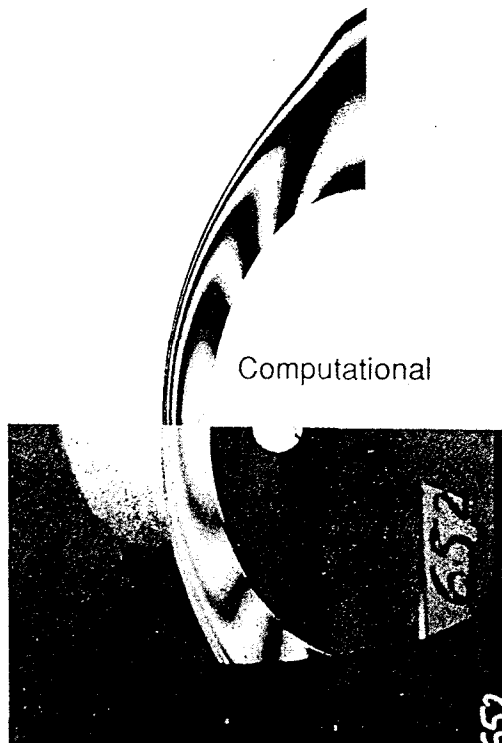


Fig. 6 Comparison of case 1 experimental and computational interferograms for the Park et al.⁴ rate model on $30 \times 50 \times 30$ grid.

boundary layer. The McKenzie model overpredicts the stand-off distance; the comparison would be made worse if the viscous effects were included in the computation. A careful overlaying of the fringe patterns indicates that the Park model produces better agreement of the fringe locations and shapes. For example, the full fringe closest to the stagnation point is too thick in the McKenzie model simulation, whereas the

thickness is very close in the Park model computation. Overall, the Park model produces excellent agreement with the details of the fringe patterns, except for the boundary layer that appears in the experimental interferogram. The overprediction of the shock-layer thickness in the McKenzie model simulations is due to an underprediction of density rise. This

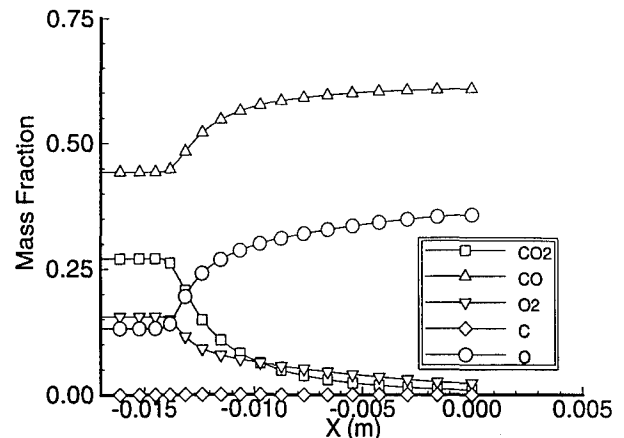


Fig. 7 Mass fractions along stagnation streamline for the McKenzie¹ rate model on $30 \times 50 \times 30$ grid.

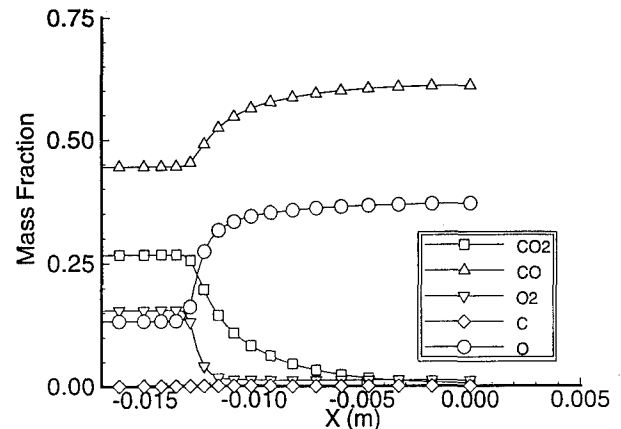


Fig. 8 Mass fractions along stagnation streamline for the Park et al.⁴ rate model on $30 \times 50 \times 30$ grid.

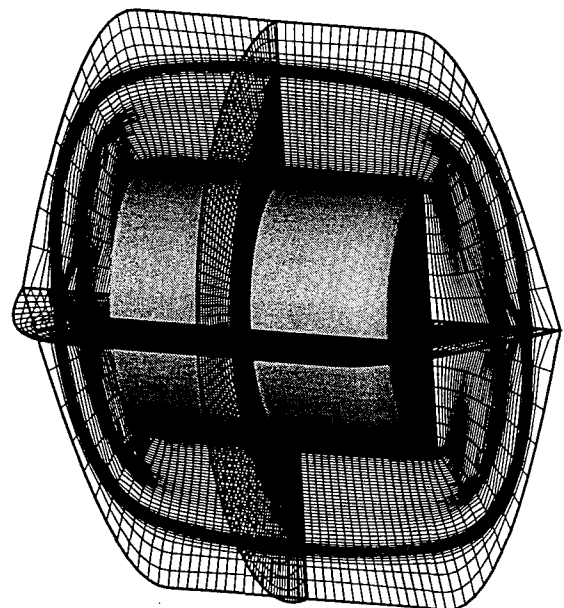


Fig. 9 $50 \times 50 \times 30$ adapted grid for case 1.

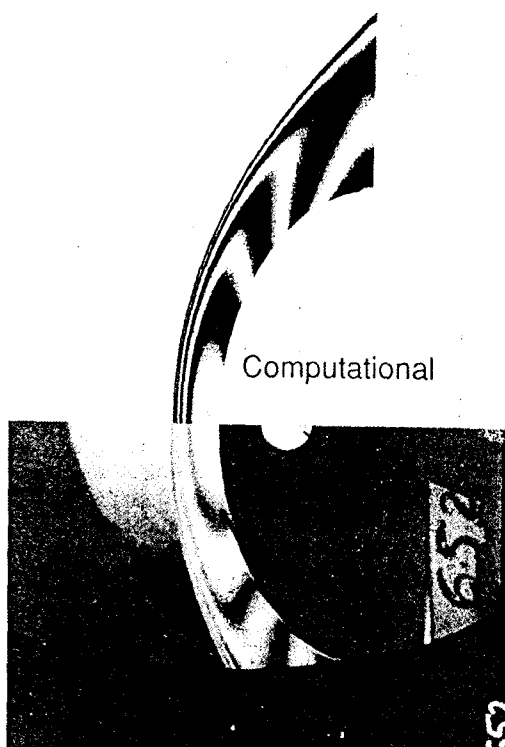


Fig. 10 Comparison of case 1 experimental and computational interferograms for the Park et al.⁴ rate model on $50 \times 50 \times 30$ grid.

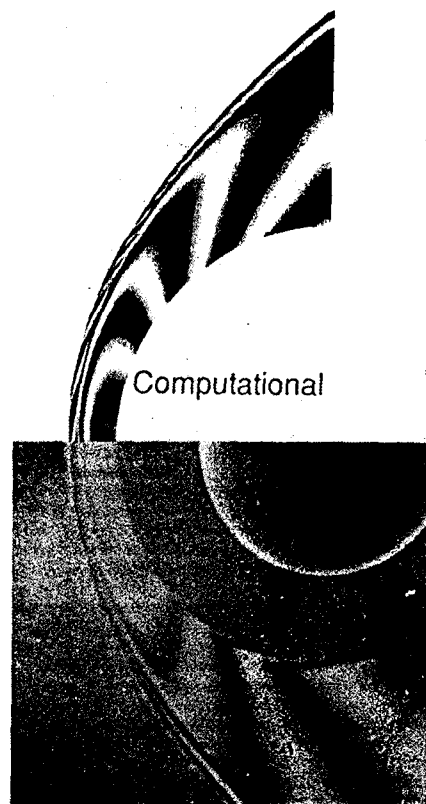


Fig. 12 Comparison of case 3 experimental and computational interferograms for the Park et al.⁴ rate model on $50 \times 50 \times 30$ grid.

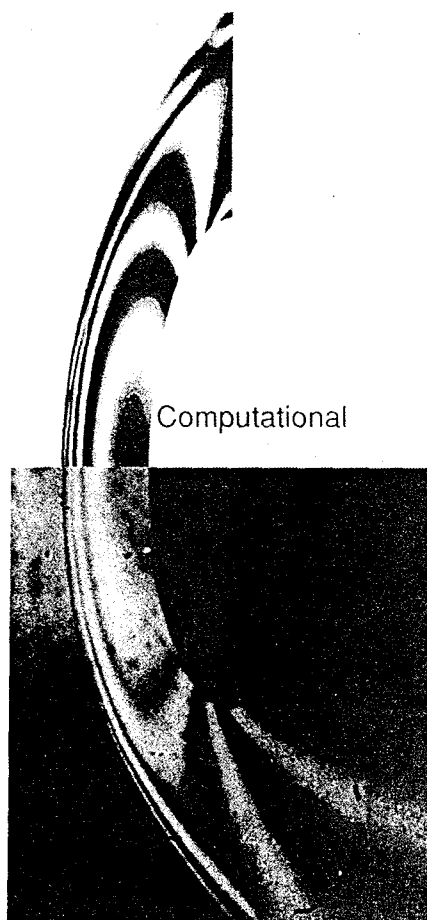


Fig. 11 Comparison of case 2 experimental and computational interferograms for the Park et al.⁴ rate model on $50 \times 50 \times 30$ grid.

effect is verified throughout the flowfield by an underprediction in the fringe shift. The McKenzie rates predict a maximum density rise of $(\rho/\rho_\infty)_{\max} = 9.05$, slightly lower than the $(\rho/\rho_\infty)_{\max} = 9.35$ predicted by the Park rates. However, this small discrepancy in the density rise results in a significant change in the computed interferograms.

The influence of the reaction rates on the density rise can be seen in the plots of the mass fractions along the stagnation line as seen in Figs. 7 and 8. The Park rates predict a faster dissociation of O_2 . This faster rate is consistent with the rate comparison of Fig. 2. Park predicts only a moderate increase in the dissociation rate of CO_2 as compared to the McKenzie rate. This moderate difference is accounted for by the fact that both chemical kinetics models predict a temperature behind the shock of approximately 5000 K. Therefore, for a large portion of the shock layer the two models predict almost identical CO_2 dissociation rates as shown in Fig. 1. However, at the higher temperatures in the vicinity of the shock, Park predicts faster dissociation rates. As a result of the high temperatures near the shock and the faster dissociation rate of O_2 , Park predicts overall faster reaction rates resulting in a greater density rise.

Cases 2-4 produced similar results, with the Park reaction rates very closely reproducing the experiment. The McKenzie reaction rates consistently underpredicted the density rise. The results of case 5 were inconclusive. For case 5, neither reaction rate model showed a close comparison to the experiment. Both models significantly overpredicted the density rise. Because of the close comparison and similar results of the first four cases, the conclusion is that the experimental data of case 5 differ significantly from the nominal test conditions. On the basis of the comparisons of the first four cases, the conclusion is that the Park et al. model more closely predicts the physics of the dissociation dominated flow for the temperature and energy range of the experiment. For this reason, the McKenzie model was abandoned and a more detailed analysis was performed on the Park et al. model.

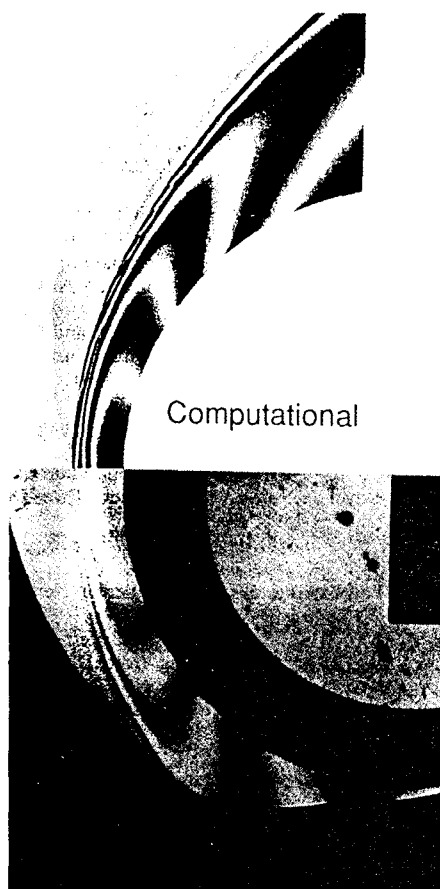


Fig. 13 Comparison of case 4 experimental and computational interferograms for the Park et al.⁴ rate model on $50 \times 50 \times 30$ grid.

Solutions were obtained for the Park et al. model on uniformly distributed $50 \times 50 \times 30$ grids. The converged solutions were then used in conjunction with the SAGE code¹⁸ to adapt the finite volume grids to regions with high density and mass fraction gradients. This ensures the most efficient use of the grid points in computing interferograms. Converged solutions were then obtained on the $50 \times 50 \times 30$ adapted grids ensuring adequate resolution of the flow features. Figure 9 shows a representative adapted grid. Due to the symmetry of the flowfield, only one-quarter of the cylinder needs to be modeled. In Fig. 9 all four quadrants are shown for clarity.

Figures 10–13 show the experimental comparison for Park's reaction rate model on the dense grid for cases 1–4, respectively. All four cases show close comparison to the experimental data. The discrepancies that exist are minor and can be accounted for by the margin of error in the experimental data. The nozzle reservoir pressure has an uncertainty of $\pm 12\%$, and the shock velocity has an uncertainty of $\pm 5\%$. For this reason, the Park et al. chemical kinetics model has been validated as closely as possible for the available experimental data.

An investigation was also performed to study the effects of the modeling of the vibrational relaxation time on the experimental comparison. Both the Millikan-White expression using $\theta_v = 945$ K for all modes [Eq. (5)] and the Camac expression [Eq. (7)] were implemented on identical grids for case 1. The interferograms produced were insensitive to the relaxation model employed. No differences in the computed interferograms could be discerned. However, a plot of the temperature profiles along the stagnation line revealed differences in the two models (see Fig. 14). The Millikan-White expression predicted a slower relaxation time, resulting in increased thermal nonequilibrium. The differences in the temperature profiles are small compared to the differences produced by the choice

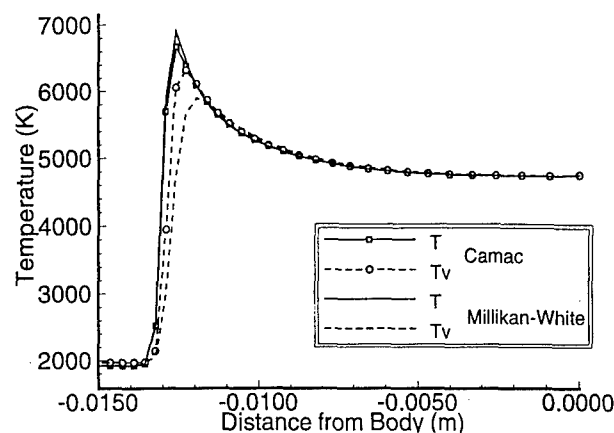


Fig. 14 Comparison of temperature distribution along stagnation line for Millikan-White and Camac vibrational relaxation expressions.

of the chemical kinetics model. Also, Chen et al.⁶ showed that the effect of vibrational relaxation time on surface heating rates is negligible. Therefore, the chemical kinetics model employed is of greater importance. Because the Camac expression is a direct fit to experimental data for dissociating CO_2 flows, it should be used.

Conclusions

The results of this study demonstrate that, for the cases examined, the chemical kinetics model of Park et al. reproduces the available experimental data more accurately than the chemical kinetics model of McKenzie. The Park reaction rate model produces results in very good agreement with experiment. Within the limitations of the experiment and the sensitivity of the interferograms to density variations, it is not possible to offer any improvements to this chemical kinetics model. This model has been shown to correctly model the physics of the flow for conditions in the range $h_{0\infty} = 10$ MJ/kg and $2000 < T < 7000$ K. Further studies need to be performed to validate the model for flows with higher postshock temperatures. With this exception, the Park et al. model has been shown to correctly model the density field at conditions similar to Martian entry flows. It should be noted that the experimental freestream is partially dissociated, making a direct comparison to actual flight conditions difficult.

The comparison to experimental interferograms was shown to be insensitive to the vibrational relaxation model employed. This insensitivity is due in part to the very fast vibrational relaxation time of CO_2 . However, the expression developed by Camac is a direct fit to experimental data for dissociating CO_2 flows. Therefore, the Camac expression is preferred to the Millikan-White expression for the relaxation time of CO_2 . Further work needs to be performed to validate the premise that the vibrational energies of all of the species can be characterized by a single temperature T_v . The strong resonance coupling that exists between the vibrational modes of the CO_2 molecule may not extend to other molecules. In particular, a decoupling of the CO molecule may require the modeling of separate vibrational temperatures $T_{v\text{CO}_2}$ and $T_{v\text{CO}}$. The investigation of these vibrational relaxation models will require new experiments that have been specifically designed to be sensitive to changes in vibrational energy.

Acknowledgments

This work was supported by the following grants: NASA Langley Research Center Cooperative Agreement NCC1-140 with the Aerothermodynamics Branch of the Space Systems Division, and NASA Grant NAGW-1331 to the Mars Mission Research Center at North Carolina State University.

References

- ¹McKenzie, R. L., "An Estimate of the Chemical Kinetics Behind Normal Shockwaves in Mixtures of Carbon Dioxide and Nitrogen for Conditions Typical of Mars Entry," NASA TN D-3287, Feb. 1966.
- ²Evans, J. S., Schexnayder, C. J., Jr., and Grose, W. L., "Effects of Nonequilibrium Ablation Chemistry on Viking Radio Blackout," *Journal of Spacecraft and Rockets*, Vol. 11, No. 2, 1974, pp. 84-88.
- ³Grose, W. L., Falanga, R. A., and Sutton, K., "An Analysis of Communications Blackout for Pioneer Venus Entry Probes," AIAA Paper 75-182, Jan. 1975.
- ⁴Park, C., Jaffe, J., Howe, J., and Candler, G. V., "Chemical Kinetic Problems of Future NASA Missions," AIAA Paper 91-0464, Jan. 1991.
- ⁵Candler, G. V., "Computation of Thermo-Chemical Nonequilibrium Martian Atmospheric Entry Flows," AIAA Paper 90-1695, June 1990.
- ⁶Chen, Y. K., Henline, W. D., Stewart, D. A., and Candler, G. V., "Navier-Stokes Solutions with Surface Catalysis for Martian Atmospheric Entry," *Journal of Spacecraft and Rockets*, Vol. 30, No. 1, 1993, pp. 32-42; also AIAA Paper 92-2946, July 1992.
- ⁷Camac, M., "CO₂ Relaxation Processes in Shock Waves," *Fundamental Phenomena in Hypersonic Flow*, edited by J. G. Hall, Cornell Univ. Press, Ithaca, NY, 1966, pp. 195-215.
- ⁸Vincenti, W. G., and Kruger, C. H., Jr., *Introduction to Physical Gas Dynamics*, Krieger, Malabar, FL, 1965, pp. 198-206.
- ⁹Millikan, R. C., and White, D. R., "Systematics of Vibrational Relaxation," *Journal of Chemical Physics*, Vol. 39, No. 12, 1963, pp. 3209-3213.
- ¹⁰Gaydon, A. G., "Temperature Measurement and Relaxation Processes in Shock Tubes," *Fundamental Phenomena in Hypersonic Flow*, edited by J. G. Hall, Cornell Univ. Press, Ithaca, NY, 1966, pp. 159-170.
- ¹¹Park, C., *Nonequilibrium Hypersonic Aerothermodynamics*, Wiley, New York, 1990, pp. 57-60.
- ¹²Candler, G. V., "The Computation of Weakly Ionized Hypersonic Flow in Thermo-Chemical Nonequilibrium," Ph.D. Thesis, Dept. of Aeronautics and Astronautics, Stanford Univ., Stanford, CA, June 1988.
- ¹³Candler, G. V., and MacCormack, R. W., "Computation of Weakly Ionized Hypersonic Flows in Thermochemical Nonequilibrium," *Journal of Thermophysics and Heat Transfer*, Vol. 5, No. 3, 1991, pp. 266-273.
- ¹⁴Yoon, S., and Jameson, A., "An LU-SSOR Scheme for the Euler and Navier-Stokes Equations," AIAA Paper 87-0600, Jan. 1987.
- ¹⁵Eberhardt, S., and Imlay, S. T., "A Diagonal Implicit Scheme for Computing Flows with Finite-Rate Chemistry," AIAA Paper 90-1577, June 1990.
- ¹⁶Imlay, S. T., Roberts, D. W., Soetrismo, M., and Eberhardt, S., "Nonequilibrium Thermo-Chemical Calculations using a Diagonal Implicit Scheme," AIAA Paper 91-0468, Jan. 1991.
- ¹⁷Hassan, B., Candler, G. V., and Olynick, D. R., "The Effect of Thermo-Chemical Nonequilibrium on the Aerodynamics of Aerobreaking Vehicles," AIAA Paper 92-2877, July 1992.
- ¹⁸Davies, C. B., and Venkatapathy, E., "Application of a Solution Adaptive Grid Scheme, SAGE, to Complex Three-Dimensional Flows," AIAA Paper 91-1594, June 1991.
- ¹⁹Goldstein, R. J., *Fluid Mechanics Measurements*, Hemisphere, New York, 1983, pp. 397-413.
- ²⁰Merzkirch, W., *Flow Visualization*, Academic, New York, 1974, pp. 102-116.
- ²¹Alpher, R. A., and White, D. R., "Optical Refractivity of High-Temperature Gases. I. Effects Resulting from Dissociation of Diatomic Gases," *Physics of Fluids*, Vol. 2, No. 2, 1959, pp. 153-161.
- ²²Kaye, G. W. C., and Laby, T. H., *Tables of Physical and Chemical Constants and Some Mathematical Functions*, Longman, New York, 1986, pp. 99, 100.
- ²³Anderson, J. D., Jr., *Hypersonic and High Temperature Gas Dynamics*, McGraw-Hill, New York, 1989, pp. 581, 582.

RECENT RESULTS FROM HYPERVELOCITY RESEARCH IN T5

H.G. Hornung¹, E.B. Cummings², P. Germain³, S.R. Sanderson², B. Sturtevant⁴ and C.-Y. Wen⁵
Graduate Aeronautical Laboratories, California Institute of Technology

Abstract

Results are presented from a selection of the graduate research projects that were carried out in the T5 hypervelocity shock tunnel laboratory during the last two years. The projects presented are:

1. Hypervelocity flow over spheres. Differential interferometry and heat transfer measurements are used in air, nitrogen, and carbon dioxide flows to test numerical results and a new stand-off distance correlation.
2. High-enthalpy real-gas effects in boundary layer transition on a slender cone. Heat transfer measurements and resonantly enhanced flow visualization provide new data on the effect of reservoir enthalpy on transition. The effect is quite strongly stabilizing. The visualization shows the structure of high-enthalpy transitional and turbulent boundary layers.
3. Real-gas effects in shock-on-shock interaction. Flow visualization indicates that the range of shock impingement points for which enhanced heating occurs is increased by high-enthalpy real-gas effects. Some flow features are changed qualitatively.
4. A new diagnostics technique: Laser-induced thermal acoustics. This method provides accurate point measurement of the speed of sound, bulk viscosity, and susceptibility of a gas.

The experience with T5 over the first 700 runs shows that its operation in a university environment is a cost-effective way of improving the understanding of phenomena in hypervelocity gasdynamics.

1. INTRODUCTION

At the last AIAA Ground Testing Meeting, we presented the performance characteristics of the free-piston hypervelocity shock tunnel T5, the problems encountered during the shake-down period, its limitations, and some data on flow duration and repeatability, see Hornung (1992).

Further experience in operating T5 has led us to make a study of the limitations of high-enthalpy facilities, see Hornung (1993). One of the diagrams of this study is reproduced here to illustrate the relation of the two main types of hypervelocity facilities, the expansion tube and the reflected-shock tunnel, relative to each other. This is done in a Mollier chart, see Fig. 1.

¹ Kelly Johnson Professor of Aeronautics, Director of GALCIT, Member, AIAA

² Graduate Research Assistant

³ Research Associate, NRC, Canada

⁴ Professor of Aeronautics, Member, AIAA

⁵ Student member, AIAA

The square symbols are the actual thermodynamic states reached by the test gas in an example of the free-piston shock tunnel operation. To achieve a reservoir specific enthalpy of 16 MJ/kg, say, the shock speed needs to be approximately 4 km/s. Thus, the specific enthalpy after the shock is 8 MJ/kg. This corresponds to $h/R = 28,000$ K, where R is the specific gas constant for air at room temperature. If the initial state of the gas in the shock tube is $s/R = 24$, and $T = 300$ K, the primary shock takes the gas to the state $s/R = 30$, $h/R = 24,000$ K. These two points are connected schematically by a straight dashed line in the diagram. The test gas is then brought to rest by the reflected shock, which raises the entropy and enthalpy further, to [33.5, 60,000 K], again shown by a square symbol and schematic dashed line. From this hot state, the gas is re-accelerated by a steady expansion, initially at constant entropy while the expansion proceeds at equilibrium, and with a slight entropy increase toward the end of the expansion. For simplicity, the expansion is drawn at constant entropy.

The expansion tube shares the first process with the shock tunnel. However, instead of then stopping the gas by a reflected shock, and converting the kinetic energy to thermal energy, and then re-accelerating it in a steady expansion, it processes the already moving gas by an unsteady expansion to the desired free-stream state. It therefore always retains some of its energy in kinetic energy form, so that the gas never sees the high temperature encountered in reflected-shock tunnels. At the same time, the entropy

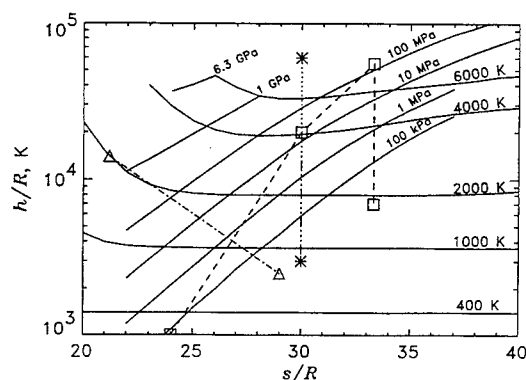


Fig. 1. Mollier diagram for equilibrium air, showing lines of constant pressure and temperature. An example of the processes in a reflected-shock tunnel is shown by the dashed line and square symbols. The lower asterisk represents the exit condition in an expansion tube that starts with the same shock tube conditions as in the reflected-shock example. The upper asterisk represents the effective reservoir state of the expansion tube. The triangles show reservoir and exit condition of the direct energy addition facility proposed at Princeton.

remains considerably lower, so that the effective reservoir pressure is extremely high. The effective reservoir state of the expansion tube is shown as the top asterisk in the Mollier chart. This high pressure (>1 GPa) is also never seen by the facility, since the flow is never stopped.

The expansion tube has the important advantages that the material of the machine is not exposed to the extreme temperatures and pressures encountered in the shock tunnel, and that the test gas is not as highly dissociated, and therefore has less atomic oxygen in the free stream gas. These advantages are obtained at the expense of considerably smaller test time and size for a given shock tube diameter. The smaller test time is also bugged by uncertainties about the secondary diaphragm behavior, some of which have been studied by Roberts et al. (1993). To date, the largest expansion tube is one operated at the General Applied Sciences Laboratory in New York by a team headed by Dr. John Erdos. This has a shock tube (and test section) diameter of 150 mm. At present it has a cold helium driver, so that the enthalpy at which it can be run is limited to approximately 15 MJ/kg, see, e.g., Bakos et al. (1992). The largest free-piston reflected-shock tunnel is being operated by the group under Dr. Georg Eitelberg in the DLR, Göttingen, Germany, with a shock tube diameter of 150 mm, and a test section diameter of 800 mm.

(As a matter of interest, Fig. 1 also shows the approximate Mollier path of a proposed direct energy addition facility, which has the aim of producing a free stream completely free of atomic oxygen and NO, by avoiding temperatures higher than 2000 K.)

The relatively more rapid development of the reflected-shock tunnel is due in part to the perseverance in the field of hypersonics of groups like Calspan, Buffalo (Holden), and Australian National University (Stalker) during the 1970's and early 1980's, who developed and operated reflected-shock tunnels. T5 is very much a derivative of the development of the free-piston driven devices developed by Stalker in Australia. The Stalker group now operates free-piston reflected-shock tunnels and expansion tubes at Queensland University, see other presentations at this meeting.

During the last two years, T5 has been used in some 400 runs, mostly for graduate research, but also for a few proprietary tests for the European Space Agency, Hitachi, and Mitsubishi Heavy Industries. In this paper, we report on selected results from the graduate research projects on

1. Hypervelocity flow over spheres,
2. High-enthalpy real-gas effects in boundary layer transition on a slender cone,
3. Real-gas effects in shock-on-shock interaction,
4. A new diagnostics technique: Laser-induced thermal acoustics.

Two other projects on high-speed hydrogen injection and on the computation of the gas-dynamical processes in free-piston shock tunnels are being presented in separate papers at this conference, see Bélanger and Hornung (1994a&b).

2. HYPERVELOCITY FLOW OVER SPHERES

An extensive series of experiments on flow over spheres has been completed. This involved nitrogen, air and carbon dioxide flows covering the full range of enthalpy of T5, ranging from perfect-gas to near-equilibrium flow, and a large range of pressure. Differential interferometry and surface heat transfer constituted the diagnostics used. The experiments were accompanied by detailed numerical computations of the flow fields, which were used to construct interferograms for comparison with the experimental ones. Theoretical analysis of the problem led to a complete understanding of the correlation of the dimensionless stand-off distance with dimensionless reaction-rate parameter, and its extension to reacting gas mixtures. Numerical and experimental results support the correlation very well. A previous theoretical analysis of dissociating flow along a streamline downstream of a curved shock has been extended to include the effects of recombination. The limits of binary scaling were delineated. Initial exploratory experiments on the detection of the high vorticity layer and its stability were performed.

2.1 Interferometry and heat flux measurements

The experimental differential interferograms were compared with the images constructed from computational flow fields. Generally, good agreement of fringe pattern and shock shape was observed. Fig. 2 shows the comparison of experimental and computational differential interferograms of the flow of nitrogen over a 4 in. diameter sphere at a specific reservoir enthalpy of 16 MJ/kg and a reservoir pressure of 60 MPa. As may be seen, the features of the photo are faithfully reproduced by the computation, both qualitatively and quantitatively, in most of the flow field. Small differences near the shock give valuable information about the beginning of the dissociation process.

Experimental heat flux measurements show:

1. Good agreement among the measured stagnation point heat transfer rates, computational results and Fay and Riddell's theoretical predictions. This also provides confirmation of T5 enthalpy.
2. For nitrogen and air, the measured heat flux distributions were also in good agreement with numerical results and Lees' theory.
3. For carbon dioxide, large differences between experimental and theoretical heat flux distributions were observed. Early transition, tripped by surface roughness is a possible cause.

2.2 Binary scaling law

An approximate analytical solution was obtained for inviscid hypervelocity dissociating flow over spheres. The solution explains the correlation between the dimensionless stand-off distance and the dimensionless reaction rate parameter previously observed by Hornung (1972) for nitrogen. The physics of the correlation is equivalent to binary scaling. Based on the solution, a new dimensionless reaction rate parameter Ω is defined to generalize Hornung's correlation for more complex gases than nitrogen. The physical meaning of Ω is recognized as the ratio of

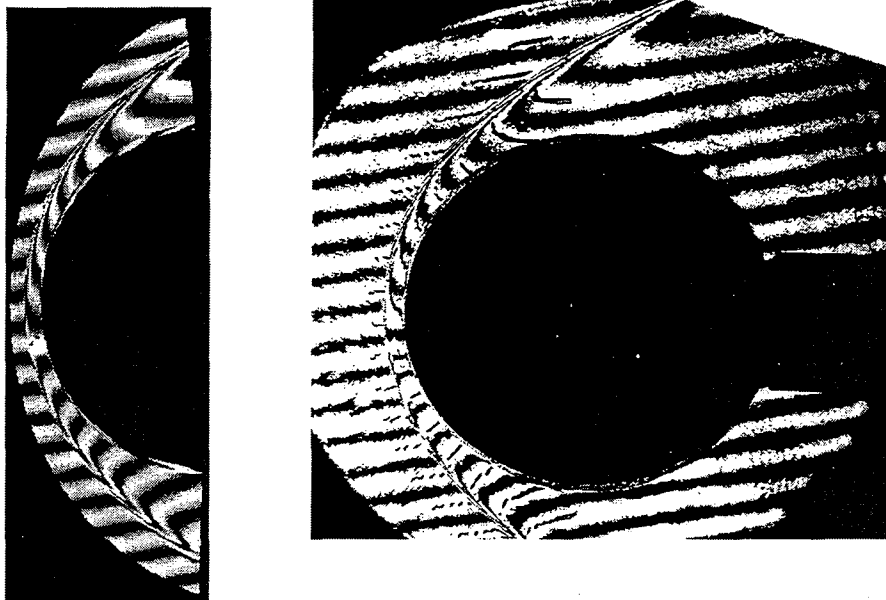


Fig. 2. Comparison of experimental and computed differential interferograms of nitrogen flow over a sphere. Free-stream conditions: 5.08 km/s, 0.04 kg/m³, 16.56 MJ/kg. The photograph on the right is a finite-fringe differential interferogram of nitrogen flow over a sphere. The picture on the left is a corresponding computed interferogram at the same conditions as the experiment. Except for a slight difference in the vicinity of the shock, the two pictures are virtually congruent. To show this, a line along the center of the calculated white fringe is superimposed on the photograph.

the energy absorption rate by chemical reactions just after the normal shock to the input rate of free-stream kinetic energy. This suggests that there exists a universal relationship which applies to all gases and free-stream conditions, provided that the Mach number is sufficiently high. The form of the function is also determined by the approximate analysis and is presented together with computational results for air in Fig. 3 and together with experimental results from T5 for carbon dioxide in Fig. 4. Experimental and numerical results confirm the new correlation.

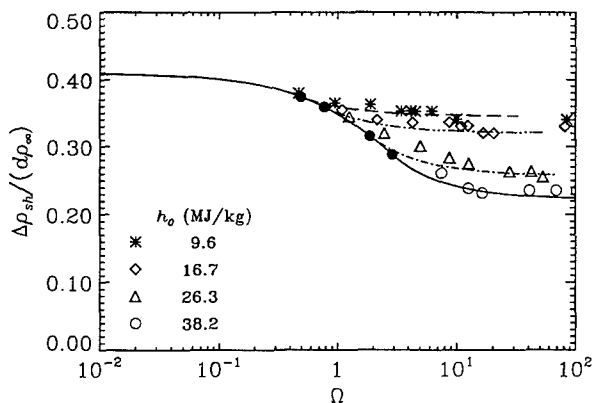


Fig. 3. Dimensionless stand-off distance plotted against reaction rate parameter for different specific reservoir enthalpies in air. The symbols represent computational results. The filled circle is the point at which the curve branches off from the solid line for each Pe/ρ_{sh} .

The effect of nonequilibrium recombination downstream of a curved two-dimensional shock was also investigated. An analytical solution for an ideal dissociating gas was obtained, giving an expression for dissociation fraction as a function of temperature on a streamline. The solution agrees well with the numerical result and provides a rule of thumb to check the validity of binary scaling for the experimental conditions. The effects upon the binary scaling of the large difference in free-stream temperature between flight and free-piston shock tunnel conditions are discovered.

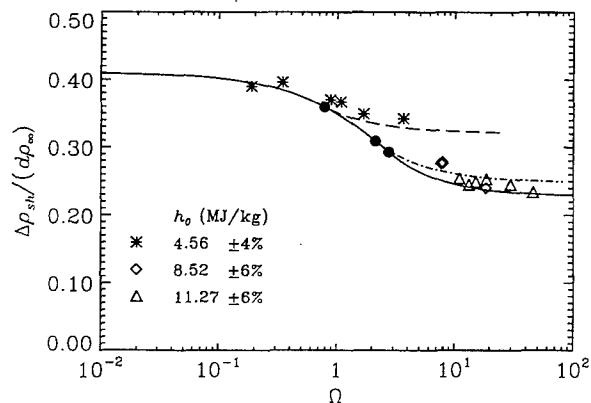


Fig. 4. Dimensionless stand-off distance plotted against reaction rate parameter for different specific reservoir enthalpies in carbon dioxide. The symbols represent experimental results.

Though theoretical and computational results show that recombination is important in parts of the flow field, binary scaling is a satisfactory model for global quantities such as the stand-off distance.

2.3 Vorticity generation by curved shock

Fig. 5 shows a partial view of a resonantly-enhanced shadowgraph of carbon dioxide flow over a sphere. Streamlines are marked by seeding the flow with sodium and using a light source tuned to one of the sodium D lines, see also section 3. At the side of the sphere these show similarities with the instability of a shear layer. The vortical structures may be the result of Kelvin-Helmholtz instability of the high-vorticity layer at the edge of the high-entropy layer near the body. If they are, to our knowledge, this resonantly-enhanced shadowgraph is the first visualization of this phenomenon. Further experiments are needed before definite conclusions may be reached. Nevertheless, the resonantly-enhanced shadowgraphic technique provides a promising tool for studying the vorticity-interaction problem in hypervelocity blunt-body flows.

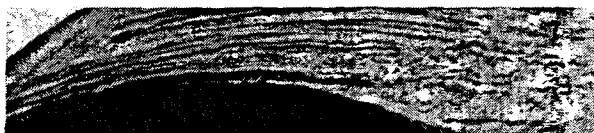


Fig. 5. Partial view of a resonantly-enhanced shadowgraph of CO_2 flow over a sphere of 4 in diameter. Free-stream condition: CO_2 , 3.55 km/s, 0.081 kg/m³, 11.27 MJ/kg.

3. TRANSITION AT HIGH ENTHALPY

One of the most serious gaps in the knowledge of hypervelocity flows is that concerning transition to turbulence in the boundary layer. T5 created the opportunity to achieve Reynolds numbers in the right range at high enthalpy in a steady nozzle expansion. Reflected-shock tunnels can only provide a notoriously noisy environment. The question therefore needs to be addressed as to whether the mechanism of transition that occurs is the same as that occurring in flight. Nevertheless, an experimental study was undertaken, which yielded some interesting results.

A slender cone of half-angle 5 deg. was instrumented with thermocouple heat transfer gauges. Flows of air, nitrogen, carbon dioxide, and helium over this cone were studied at specific reservoir enthalpies ranging from 3 to 22 MJ/kg. Flow visualization was achieved with resonantly enhanced interferometry. The resonant enhancement is necessary to make the visualization technique sufficiently sensitive.

The experiments show that the mechanism of transition in the range studied is via the Tollmien-Schlichting instability. This is not surprising, since the frequency of the second mode at these conditions is approximately 1 MHz which is higher than any of the noise sources in the facility. On the other hand, the TS frequency is typically 150 kHz, a value which is abundantly present in the noise spectrum. Two flow visualization photographs of a transitional and of a turbulent boundary layer are shown in Fig. 6 and Fig. 7.



Fig. 6. Flow of nitrogen at $h_0 = 11$ MJ/kg and $p_0 = 60$ MPa (run 360). This resonantly enhanced interferogram shows the boundary layer on the top of the cone, starting on the left from $x = 510$ mm (corresponding to $Re = 2.75$ million) to $x = 680$ mm ($Re = 3.77$ million). The pictures below magnify portions of the one above three times ($3\times$). A wave in the laminar part of the flow appears distinctly and its wavelength is approximately 1.5 cm.



Fig. 7. Flow of nitrogen at $h_0 = 20$ MJ/kg and $p_0 = 55$ MPa. Resonantly enhanced interferogram showing a turbulent boundary layer.

The most interesting result of the study is that a clear trend may be observed in the behavior of the transition Reynolds number with specific reservoir enthalpy. This trend is stronger for air than for nitrogen, see Fig. 8. In this, the transition Reynolds number is evaluated at the reference temperature, in order to eliminate the separate dependence of the data on Mach number, specific heat ratio, and wall temperature. Since the lowest enthalpy at which dissociative real-gas effects are observed is lower in air than in nitrogen, this appears to indicate that the appropriate dimensionless variable to plot on the horizontal axis is h_0/D , where D is some representative dissociation energy. In the case of nitrogen, the value of D is, of course, the dissociation energy of nitrogen. If D is taken to be the dissociation energy for oxygen in the case of air, the two curves do not quite collapse when plotted against h_0/D , this procedure overcompensates slightly for the difference between air and nitrogen. To test the notion that the effect is proportional to h_0/D , a few experiments were carried out with carbon dioxide, with even lower first dissociation energy, and with helium, where ionizational real-gas effects appear only at very high enthalpy, well beyond the range tested. The carbon dioxide flows indeed showed a much stronger dependence of Re_{tr}^* on h_0 than nitrogen and air, and helium showed no dependence at all. Further experiments are planned to examine this effect in more detail.

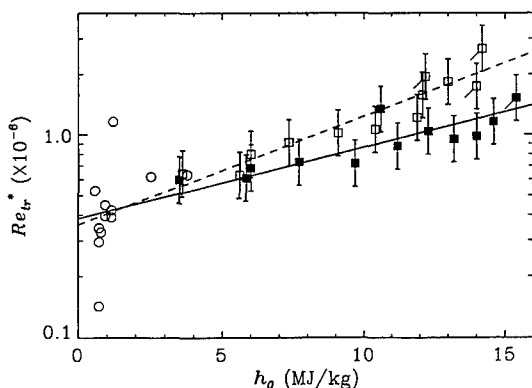


Fig. 8. Transition Reynolds number evaluated at the reference temperature. Our data are shown as square symbols (open for air and solid for nitrogen). The error bar shown is an approximation of the accuracy in determining Re_{tr}^* . The data shown as open circles come from DiCristina (1970) and Demetriades (1977). The two lines are least-squares-fit approximations of the open or the solid symbols respectively.

4. SHOCK-ON-SHOCK INTERACTION

4.1 Introduction

The impingement of shock waves on blunt bodies in steady supersonic flow is known to cause extremely high local heat transfer rates and surface pressures. Although this phenomenon has been studied in cold hypersonic flow, the effects of dissociative relaxation processes are unknown. Shock impingement phenomena, which constrain the development of hypervelocity vehicles, are discussed in the literature by many authors, notably by Edney (1968 a,b).

For the inviscid, compressible flow of a perfect gas a sufficient set of dimensionless parameters to describe any dimensionless quantity ϕ in the flow is,

$$\phi = \phi(M, \gamma, \beta_1, \Lambda, \Gamma),$$

where M is the free stream Mach number, γ is the ratio of specific heats, β_1 is the impinging shock angle, Λ describes the position of the impinging shock and Γ defines the body geometry. Consider the case of a given gas and fixed free stream condition, impinging shock strength and body geometry. The only remaining dependence is then the location of the impingement point relative to the body, i.e.,

$$\phi = \phi(\Lambda).$$

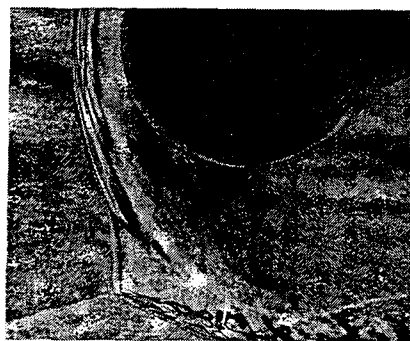
On the basis of an experiment such as this, Edney (1968 a,b) observed and categorized six interaction regimes known as types I–VI. Edney rationalized the observed flow fields through local analysis about shock wave intersection points in the pressure–flow deflection angle plane (p – δ plane). The key conclusion drawn from such an analysis is the role of the three-shock solutions. Based on the assumption of straight shocks in the vicinity of the interaction, the flow field for the global type IV interaction, whereby a supersonic jet penetrates a region of low subsonic flow [see Edney (1968 a,b) or Fig. 11], can be solved approximately as a free streamline flow up to some unknown length scale. Typically this length scale is specified in terms of the width of the jet.

According to Edney's model, the heat transfer is determined by the attachment at the body surface of the shear layers generated at the shock impingement points. A correlation was obtained between local pressure and local heat transfer rate at the surface. A further observation made by Edney is that the jet curvature increases as the intersection point moves closer to the normal-shock point. Some recent contributions to the literature are noted in the references.

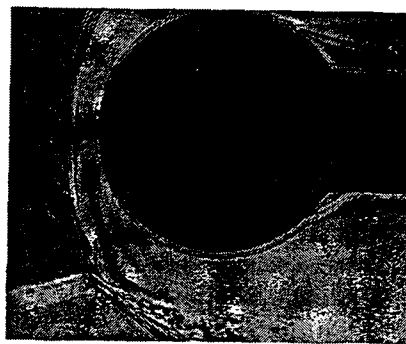
4.2 Experiment and results

We have conducted an experimental investigation of the nominally two-dimensional mean flow that results from the impingement of an oblique shock wave on the leading edge of a cylinder. These initial experiments, comprising 35 shots, were conducted with nitrogen test gas at nozzle reservoir enthalpies of 3 MJ/kg and 12.5 MJ/kg and reservoir pressures of 12 MPa and 25 MPa, respectively. The reservoir gas was expanded through a contoured axisymmetric nozzle with area ratio 109.5 to yield a nominal Mach number of 5.5 in the test section. The cylinder was 37.5 mm in diameter with aspect ratio 4.5 and the flow was deflected 7 degrees by the incident planar shock wave.

The effects of variations in shock impingement geometry were visualized using infinite fringe differential interferometry with vertical beam shear. Figs. 9 to 11 illustrate type II, III and IV interactions, at stagnation enthalpies of 3 MJ/kg and 12.5 MJ/kg. The incident shock is curved in the transverse plane (concave down) at the edge of test section and some fringe shift is observed below this wave. However, the main centerline disturbance is generally at the top of the line-of-sight-integrated image.

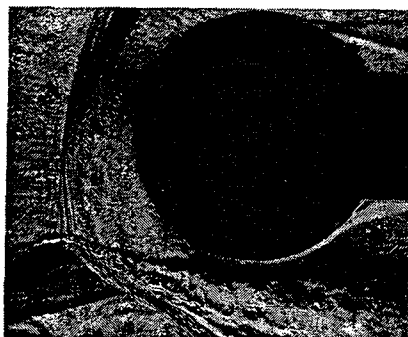


(a) 3 MJ/kg

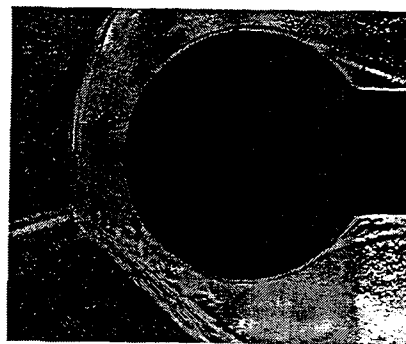


(b) 12.5 MJ/kg

Fig. 9. Differential interferograms of type II interactions.

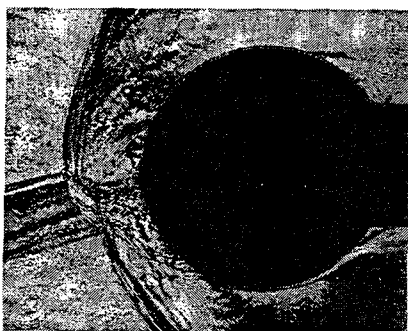


(a) 3 MJ/kg

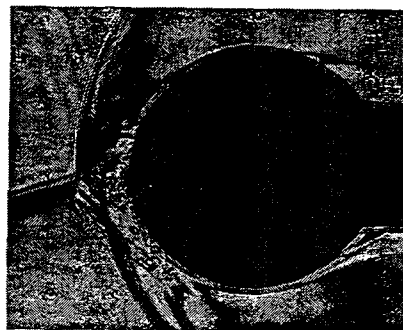


(b) 12.5 MJ/kg

Fig. 10. Differential interferograms of type III interactions.



(a) 3 MJ/kg



(b) 12.5 MJ/kg

Fig. 11. Differential interferograms of type IV interactions.

At the lowest impingement point reported in this paper the type I-II transition has already occurred with the incident shock wave impinging somewhat below the lower sonic line (Fig. 9). In the low enthalpy case a Mach stem connects the λ -shock pattern at the impingement point to the bow shock of the cylinder. At the intersection point a strong vortex sheet is generated, separating the upper region of subsonic flow from the lower region of supersonic flow. No transmitted wave is resolvable at the upper end of the Mach stem which appears to join smoothly into the bow shock in the vicinity of the sonic line. The upper portion of the bow shock remains symmetrical. In the high enthalpy case the bow shock remains undisturbed. However, a point of inflection is observed immediately above the intersection point.

In the type III experiments (Fig. 10) the incident shock wave intersects the bow shock wave in the subsonic region, somewhat below the geometric stagnation point. For both enthalpies the Mach stem has merged with the bow shock wave and the λ -shock pattern is preserved at the intersection point. The influence of the impinging shock wave is now global and both the radius of curvature and the stand-off distance of the asymmetrical upper portion of the bow shock have increased to match the λ -shock pattern at the impingement point. Dominated by the inertia of the supersonic stream, the shear layer is deflected only in the immediate vicinity of the cylinder.

Generally, the stand-off distance decreases with increasing enthalpy and this influences the impingement of

the shear layer on the body. In the high-enthalpy case, the resulting compression waves that are observed as a series of nearly vertical white lines below the impingement point, steepen the lower shock. Note the analogy between this phenomenon and the mechanism of complex Mach reflection.

When the incident shock wave impinges in the vicinity of the normal-shock point a type IV flow results (Fig. 11). The λ -shock pattern is preserved, and the supersonic transmitted portion of the bow shock forms a second inverted λ -shock with the subsonic continuation of the bow shock below the interaction. The flow behind the oblique shock wave connecting the two λ -shocks is supersonic and forms a jet that turns upwards under the action of the pressure gradient produced by the second λ -shock. The strongly curved shear layer generated at the upper λ -shock forms large plumes as it passes above the cylinder. The stand-off distance and jet width are reduced in the high-enthalpy case but this also depends strongly on the location of the impinging shock. A portion of the supersonic flow is now turned, so that it passes above the cylinder, and hence the stagnation streamline must pass through the supersonic jet. The stagnation density is higher for streamlines that pass through the supersonic jet than for streamlines that cross the adjacent strong bow shock. The higher density and large unsteady velocity gradients produced by the impingement of the supersonic jet provide the mechanism for local increase of the heat transfer rate.

4.3 Conclusions

Experiments conducted in T5 provided insight into real-gas effects on the global flow. Generally, real-gas effects are seen to increase the range of shock impingement points for which enhanced heating occurs. They further influence the Mach stem form in type II flows, the deflection of the shear layer in type III flows and the length scales associated with the type IV jet.

5. LASER-INDUCED THERMAL ACOUSTICS

5.1 Description of LITA diagnostic technique

Over the past year, work on optical diagnostics for T5 has progressed markedly with the development at GALTIT of laser-induced thermal acoustics, or LITA, a new technique superior in many respects to other laser diagnostic techniques. In the first series of experiments LITA has provided relatively simple, accurate, single-shot, spatially resolved measurements of sound speed, transport properties, and collisional thermalization rate in laboratory air. Current experiments apply LITA for single-shot measurement of these properties, as well as of the complex susceptibility, susceptibility spectra, and gas velocity. Absolute species concentration and temperature measurements may be extracted from susceptibility spectra. The work on LITA performed at GALTIT has the interest of the wider combustion diagnostics community because

- quantitative signal analysis is simple (cf., LIF, DFWM),
- exhaustive information about probed species is not required (cf., LIF),

- LITA excels in strongly quenching environments (e.g., where collision rates are high, a requirement for fast chemistry; cf., LIF),
- LITA requires only standard lasers and equipment, and
- LITA's capabilities exceed those of other techniques (e.g., single-shot transport-property, absolute concentration, and velocity measurements)
- LITA signals are relatively strong.

LITA is a four-wave mixing (FWM) technique related to coherent anti-Stokes Raman scattering (CARS) and degenerate FWM (DFWM). In FWM techniques, crossed-laser beams form electric-field interference "gratings" in the probed volume. Electric field gratings generate susceptibility (index-of-refraction) gratings via nonlinearities of the probed medium. These gratings scatter light from a third beam into the signal beam. If the intensity of the signal beam can be related to properties of the medium, FWM can be used to measure these properties remotely. The principal difference between the techniques is the type of nonlinearity used to form the susceptibility gratings. CARS and DFWM form gratings by quantum mechanical effects.* These gratings have short lifetimes (< 5 ns at STP), since they are destroyed by molecular collisions. LITA gratings are acoustic: crossed driver lasers generate acoustic pressure and temperature gratings via electrostriction and thermalization, two semi-classical opto-acoustic effects. Acoustic gratings are damped by thermal and viscous diffusion on a much longer time scale (e.g. 1 μ s) than quantum mechanical gratings. Longer time scales permit single-shot time resolution of the evolution of the signal which allows sound speed measurement. Furthermore, the formation and lifetime of acoustic gratings are *enhanced* by quenching, which has the opposite effect on quantum-mechanical gratings.

The mathematics of acoustic grating formation is generally far simpler than that of quantum-mechanical gratings. This makes the expression relating experimental LITA signals to gas properties simpler than that of DFWM or CARS. Thus, it was possible to predict the LITA signal with an analytical expression derived previously from the linearized equations of light scattering and hydrodynamics, see Cummings (1992). By fitting the experimental signal to the prediction, sound speeds could be obtained to an accuracy within the uncertainty of independent determinations ($\sim 0.5\%$). Transport properties obtained this way matched published quantities to within $\sim 30\%$. A finite-beam-size effect neglected in the predictive analysis limited the accuracies of these measurements. The analysis has since been extended to include this additional effect, the effect of electrostriction, and the effect of finite laser linewidth.

* Thermal or acoustic gratings often contribute to DFWM signals, especially at high densities. However, the contribution to the signal from these gratings is generally regarded as "interference" with the (desired) signals from the quantum-mechanical gratings. For this reason, the distinction is made that DFWM gratings are purely quantum-mechanical and LITA gratings are purely acoustic, i.e., LITA signals often interfere with DFWM signals.

5.2 Results of demonstration experiments

Experiments conducted to date use the setup schematized in Fig. 12. A pulsed narrowband dye laser pumped by a Q-switched, frequency-doubled Nd:YAG laser drives the acoustic waves. The dye laser emits about 40 mJ of light tuned between 587 nm and 592 nm in approximately 5 ns pulses. Three-millimeter-wide driver beams are formed from the dye laser emission by a 50% beamsplitter (*B.S.*) and a mirror *m*₁. The driver beams intersect at the focus of the 400 mm lens where they approximate finite plane waves about 200 μ m in diameter. The distance between the parallel beams, adjusted using micrometer translation stages, sets the beam-crossing angle. Three-dimensional phasematching (BOXCARS) geometries with crossing an-

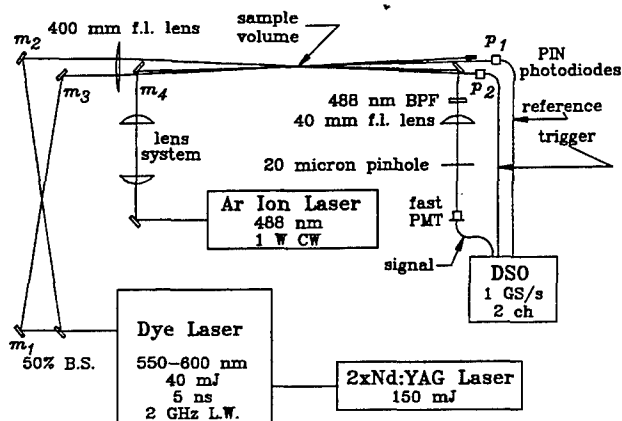


Fig. 12. Schematic diagram of LITA operation. For notation see text.

gles ranging from 1.0° to 2.3° were used in these experiments. The acoustic gratings are formed in the sample volume defined by the intersection of these beams. Detection of the driver beam pulse by a silicon PIN photodiode, *p*₁, triggers the acquisition of the LITA signal. Light from a 1W CW argon ion "source" laser operating at 488 nm scatters coherently off the acoustic gratings into the signal beam. A two-lens system adjusts the source beam diameter, which ranged from about 200 μ m to 2 mm. Phase-matching adjustments are made using a micrometer-driven translation stage under *m*₄. A silicon PIN photodiode, *p*₂, monitors the intensity of the source beam.

The signal beam detection system consists of a fast photomultiplier tube (PMT) with at least a 500 MHz signal bandwidth. Optical filters, including a 10 nm interference filter at 488 nm and a 40 mm lens/20 μ m spatial filter, prevent signal contamination. The LITA signal path-length to the detector is about 2.5 m. Data are recorded using a fast digital storage oscilloscope (DSO). This records typically 500-to-2000-sample time histories of signals from the PMT and *p*₂.

The first LITA experiments used laboratory air. Non-resonant electrostriction generated LITA signals with a signal-to-source beam intensity ratio, or reflectivity, of $\sim 10^{-8}$. An average over 256 shots yields the nonresonant data plotted as the dotted curve in Fig. 13. The modulation or "ringing" results from beating between Doppler-

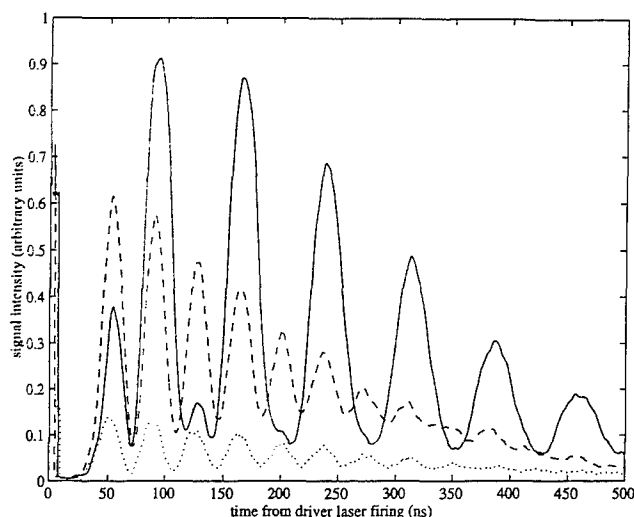


Fig. 13. LITA signals averaged over 256 shots in room air near a weak line of NO₂ which is present to about 50 ppb. Full line: Signal recorded near the peak of the spectral line. Dashed line: Resonantly enhanced signal near the spectral line. Dotted line: Non-resonant signal. By fitting these to the theoretical prediction, the speed of sound is obtained to $\pm 0.5\%$, and the bulk viscosity to $\pm 10\%$.

shifted light scattered off the laser-induced acoustic waves. This occurs at a frequency proportional to the sound speed and known geometrical and optical parameters. The frequency of the modulation (about 26 MHz) yields a sound speed accurate within the uncertainty of the knowledge of the laboratory sound speed ($\sim 0.5\%$). Electrostriction is resonantly enhanced near absorption lines. The resonantly-enhanced signal recorded near a weak line of NO₂ appears as a dashed curve in Fig. 13 for comparison. When the driver laser is tuned to an absorption line of the gas, molecules absorb light energy and release thermal energy through inelastic collisions, generating a thermal grating. If thermal gratings form rapidly, expansion of the gas emits acoustic waves. The signal recorded near the peak of the absorption line is the solid curve plotted in Fig. 13, which shows the difference in signature between electrostriction and thermalization signals. These signals are proportional to the real and imaginary parts of the complex gas susceptibility respectively, so that this provides a measurement of the complex susceptibility. The high sensitivity of LITA is demonstrated by this experiment, since the ambient air contained less than 50 ppb of NO₂ according to the Southern California Air Quality Management District.

Seeding the gas with NO₂ provided LITA signals that were several orders of magnitude stronger than the signals obtained from room air, with estimated reflectivities around 10^{-4} . A sample single-shot LITA signal is presented in Fig. 14 with the theoretical fit plotted as a dashed curve. The sound speed and transport coefficients used in the fit are published values for dry air. Clearly, the theoretical model gives an excellent prediction. Here, the thermalization process is treated as the superposition of two single-rate thermalizations: A fast ~ 10 ns process and a

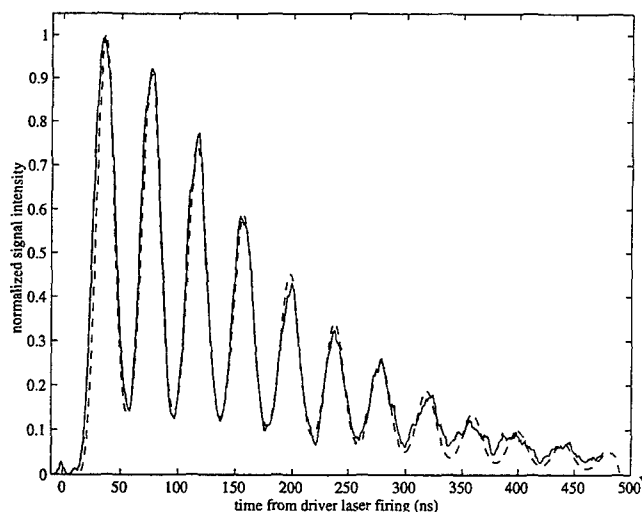


Fig. 14. Single-shot LITA record in room air seeded with NO_2 . Dashed curve shows theoretical prediction.

slow ~ 100 ns process. A better fit to the data could be obtained by adopting a more accurate thermalization model and source-beam-profile model in the analysis (a top-hat profile is assumed) and by including the effect of source-beam phase noise. These improvements are presently being incorporated into a computer fitting routine for LITA signals.

Information gained from these experiments has guided plans for future experiments. The accuracy of the simple analytical model and the relative strength of LITA signals have opened new paths of exploration: multiplex LITA and LITA velocimetry. Absolute species population and concentration measurements may be extracted from spectra obtained by LITA experiments in which the source laser is scanned across a band of species spectral lines. Such scanning techniques are common in laser diagnostics; however, they are not yet applicable to pulsed facilities such as T5. Alternatively, a broadband source laser can be used along with dispersion of the signal beam in a spectrometer to obtain single-shot "multiplex" spectra. Multiplexing using conventional FWM techniques has two drawbacks avoided by LITA:

- Analyzing multiplex spectra from "quantum-mechanical" grating techniques is complicated by quantum interferences, etc. Because LITA uses classical gratings, quantum mechanical complications are avoided. The simple analysis already experimentally verified extends readily to multiplex LITA.
- Much of the energy of the source laser falls between lines and is wasted, thus a high reflectivity is needed. Spectrometer losses compound this effect. LITA signals with reflectivities of 10^{-4} can be used in multiplex experiments studying even trace species. Furthermore, a long-pulse, broadband source laser such as a flashlamp-pumped dye laser may be used. These are available inexpensively with high pulse energies (> 1 J).

Multiplex experiments are currently under construction. A flashlamp-pumped dye laser with about 2.5 J per pulse is being modified for less mode structure. Laser mode structure interferes with all multiplex measurements. A high resolution echelle spectrometer with multiple inputs has been aligned and focused. Spectra fall on a computer-controlled precision CCD array. The spectrometer has a dynamic range of at least 2000:1 and a frequency resolution measured to be better than 3 GHz at 589 nm ($> 10^5:1$).

LITA velocimetry, by analogy with laser Doppler velocimetry (LDV), is also actively being pursued at GALCIT. In this technique, the Doppler shift of light scattered off convecting acoustic gratings is measured relative to an unshifted reference. This should make single-shot velocimetry possible in pulsed experiments with flow velocities from 50 to 3000+ m/s (estimation based on detector frequency response, beam size and duration effects etc.) For these experiments, a windowed test section with optical access from four sides has been designed and built. The test section is designed to be used in connection with a variety of test articles including a small combustion-driven shock tunnel capable of generating exit velocities of 3000 m/s in air and 7000 m/s in hydrogen. Alignment and testing will first be performed on a steady Mach 2 jet of air from the laboratory air supply.

LITA tests in T5 have been postponed until Spring 1995 to allow experimental development and exploration of the potential for LITA diagnostics. The risk reduction from this measured development and knowledge gained about the use of this promising diagnostic technique will enhance T5 LITA tests. In addition, timely development of generic LITA capabilities such as spectral multiplexing and velocimetry is in the broad interest of the combustion diagnostics community.

6. CONCLUSION

Results from four selected graduate research projects conducted in the T5 laboratory in the last two years have been presented. These have produced extensive new data that have widened the understanding of hypervelocity flows significantly. In addition a new laser diagnostic technique for sound speed and transport property measurement has been developed. The operation of T5 in a university environment has demonstrated that small-scale research of this style is very cost-effective in the advancement of hypervelocity gasdynamics. At the same time, the facility is large enough to make it suitable for some hypervelocity testing for industry.

Acknowledgements

This work was supported by AFOSR Grant F49610-92-J-0110 (Dr. L. Sakell) and AFOSR grant F49620-93-1-0338 (Dr. J. Tishkoff).

References

- Bakos R. J., J. Tamagno, O. Ryszka, M. V. Pulsonetti, W. Chinitz, and J. I. Erdos, 1992 "Hypersonic mixing and combustion studies in the Hypulse facility," *J. Propulsion and Power*, 8 900-906.

- Bélanger J. and H. G. Hornung 1994a "Transverse jet mixing and combustion experiments in the hypervelocity shock tunnel T5", AIAA paper 94-2517.
- Bélanger J. and H. G. Hornung 1994b "Numerical prediction and actual behavior of the free-piston shock tunnel T5", AIAA paper 94-2527.
- Candler G.V. 1988 "The computation of weakly ionized hypersonic flows in thermo-chemical nonequilibrium", Ph.D. Thesis, Stanford University.
- Cummings, E. B. 1992 "Techniques of Single-shot Thermometry by Degenerate Four-wave mixing (DFWM)", GALCIT Fluid Mechanics Report FM 92-2, Caltech, Pasadena, CA.
- Cummings, E. B. 1994 "Laser-induced Thermal Acoustics (LITA): Simple Accurate Gas Measurements", to be published in *Optics Letters*.
- Demetriades, A. 1977 "Laminar boundary layer stability measurements at Mach 7 including wall temperature effects", Rept. AFOSR-TR-77-1311, Air Force Office of Scientific Research, Washington, D. C.
- DiCristina, V. 1970 "Three-dimensional laminar boundary-layer transition on a sharp 8° cone at Mach 10", *AIAA Journal* 8, 852-856.
- Edney B.E. 1968a "Effects of Shock Impingement on the Heat Transfer Around Blunt Bodies". *AIAA Jour* 6 15-21.
- Edney B.E. 1968b "Anomalous heat transfer and pressure distributions on blunt bodies at hypersonic speeds in the presence of an impinging shock". FFA-115, The Aeronautical Research Institute of Sweden.
- Eitelberg G. 1992 "The high-enthalpy shock tunnel in Göttingen", AIAA Paper No. 92-3942, Nashville.
- Germain, P. 1993 "The boundary on a sharp cone in high enthalpy flow", Ph.D. thesis, California Institute of Technology.
- Germain P., Cummings E. and Hornung H. 1993 "Transition on a sharp cone at high enthalpy; new measurements in the shock tunnel T5 at GALCIT. AIAA 93-0343, Reno, Nevada.
- Germain P., and Hornung H. 1993 "The boundary on a sharp cone in high enthalpy flow", *Proc. 19th Int Symp on Shock Waves*, Marseille, Springer Verlag, to appear.
- Hornung, H. G. 1972 "Nonequilibrium dissociating nitrogen flows over spheres and circular cylinders", *J. Fluid Mech.*, 53, 149-176.
- Hornung, H. G. 1992 "Performance data of the new free-piston shock tunnel at GALCIT", AIAA 92-3943.
- Hornung H. G. 1993 "Hypervelocity flow simulation, needs, achievements and limitations", *Proceedings, 1st Pacific International Conference on Aerospace Science and Technology*, Tainan, Taiwan, pp. 1-10.
- Klopfer G.H. and Yee H.C. 1988 "Hypersonic shock-on-shock interaction on blunt cowl lips". AIAA Paper 88-0233.
- Lukasiewicz, J. 1973 "Experimental Methods of Hypersonics", Marcel Dekker.
- Roberts G. T., R. G. Morgan, and R. J. Stalker 1993 "Influence of the secondary diaphragm on flow quality in expansion tubes", *Proceedings of 19th International Symposium on Shock Waves*, Marseille, France, July, 1993, Springer-Verlag, to appear.
- Wen C.Y. and Hornung H.G. 1993 "Non-Equilibrium Recombination after a Curved Shock Wave," *Proceedings of 1st Pacific International Conference on Aerospace Science and Technology*, Vol. 2, 639-647, Tainan, Taiwan, Dec., 1993.
- Wen C.Y. and Hornung H.G. 1993 "Experiments on Hypervelocity Dissociating Flow over Spheres," *Proceedings of 19th International Symposium on Shock Waves*, Marseille, France, July, 1993, Springer-Verlag, to appear.
- Wen C.Y. "Hypervelocity flow over spheres", Ph.D. thesis, California Institute of Technology.
- Wieting A.R. and Holden M.S. 1989 "Experimental shock wave interference heating on a cylinder at Mach 6 and 8". *AIAA Jour.* 27 1557-1565.

Experimental Hypervelocity Flow Simulation, Needs, Achievements and Limitations.

Hans Hornung

Graduate Aeronautical Laboratories

California Institute of Technology

Pasadena, California 91125, USA

Abstract

The requirements for ground simulation of hypervelocity flows are set out on the basis of the similarity parameters of the problem. This, together with the thermodynamical properties of air, the consequent heat loads on the facility and large power requirements, leads to the two most successful devices, the reflected shock tunnel and the expansion tube. After a description of the operation and the thermodynamics of these devices, their essential limitations are explained. Scale effects of these limitations are discussed. On this basis the range over which they can be applied for flow simulation is delineated.

Keywords: Hypervelocity flow, ground simulation, simulation facilities, shock tunnel, expansion tube, dissociation.

1. Introduction

The term *hypervelocity* is used to distinguish those flows in which the velocity is so large that the conditions after the bow shock on a body are such as to cause the molecular components of the gas to dissociate. The fields of human endeavor where hypervelocity flows are of importance are those in which an object traverses the atmosphere of one of the planets of the solar system. Typically this could be associated with transport to or from space in man-made vehicles, but hypervelocity flows also occur naturally, e.g., when a meteorite enters a planetary atmosphere.

The term *hypersonic* flow is used to describe situations where the flow speed is large compared to the free-stream speed of sound. Such high-Mach-number flows can, of course, be generated by lowering the speed of sound far enough to keep the gas in the regime where it behaves as a perfect gas. In such *cold* hypersonic flows, the important dissociative and other real-gas effects of hypervelocity flows do not occur. In order to understand the intricacies of flows in which the chemistry of the gas is activated by the kinetic energy of the flow, it is necessary to simulate *hypervelocity* flows in the laboratory.

In the context of the earth's atmosphere the orbital velocity is 8 km/s, and the velocity at which the most severe heating problems arise is 6 km/s. In the frame of reference of the flying object, the ordered kinetic energy per unit mass of the free-stream gas is therefore 18 MJ/kg. At high enthalpy, the Mach number, which measures the square root of the ratio of the ordered kinetic energy of the flow to the thermal energy of the gas, is not so important as the ratio of the ordered kinetic energy measured in terms of the specific dissociation energy of the gas. There are usually several such characteristic chemical energies.

The characteristic specific energies relevant for air are

$$\begin{array}{ll} D_{N_2} = 33.6 \text{ MJ/kg} & E_{vN_2} = 0.992 \text{ MJ/kg} \\ D_{O_2} = 15.5 \text{ MJ/kg} & E_{vO_2} = 0.579 \text{ MJ/kg} \\ D_{NO} = 20.9 \text{ MJ/kg} & E_{vNO} = 0.751 \text{ MJ/kg} \end{array}$$

where the D 's and E_v 's are specific energies of dissociation and of vibration respectively. It is not possible to simulate the numerous idiosyncrasies of a particular gas by using another gas. The specific chemical energies have definite known values, and the duplication of the ratios of the ordered kinetic energy to them in a simulation implies that the actual flow speed has to be duplicated.

It follows that the reservoir enthalpy h_0 of the flow, which is approximately equal to $V^2/2$, where V is the flow speed, has to have the same value as in flight. If the flow is accelerated from a reservoir at rest, without adding energy to it during the expansion, the reservoir enthalpy corresponding to a flow speed of 6 km/s is 18 MJ/kg, which, at a reservoir pressure of 100 MPa, implies a temperature of nearly 9000 K in air.

The high pressure is necessary to ensure that the chemical reaction rates occur at the right speed for correct simulation of nonequilibrium effects. Smaller scale requires faster reaction for correct simulation. If the temperatures are right (as is ensured by correct flow speed) the reaction rates depend mainly on the density. Rates for binary reactions, like dissociation, are linear in density, those for three-body reactions, like recombination, are quadratic in density. Thus, all reactions can never be simulated correctly except at full scale. In many cases, three-body reactions are not important and, where they are, component testing or extrapolation is necessary.

Continuous flow facilities are ruled out by the high power requirements of typically a few GW. The high speed reduces the steady flow duration requirement to a few ms, however. A convenient way to accelerate, heat and compress a gas for a short time, is to pass a shock wave over it. Many types of high-enthalpy facilities therefore embody shocks as elements.

The problem of hypervelocity simulation is not limited to speeds of the order of 6 km/s, of course. Meteorites entering planetary atmospheres typically have a speed of 20-60 km/s, and proposals for man-made vehicles have considered speeds in the vicinity of 16 km/s. Such conditions involve very strong ionization of the gas and intense radiative heat loss from it. In the following discussion, such very high speeds will not be considered, and attention will be concentrated on the range 3-7 km/s. In this range, the requirements for simulation of hypervelocity flows and some of the methods by which the simulation has been achieved to date will be presented. The paper then closes with a discussion of the limitations and achieved conditions of the different types of facilities.

This paper is a descriptive account of the reasons for the forms that hypervelocity simulation facilities have taken. It is not a detailed account of the work that has been done in the field, and only a few representative publications will be cited. A very important book on the subject is Lukasiewicz's "Experimental Methods of Hypersonics". The interested reader should consult this volume on all the questions concerning this field.

In the present paper, the two most successful facility types for hypervelocity flow simulation, the reflected shock tunnel and the expansion tube will be given prominence.

2. Requirements for Ground Simulation

2.1 Similarity in Hypervelocity Flows

To simulate a hypervelocity flow at smaller scale, all the dimensionless parameters of the problem have to be reproduced. In steady hypervelocity flows any dimensionless dependent quantity Q , say, depends on dimensionless variables as follows:

$$Q = Q(M_\infty, Re, Pr, T_w/T_0, B_n, \alpha, \beta, E_i, R_j, Le_i, c_{oi}).$$

Here, M_∞ is the free stream Mach number, Re and Pr are Reynolds and Prandtl numbers, which, in this context, are best defined at conditions corresponding to the gas in equilibrium after a normal shock for which the upstream conditions are those of the free stream, T_w is a representative body surface temperature, T_0 is the temperature from which a gas would have to be expanded by a steady expansion to reach the free-stream conditions, B_n is a vector of length ratios defining the body geometry, α is the angle of attack, and β is the yaw angle. E_i is a vector of dimensionless numbers relating the specific formation enthalpies of the species to the specific kinetic energy of the free-stream gas, R_j is a vector relating the characteristic lengths associated with the chemical reactions to the characteristic length of the body, Le_i are the Lewis numbers giving the dimensionless species diffusion coefficients, and c_{oi} is a vector giving the dimensionless concentrations of the species in the free stream. Even this long list of variables is not complete, as the vibrational characteristics of the molecular species have been omitted.

Up to and including β in the above list, the variables are the same as in cold hypersonics, in which the remaining variables, which describe the thermodynamic and chemical properties of the gas, can be replaced completely by a single variable, the ratio of specific heats, which, for a perfect gas, is a constant. Clearly, the more complex thermodynamics and chemistry of the hypervelocity flow requires many more parameters to be duplicated in the scale experiments than perfect-gas cold hypersonics. For example, in air at a free-stream speed of 5 km/s, it is necessary to include at least 5 species and 8 reactions, so that, if all the geometrical parameters are exactly duplicated, there remain over 20 dimensionless variables to match. In fact, as has already been indicated in the introduction, it is not possible to simulate both binary and three-body reactions simultaneously (except at full scale) because of the difference in their dependence on the density.

In special cases, however, the problem may be considerably simplified. For example, if the gas is especially simple, such as in a single diatomic gas, there is only a single E and there are only two R 's. Only one of the R 's can be matched, and, e.g., in blunt body flows, it is best to match the binary dissociation reaction. With correct E , this automatically also causes Re , Le and Pr to be matched. Thus, the problem reduces to

$$Q = Q(M, T_w/T_0, E, R, c_\infty).$$

If the Mach number is sufficiently high, and the bow shock is not of interest in regions where it becomes very weak, the Mach-number-independence principle is effective, and the number of independent parameters is down to 4. This situation can be satisfactorily simulated.

Where such simplifications are not possible, it becomes necessary to divide the flow field up into particular regions and to simulate these separately. This is sometimes referred to as component testing. An example is the testing of engine combustors by connecting the inlet of the combustor directly to the exit of the facility nozzle, thus enabling testing at almost full size. Another example is the testing of the situation on the front of a body by placing only the nose shape into the test section, so that binary scaling and Mach-number independence apply.

2.2 Power Requirement

It is really quite amazing how much power is in a hypervelocity flow. For example, a wind tunnel with a cross-sectional area of 1 m², in which the flow speed is 7 km/s, and the density is 0.01 kg/m³ requires a power of 2 GW. This is a tenth of a percent of the power consumption of the USA. It also corresponds to an energy flux of 2 GW/m², or 46 times that at the surface of the sun. It is clear, that this kind of power can not be sustained for long times.

Fortunately, it only takes a very short time to set up a steady flow over a model at such high speeds. Opinions differ about the necessary test time. A reasonably conservative value is

$$\tau = 20 \frac{L}{V_\infty},$$

where L is the model length and V_∞ is the free-stream velocity. With this value, the test time requirement for the above facility comes out to approximately 3 ms, so that the energy requirement is only 10 MJ. This energy can be stored over a long time and released during a short test period.

The power requirement is thus one of the reasons why short-duration facilities are necessary for hypervelocity flow simulation. Another reason arises in the case of facilities that use a steady expansion to accelerate the flow from rest. In such facilities, the thermodynamic condition in the reservoir from which the gas is expanded is such that the specific enthalpy, h_0 , has to be 20 MJ/kg or so. In air, at a pressure of 100 MPa, this corresponds to a temperature of 9500 K or so. Hence, it is necessary to limit the time for which the materials containing the flow are exposed to these conditions. With the best materials available today, 3 ms is about the limit at the conditions quoted.

2.3 Instrumentation Requirements

This topic is one that deserves at least as much space as this whole paper, and it will not be possible to deal with it here, except for the purpose of pointing to its importance. Clearly, a test in a hypervelocity simulation facility is quite expensive. It is therefore most desirable to make as extensive a set of measurements as possible, each time such a test is performed. Unfortunately, the different forms of non-intrusive testing that exist at present require different degrees of expertise, which are seldom available at the same place as the test, because of the degree of sophistication that they often require.

Among the presently used routine measurement techniques, the following are available at all high-enthalpy test facilities:

1. Surface pressure measurement

2. Surface heat flux measurement
3. Schlieren and shadow photography
4. Interferometry

Techniques that are applied relatively rarely to hypervelocity flows, but are very important for them, are

1. Mass spectrometry
2. Spectroscopy
3. Laser-induced fluorescence
4. Raman spectroscopy

These methods are able to measure species concentrations and temperature, and would therefore provide extremely important data for the analysis of results from hypervelocity facilities. In the author's opinion, it is high time that major funding be directed to the juxtaposition of modern diagnostics and hypervelocity facilities. A good example of this is the policy at the HEG laboratory in Göttingen, Germany.

3. Hypervelocity Simulation Facilities

In this section the principles of operation of the most successful types of hypervelocity facilities are presented. The thermodynamical and chemical processes which the gas undergoes in the generation of the hypervelocity flow are given prominence in this, because they define and explain the most serious disadvantages of the facility types.

3.1 Reflected-Shock Tunnel

3.1.1 Configuration and Operation

By far the most used and most productive hypervelocity simulation facility is the reflected shock tunnel. Fig. 1 shows a schematic sketch and a wave diagram of the device. Initially, the driver region is filled with high-pressure gas and a diaphragm separates it from the shock tube, which is filled with the test gas at lower pressure. The shock tube is separated from a nozzle, attached to its other end by a weak diaphragm. The nozzle and test section, as well as the dump tank, are initially evacuated. The test section and dump tank are not shown in the figure.

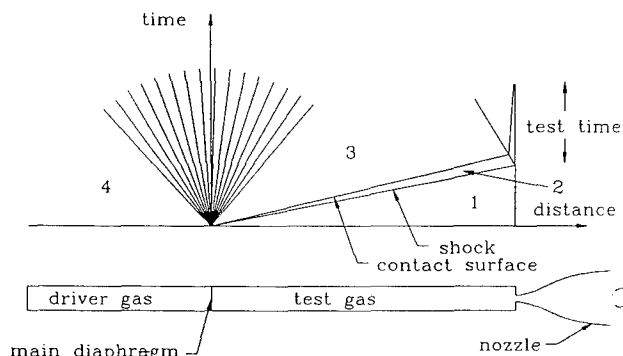


Fig. 1. Schematic sketch of reflected shock tunnel and wave diagram. The separation between the shock wave and contact surface is exaggerated to show it better

When the main diaphragm breaks, a shock wave propagates into the test gas, and an expansion wave propagates into the driver gas in such a way that the pressures and velocities in the region

between the shock wave and expansion wave are continuous across the interface between the two gases. These processes are shown in the wave diagram of Fig. 1. The initial state of the driver gas, in region 4 of the wave diagram, is processed by the expansion wave to the condition in region 3, and the initial state of the test gas, region 1, is processed by the shock wave to the condition in region 2. The states 2 and 3 are determined by the expansion wave and by the shock wave and the requirement that velocities and pressures must match across the boundary between 2 and 3. This may best be illustrated by a velocity-pressure diagram, shown in Fig. 2. The upper curve shows the locus of the states that can be reached from the initial condition of the driver gas via an expansion wave and the lower curve shows the states that can be reached from the initial state of the test gas via a shock wave. Their intersection represents the condition in regions 3 and 2, where pressures and velocities are matched. The solution thus corresponds to the intersection of the two curves in Fig. 2.

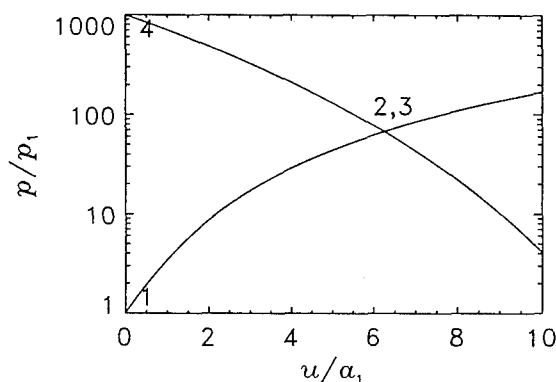


Fig. 2. Example of velocity-pressure diagram for a shock tube. The pressure p is normalized with the initial pressure of the test gas, p_1 , and the velocity u is normalized with the speed of sound in the test gas at condition 1, a_1 . In this example the gases are treated as perfect gases with specific heat ratios γ_1 and γ_4 of 7/5 and 5/3 respectively. Also, the ratio of the speeds of sound a_4/a_1 , the third parameter determining the solution, was chosen to be 5.

If a whole lot of such solutions are combined, the solutions can be shown parametrically in a diagram plotting the shock Mach number $M_s = V_s/a_1$ against the pressure ratio p_4/p_1 . This is done in Fig. 3.

In the reflected shock tunnel, the state of the test gas in region 2 is processed further by the shock wave reflected from the closed end of the shock tube. This heats and compresses the gas even more than has already been accomplished by the primary shock, but it also brings the test gas to rest again. The primary shock breaks the thin diaphragm between the shock tube and the nozzle, thus allowing the test gas to expand in a steady expansion through the nozzle.

It is important to operate the shock tunnel in such a way that the interaction between the reflected shock and the contact surface does not produce any further waves. When conditions have been chosen in such a way that this is the case, this is referred to as tailored-interface operation. The condition behind the reflected shock is then the reservoir condition of the nozzle flow, and is referred to by the subscript 0.

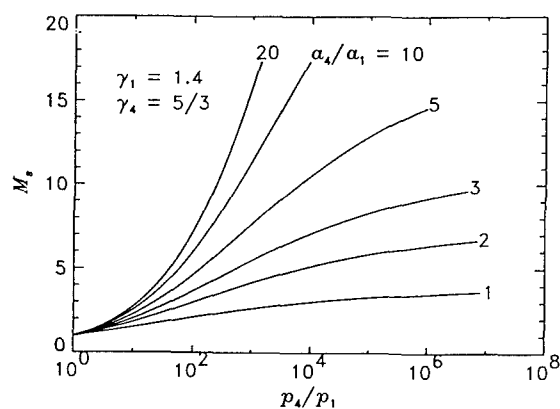


Fig. 3. The shock tube equation for monatomic driver gas and diatomic test gas, both treated as perfect gases. Note the strong dependence of the shock Mach number on the speed of sound ratio. Real-gas effects modify this diagram only slightly.

The nozzle expansion converts the thermal energy of the stationary reservoir gas into ordered kinetic energy. In doing so, the maximum flow velocity achievable is

$$V_{\infty} = \sqrt{2h_0},$$

where h_0 is the specific enthalpy of the reservoir condition. Since it is necessary to achieve speeds around 6 km/s, the reservoir specific enthalpy needs to be in the vicinity of 18 MJ/kg. In a reflected shock tunnel, a very good approximation is

$$h_0 = V_s^2.$$

It follows that the shock speed has to be about 4.3 km/s, which, in air, corresponds to $M_s = 12.5$. Referring to Fig. 3, we see that this value may not be reached with pressure ratios less than 2000 unless a_4/a_1 exceeds 8. Since the test gas speed of sound is virtually fixed by the fact that we want to use air in a laboratory at room temperature, the driver-gas sound speed has to be high.

3.1.2 Driver-Gas Conditions

Various ways have been used to increase a_4 . First, a light gas, either hydrogen or helium is used, and second, the driver gas is heated. Steady state heating is limited to about 800 K. This gives $a_4/a_1 = 4.8$ for helium driver gas and air test gas. Not only is

this too low, but it is also expensive and dangerous to contain high-pressure and high-temperature gas for an extended period. A second method is to heat the driver gas relatively quickly by combustion of a limited amount of hydrogen and oxygen mixed with the driver gas before the test. Mixtures in the proportions 14% hydrogen: 7% oxygen: 79% helium, give $a_4/a_1 \approx 7$.

While this is just about enough, another, more convenient technique is to compress the driver gas adiabatically with a heavy piston. This method has the advantage that the driver gas is hot only for a very short time, and that (as in the combustion-heated driver) the high pressure required is produced automatically. However, it also means that the driver is short, with a moving end wall, so that waves travelling between the main diaphragm station and the piston cause disturbances to the shock. With adiabatic compression, values of a_4/a_1 up to 12 are easily achievable, and the value of this parameter may be adjusted by using mixtures of helium and argon as driver gas. Monatomic gases require smaller compression ratios for the same pressure and temperature gains.

An example of a free piston driven reflected shock tunnel is shown in Fig. 4. This is the facility known as T5 at GALCIT. Similar machines exist at Canberra and Brisbane in Australia, at Göttingen in Germany, and at Tullahoma, USA.

The piston is accelerated in the compression tube by compressed air initially contained in the secondary air reservoir, thus compressing the driver gas until the diaphragm burst pressure (≈ 90 MPa) is reached. The piston speed at rupture has to be sufficiently high (≈ 170 m/s) to maintain almost constant pressure after diaphragm rupture for a short time (≈ 2 ms). Thus, the free-piston driver is a constant-pressure driver, in contrast to the constant-volume driver of the conventional shock tunnel. Fig. 5 shows a computed wave diagram for the processes in the compression and shock tubes of T5 after diaphragm rupture.

Another method of heating the driver gas is by a detonation wave travelling into a detonable mixture from the diaphragm end of the driver tube. This method has the advantage that the diaphragm may be much thinner, since it only needs to withstand the relatively low pressure before detonation. It also produces a long driver which should produce a more uniform shock propagation than the free-piston driver. A disadvantage is that, with hydrogen, the combustion produces water. The NO invariably produced in the reflected shock tunnel is likely to combine with this to form a very hostile environment for instrumentation and models.

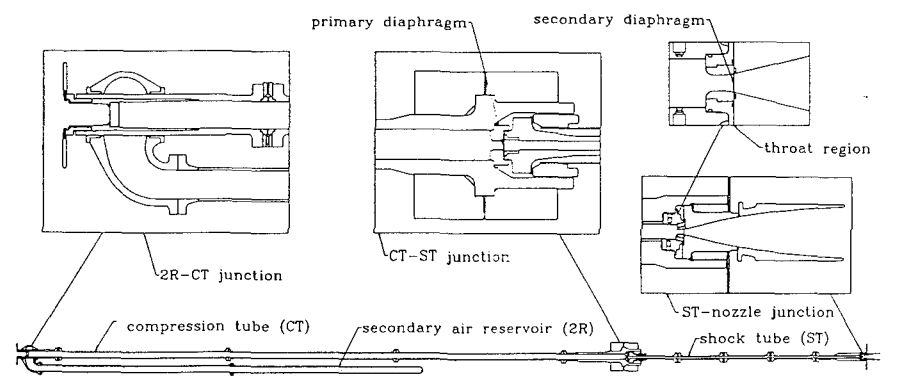


Fig. 4. Sectional view of the free-piston reflected shock tunnel T5 at GALCIT, with blow-ups of some of the parts. On the left is the 30 m long compression tube, joined to the 12 m shock tube and nozzle on the right. The test section and dump tank are not shown.

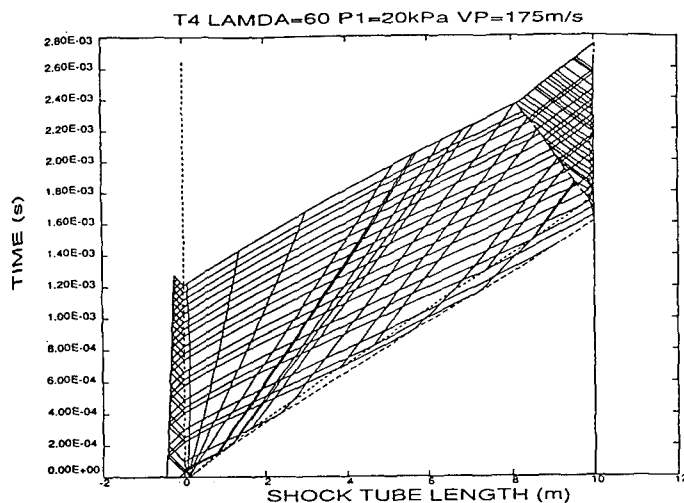


Fig. 5. Method of characteristics computation of the processes in the free-piston reflected shock tunnel. (after Hornung and Bélanger, AIAA 90-1377).

3.1.3 Reservoir Conditions

The shock wave propagating along the shock tube generates a boundary layer on the shock tube wall, which causes the shock to decelerate. This attenuation limits the length to diameter ratio of shock tubes to approximately 100. Since the test time is proportional to the shock tube length if there are no losses, the shock tube diameter effectively is one of the limiting factors on the test time.

As the shock speed needs to be approximately 4 km/s, the specific enthalpy after the shock is 8 MJ/kg. This corresponds to $h/R = 28,000$ K, where R is the specific gas constant for air at room temperature. The process undergone by the gas may be shown in a Mollier diagram, see Fig. 6. Here the initial state of the gas in the shock tube (state 1) is shown at $s/R = 24$ on the entropy axis as a square point, and the primary shock raises the state to the coordinates $[30, 24000 \text{ K}]$, (state 2) see dashed line. Pressure and temperature are now 18 MPa and 4000 K. At this condition, part of the oxygen is already dissociated and some NO has been formed.

The reflected shock then increases h and s further, to the point $[33.5, 60000 \text{ K}]$, (state 0), where pressure and temperature are 100 MPa and 8000 K, see continuation of dashed line. The steady nozzle expansion takes the gas down in enthalpy at constant entropy to the final point on the dashed line, which then represents the free stream conditions of the tunnel.

This is not quite correct, of course, because the nozzle flow does not usually proceed in thermodynamic equilibrium all the way down to this state. At some point in the nozzle flow, the density is no longer large enough to maintain the large number of three-body collisions between particles that is required for the atomic particles to continue recombining as the gas cools in the expansion. Such non-equilibrium states can not be represented in a Mollier diagram.

3.1.4 Nozzle-Flow Freezing

The recombination reactions stop fairly suddenly in the nozzle expansion, and because the composition of the gas remains constant after this point, the phenomenon is called nozzle-flow freezing. A

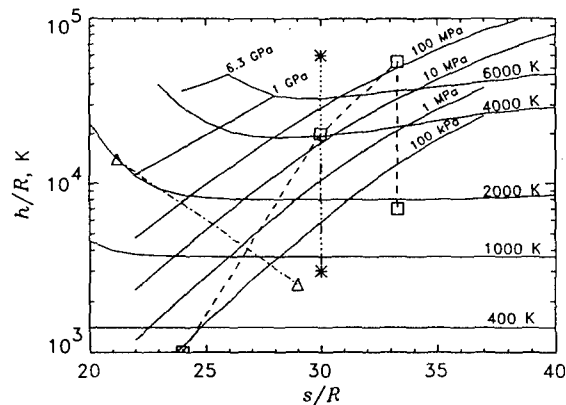


Fig. 6. Mollier diagram for equilibrium air, showing lines of constant pressure and temperature. An example of the processes in a reflected shock tunnel is shown by the dashed line. The lower asterisk represents the exit condition in an expansion tube that starts with the same shock tube conditions as in the reflected shock example. The upper asterisk represents the effective reservoir state of the expansion tube. The triangles show reservoir and exit condition of the facility proposed at Princeton.

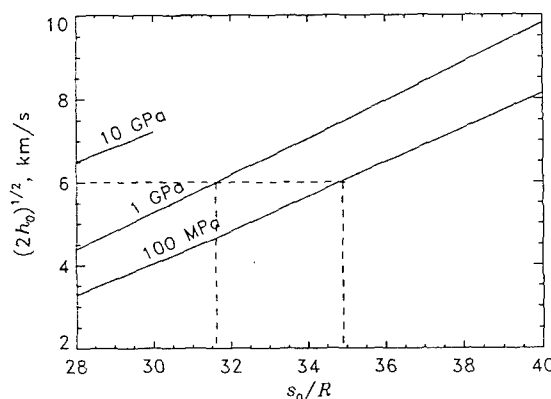
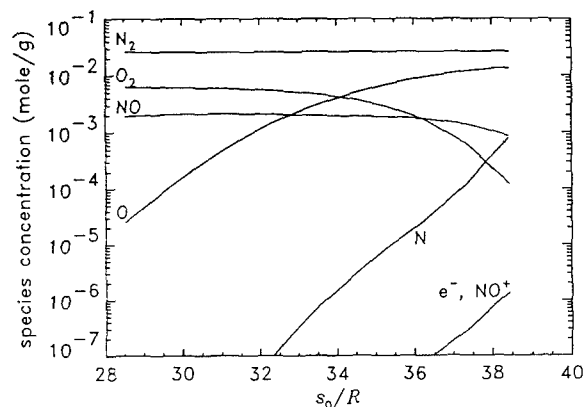


Fig. 7. TOP: For a given nozzle, the exit composition depends only on the dimensionless reservoir entropy. Example of T5 nozzle. BOTTOM: Mollier chart of the reservoir state showing lines of constant reservoir pressure. The specific reservoir enthalpy axis is plotted in the form of the maximum achievable velocity. This shows how, at a given flow speed, the specific reservoir entropy, and therefore the exit composition, depend on the reservoir pressure.

well-known feature of freezing is that, for a given nozzle, the composition of the frozen gas depends only on the reservoir specific entropy s_0 , and not on the reservoir specific enthalpy h_0 or reservoir pressure p_0 . In the example of one of the nozzles of T5, the upper part of Fig. 7 shows the frozen composition plotted against s_0/R . As may be seen, the concentration of atomic oxygen in the flow increases as s_0/R increases, until at 34 the number densities of O_2 and O are equal. Also, the fairly high concentrations of NO are unavoidable.

The lower part of Fig. 7 shows a Mollier chart of the reservoir state. Here the enthalpy coordinate has been distorted to convert it into the velocity achievable from a given reservoir state. This is because it shows the relation between the composition of the free-stream gas and the reservoir pressure. For example, to achieve 6 km/s, a reservoir pressure of 100 MPa produces the composition corresponding to $s_0/R = 34.9$, while a reservoir pressure of 1 GPa at the same enthalpy would give the lower atomic oxygen concentration corresponding to $s_0/R = 31.6$. Fig. 7 also shows that the NO concentration remains constant as s_0 is decreased. This is unavoidable with high-enthalpy reflected shock tunnels.

3.2 Expansion Tube

3.2.1 Configuration and Operation

Some of the essential limitations of the reflected shock tunnel are removed at the cost of new limitations by using an expansion tube. The expansion tube, like the reflected shock tunnel, first processes the test gas by propagating a shock wave through it, thus compressing, heating and accelerating it. The test gas is then not brought to rest as in a reflected shock tunnel, but accelerated further by an *unsteady* expansion. This is achieved by the arrangement shown in Fig. 8 also showing the wave diagram describing its operation.

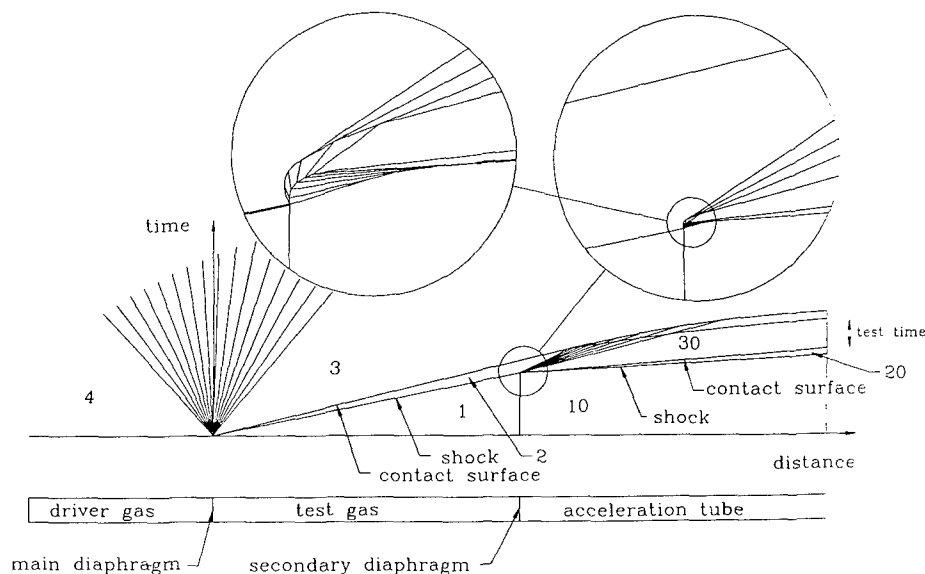


Fig. 8. Schematic sketch and wave diagram of an expansion tube. The detail in the vicinity of the rupture of the secondary diaphragm is shown in two enlarged insets. The diaphragm is accelerated to the contact surface speed over a finite opening time. This causes a reflected shock that is accelerated by the left running expansion wave transmitted from the diaphragm. Clearly, diaphragm opening time reduces the available test time.

In the expansion tube, a long acceleration tube usually of the same diameter as the shock tube is initially separated from the shock tube's downstream end by a thin secondary diaphragm. The pressures might have the initial values: 100 MPa, 100 kPa, 200 Pa in the driver, shock tube and acceleration tube respectively.

When the shock strikes the secondary diaphragm, it breaks, and the test gas acts as the driver for the shock propagating into the acceleration tube gas. The regions 10, 20 and 30 thus are analogous regions to those labelled 1, 2 and 3 in the shock tube. The processes undergone by the test gas are: 1-2 (shock), 2-3 (unsteady expansion). The conditions in the test gas after these processes may again be calculated by the shock tube equation. The result of such a calculation is shown graphically in Fig. 9. The test time is limited by the acceleration-gas test-gas contact surface, and by the leading edge of the reflection of the unsteady expansion from the driver-gas test-gas contact surface.

3.2.2 Effective Reservoir State

The expansion tube's thermodynamics may now be compared with that of the reflected shock tunnel in Fig. 6, where the lower asterisk marks the test condition of the expansion tube. The two first square symbols representing state 1 and state 2 are shared by the shock tunnel and expansion tube. The expansion tube takes the gas to a maximum temperature of 4000 K in this example, so that the atomic oxygen and NO concentrations may be kept much lower than in the shock tunnel.

At the same time, the effective specific reservoir enthalpy is more than twice the static enthalpy in region 2, since it is possible to gain total enthalpy in an unsteady expansion. This is therefore higher than after the reflected shock. To show the effective reservoir state of the expansion tube in Fig. 6 a second asterisk is plotted there, connected to state 2 with a dotted line to indicate that the gas never reaches this high enthalpy and pressure. The

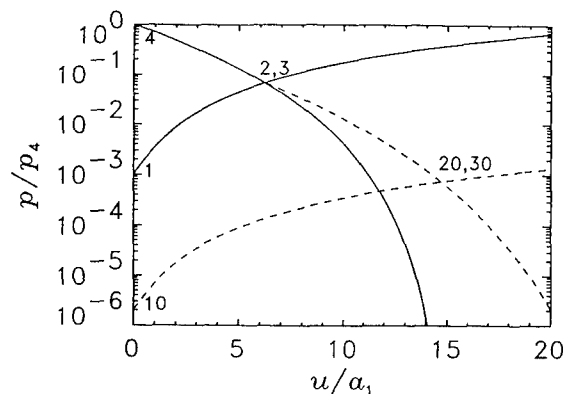


Fig. 9. Velocity-pressure plot of the processes in an expansion tube. The full lines give the solution for region 2 and the dashed lines, representing the locus of conditions achievable via a shock wave from condition 10, and the conditions achievable via an unsteady expansion from condition 2, give the solution for the test condition, 20. In this example, the driver gas is monatomic and the test and acceleration gases are diatomic. All are considered perfect gases.

lower entropy of the expansion tube causes the effective reservoir pressure to be enormous. In our example, it is around 2 GPa.

The static enthalpy h and static pressure p of the gas can remain low in the expansion tube, because the gas is not brought to rest after reaching state 2. This may be illustrated schematically in the case of h by the diagrams in Fig. 10

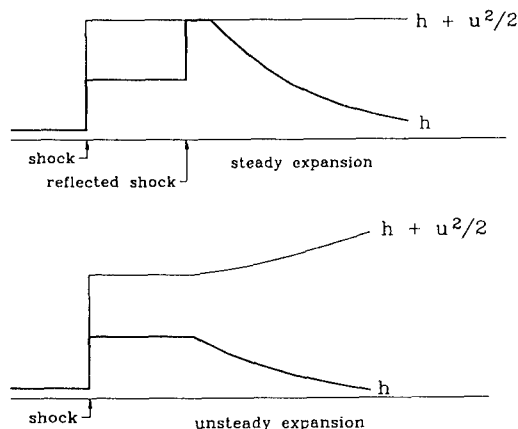


Fig. 10. Timelines of the static and effective reservoir specific enthalpy during the processes in a reflected shock tunnel (TOP), and in an expansion tube (BOTTOM). The expansion tube avoids the high value of h experienced by the test gas in the reflected shock tunnel and yet achieves even higher h_0 .

3.2.3 Free Stream Conditions

The test gas composition is practically that of state 2, because the density drops so quickly in the unsteady expansion that recombination of the atomic oxygen is not possible. Therefore it is best to operate the expansion tube with as low a value of T_2 as possible from this point of view.

If the expansion is taken to the same free stream pressure as in the reflected shock tunnel, see Fig. 6, the free stream temperature is seen to be much lower. This permits higher Mach number to be reached at the same h_0 .

3.3 Other Types of Facilities

A number of other types of facilities are in operation or are being considered. Among these the hypervelocity range is the most important. It employs a two-stage light gas gun to launch a model at the required speed into stationary gas in a long tube. This device is clearly much more expensive to operate than one in which the model is stationary. The model and instrumentation are also much more expensive, and it is difficult to test models that have high lift. However, the hypervelocity range is the only facility type in which good measurements of far wakes of bodies can be obtained.

There have been a number of other schemes, involving magneto-hydrodynamic accelerators or arc heaters. A relatively new idea being pursued at Princeton, is the optically heated continuous flow facility. This scheme aims to keep the gas below 2000 K in order to prevent the formation of NO. In Fig. 6, the process is shown by the chain-dotted line terminated by triangles. The gas is first compressed to a pressure of 1 GPa or more, and 2000 K. This makes use of the van der Waals effect that the isotherms curve up at low entropy, giving higher enthalpy. In the example shown in Fig. 6, the gas has approximately 20% of the necessary total enthalpy in this condition. The remainder of the enthalpy is added during a steady expansion by absorption of light. Success depends critically on whether the enormous power levels required (≈ 1 GW in the form of light) can be achieved and can be absorbed by the gas without causing non-equilibrium processes to produce atomic oxygen. In the author's opinion, these are very substantial questions.

4. Limitations of the Main Facility Types

All the different facility types have limitations that constrain them to be operated in regimes where conditions are acceptable and where they work. To some extent, the regimes covered by different facilities complement each other. As in the previous sections the following discussion will concentrate on the two most important types, the reflected shock tunnel and the expansion tube.

4.1 Reflected Shock Tunnel

Part of the following discussion is concerned with the effects of increasing the size of a reflected shock tunnel. In these considerations it is assumed that the ratios of lengths remain constant. In particular, the length to diameter ratio of the shock tube, which is limited by friction and heat loss at the shock tube wall, is considered to have the same value. The best value for this ratio turns out to be close to 100.

There are four main limitations to the regime that can be covered by the reflected shock tunnel:

1. The departure of the composition of the free-stream gas from that of air.
2. The fact that the test gas is brought to rest before it is accelerated again produces very high temperatures at high pressures which causes a containment problem.
3. The test time is limited by the size, by driver-gas contamination and by the containment limitation.
4. The strength of the facility limits the pressure.

4.1.1 Free-Stream Freezing

It is clear from Fig. 7 that it is not possible to produce a free-stream gas composition that is free of NO, unless the reservoir temperature is kept below 2000 K. This is therefore a hard limitation of the device if one is interested in real-gas effects in air. To set an arbitrary limit, choose the case when the molecular oxygen concentration is half of that in air. Fig. 7 may now be used to translate this limit into a line in $h_0 - p_0$ space. The top part of the figure shows that this limit is reached at $s_0/R = 35.2$. The bottom part of the figure shows how p_0 and h_0 are related along this value of s_0 . This relation is plotted in Fig. 11. As may be seen, an increase of p_0 moves the limit to significantly higher values of h_0 .

This limitation may, strictly speaking, not be represented by a single curve in $h_0 - p_0$ space, because it is dependent on the size of the facility. However, since the recombination rate in the nozzle flow is proportional to the square of the pressure (other variables being the same) quadrupling the size of the facility would only lower the line by a factor of 2 in pressure.

4.1.2 Nozzle-Throat Melting

The high temperatures and pressures seen by the containing material in a reflected shock tunnel lead to the limitation that materials can not be found that will contain the conditions for the duration of the test without melting. From experiments in T5, a copper throat is found to melt at $p_0 = 100$ MPa, $h_0 = 20$ MJ/kg, when the exposure to high heat flux lasts approximately 3 ms. From

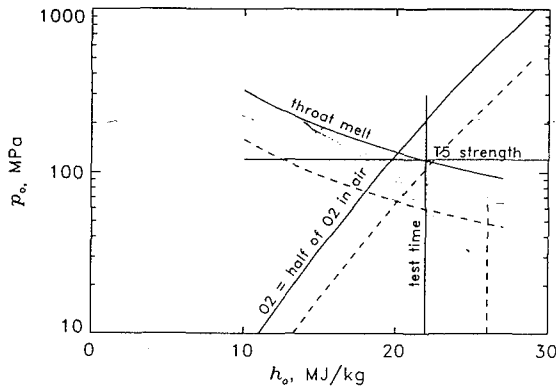


Fig. 11. Limitations on the reservoir pressure and specific enthalpy of reflected shock tunnels. The full line represents a facility of the size of T5. The dashed lines are for a facility scaled up by a factor of 4.

this result, and from the properties of copper, the heat flux to the wall may be estimated using one-dimensional unsteady heat conduction theory to be ≈ 2 GW/m². This agrees roughly with semiempirical formulas for throat heating.

Starting from this experimental point, adjusting it for the difference in the properties of copper from those of the best material found so far (tungsten-copper alloy), and extending it according to approximate formulas, the curve shown in Fig. 11 results. The basis of the approximation of this extension is that the convective heat flux is proportional to the density and the cube of the velocity, and that the exposure time is inversely proportional to the velocity.

It is important again to realize that this curve also depends on the facility size. The surface temperature reached under a given transient heat load is proportional to the square root of the exposure time (other variables being the same). The exposure time is proportional to the test time, which scales directly as the facility size (as does the *requirement* for test time). Since the heat flux is approximately proportional to pressure, quadrupling the size of the facility thus lowers the throat melt limit by a factor of 2 in p_0 , which therefore kills half of the improvement of the upscale.

4.1.3 Driver-Gas Contamination

The time interval between the arrival of the shock and the arrival of the contact surface at the right-hand end of the shock tube (see Fig. 1) is the most important factor in determining the test time. The test time can not simply be calculated from one-dimensional computations such as the one shown in Fig. 5, however, because the contact surface is in reality an extended region, and the complex interaction between the reflected shock and the boundary layer on the shock tube wall causes significantly earlier arrival of the driver gas at the nozzle throat.

At a given h_0 , the time interval between the arrival of the shock and the contact surface is directly proportional to the size of the facility (other variables being the same). As h_0 is increased, however, from the condition where the gas in region 2 is a perfect diatomic gas to where it is partially dissociated, this time interval changes down by almost a factor of 2. The speed with which the gas is drained from the reservoir through the throat into the nozzle increases as the square root of h_0 . Fortunately, the test time requirement also decreases as the square root of h_0 . However, the growth of the contact surface and the shock boundary layer interaction become more severe with increase of h_0 . As h_0 is increased, there comes a point when the test time is no longer sufficient. Though only very sparse information is available on this limit, it may be placed roughly at 22 MJ/kg for the case of T5, and this is essentially independent of p_0 .

Other things being equal, a scale increase increases the test time more than linearly, because the relative importance of the wall effects decreases. The test time *requirement* increases linearly with scale. The test time limit may therefore be expected to be moved to slightly higher h_0 in a larger facility.

4.1.4 Strength, Scale Effects

Clearly, the strength of the facility merely limits the pressure at which it can be operated, and may be represented by a line at constant p_0 .

To illustrate the effect of scaling up a facility from the size of T5 by a factor of 4, Fig. 11 also shows the displaced limits for the larger machine as dashed lines. This makes it clear that an increase of size makes strength relatively unimportant, since the throat-melt limit makes it impossible to operate at $p_0 > 70$ MPa, if $h_0 > 15$ MJ/kg in the facility scaled up by a factor of 4. As regards the throat-melt, test-time and strength limits, T5 appears to be close to the optimum scale. This was fortuitous, since the scale and strength were determined by other constraints.

4.1.5 Performance

In the region of $h_0 - p_0$ space within the above limitations, reflected shock tunnels can cover the space practically completely. In the

case of the free-piston device, this can be achieved with tailored interface operation, because of the flexibility of the speed of sound ratio a_4/a_1 of this device.

As an example, Fig. 12 shows two reservoir pressure traces obtained in T5. These are representative of the quality achievable over the range $20 \text{ MPa} < p_0 < 100 \text{ MPa}$, $5 \text{ MJ/kg} < h_0 < 22 \text{ MJ/kg}$.

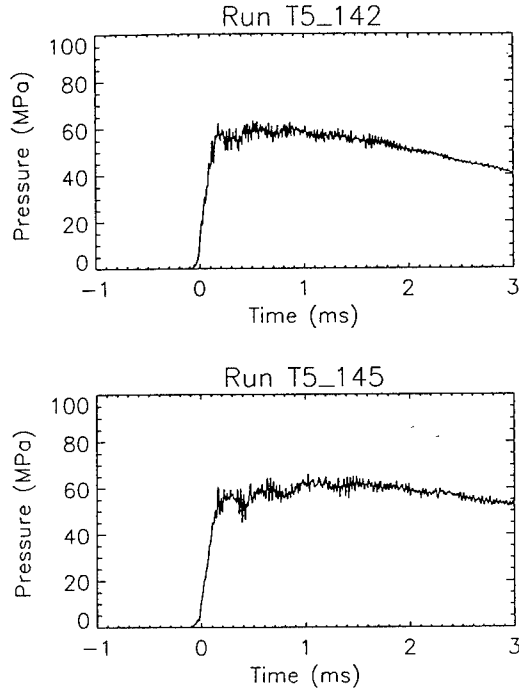


Fig. 12. Nozzle reservoir pressure traces of two runs of T5 at 22 (TOP) and 11 MJ/kg (BOTTOM).

4.2 Expansion Tube

As was pointed out in the description of the expansion tube, this facility type has the advantage that the material is exposed only to a fraction of the effective total pressure and only to a fraction of the total enthalpy. The stresses and heat loads are therefore not a serious limitation. Referring to Fig. 9 and Fig. 6 it becomes clear that for a given state 2, the effective values of p_0 and h_0 depend on the pressure p_{20} to which the flow is expanded in the unsteady expansion. It is therefore not meaningful to relate the extreme heating condition to the $h_0 - p_0$ space on this basis.

In the expansion tube a far more important concern is the short test time and the small test flow size. Consider for example a shock tube diameter of 100 mm. In the reflected shock tunnel, this provides a good flow for a nozzle exit diameter of typically 400 mm and a test duration of 1 ms at 18 MJ/kg. In the expansion tube, the same shock tube, driving an acceleration tube of the same diameter and 10 m length would produce a test flow of 100 mm exit diameter and 170 μs duration.

Fortunately, the size of the facility can be increased, since the penalty for size that plagues the reflected shock tunnel (melt limit) does not exist here. However, the test time limit remains, since the test time, which increases linearly with the size, only matches the increased test time requirement, which also increases linearly with size, unless the facility is deliberately made much larger than the models to be tested.

The friction losses in the acceleration tube set a limit on the length to diameter ratio. A reasonable maximum value is about 120. It turns out that a good shock tube length is then about 50 diameters. A rule of thumb for the optimum test time of an expansion tube is the time interval between the arrival of the primary shock and the arrival of the shock tube contact surface at the end of the shock tube. This time is given approximately by

$$\tau \approx 10 \frac{d}{\sqrt{h_0}},$$

where d is the shock tube diameter. This is smaller than the test time requirement of $20L/V_\infty$, given in section 2.2, by a factor of 1.4 if the model size L is taken to be the tube diameter d . The model therefore has to be smaller than the largest model that could be tested in the facility if size were the only constraint.

Any attempts to expand the diameter of the expansion tube at the downstream end are therefore futile, since the model size is limited by the available test time, and not by the tube diameter. (This verdict may be relaxed if the flow studied is such that less test time than $20V_\infty/L$ is required.)

The most important problem in expansion tube operation is therefore the preservation of as much as possible of the test time. An obvious factor reducing the test time is the opening time of the secondary diaphragm, which is disregarded in the ideal expansion tube calculations above. In order to show the effect of finite diaphragm opening time, Fig. 8 shows as blown up insets two successive enlargements of a portion of the wave diagram. In the largest of these, the diaphragm is shown to accelerate from rest over a finite time to become the contact surface between the acceleration and test gas. The diaphragm thus causes the incident shock to be reflected. As the diaphragm accelerates, expansion waves are transmitted to the reflected shock, weakening it and eventually causing it to become the right edge of the unsteady expansion. On the acceleration tube side of the diaphragm, compression waves are transmitted to the right, which focus to form the acceleration tube shock. The time it takes to accelerate the diaphragm clearly reduces the test time.

The reduction in test time is roughly equal to the diaphragm opening time. This is given approximately by

$$t_D \approx \sqrt{\frac{\rho \theta d}{p_2}},$$

where ρ is the density of the diaphragm material, θ is the diaphragm thickness and p_2 is the pressure in state 2. For a mylar diaphragm that is just strong enough to contain $p_1 = 100 \text{ kPa}$, and a diameter of 300 mm, this gives an opening time of approximately 70 μs . On the basis of the above rule of thumb, the test time becomes 0.7 ms at 18 MJ/kg, so that the diaphragm opening time reduces the available test time by about 10%.

All of these considerations assume the flow to be one-dimensional, and serious consequences for the test time may be expected to result also from the wall effects on the structure of the two contact surfaces, and the three-dimensionality of the diaphragm rupture.

The composition of the test gas was assumed to be that of state 2 above. This is a little pessimistic, because some recombination will occur in the unsteady expansion during the later part of the test duration, where the gas has taken a longer time to traverse the expansion wave. This will therefore cause the composition to

vary during the test time from an initial condition corresponding to that of state 2 to a final condition in which the atomic oxygen concentration, and to a lesser extent the NO concentration, are reduced slightly. The composition limit is almost independent of p_0 . The molecular oxygen will be reduced to half the value in air at $h_0 \simeq 22$ MJ/kg.

Summarizing the limitations of the expansion tube, the emphasis has to be on the test time limit. Since the diaphragm opening time is independent of h_0 , there comes a point where the enthalpy is limited by the test time. In the author's opinion, this limit is at 30 MJ/kg. The upper limit on p_0 is unimportant, since values in the GPa range are easily achievable.

4.2.1 Performance

To date, the largest expansion tube is one operated at the General Applied Sciences Laboratory in New York by a team headed by Dr. John Erdos. This has a shock tube (and acceleration tube) diameter of 150 mm. At present it has a cold helium driver, so that the enthalpy at which it can be run is limited to approximately 12 MJ/kg. A modification to equip the facility with a free-piston driver is being considered at present. This would extend the range to approximately 30 MJ/kg. The effective reservoir pressure is very high. In the GASL facility, values of up to 400 MPa have been achieved.

5. Concluding Remarks

The thermodynamics, gasdynamics and scaling laws of hypervelocity flows, the power requirements, and the properties of containing materials, were shown to lead to the two main hypervelocity flow simulation facility types: The reflected shock tunnel and the expansion tube. The simplest forms of such devices were described, giving the logic that leads to them, and a comparison of their ranges of applicability. This was done with regard only to their main features, and many subtle points of their operation had to be omitted.

The hard limitations of the reflected shock tunnel constrain this device to be restricted to specific reservoir enthalpies below 22 MJ/kg and reservoir pressures below 90-200 MPa (depending on the enthalpy in the range 25-12 MJ/kg) at the size of the presently operating facility T5. Increase of size carries severe pressure penalties. The expansion tube's most severe restriction is the short test time. This is critically constrained by the behavior of the contact surface and the opening time of the secondary diaphragm. However, there appear to be no penalties for scale increase, and the reservoir pressure obtainable is extremely high. The upper limit for the specific reservoir enthalpy is approximately 30 MJ/kg on the basis of the free stream dissociation and test time constraints.

References

- Bakos R. J., J. Tamagno, O. Ryszkalla, M. V. Pulsonetti, W. Chinitz, and J. I. Erdos, 1992 "Hypersonic mixing and combustion studies in the Hypulse facility," *J. Propulsion and Power*, 8 900-906.
- Hornung, H. G. 1992 Performance data of the new free-piston shock tunnel at GALCIT, AIAA 92-3943.
- Lukasiewicz, J. 1973 "Experimental Methods of Hypersonics", Marcel Dekker, Inc. New York.

RECENT RESULTS FROM HYPERVELOCITY RESEARCH IN T5

H.G. Hornung¹, E.B. Cummings², P. Germain³, S.R. Sanderson², B. Sturtevant⁴ and C.-Y. Wen⁵
Graduate Aeronautical Laboratories, California Institute of Technology

Abstract

Results are presented from a selection of the graduate research projects that were carried out in the T5 hypervelocity shock tunnel laboratory during the last two years. The projects presented are:

1. Hypervelocity flow over spheres. Differential interferometry and heat transfer measurements are used in air, nitrogen, and carbon dioxide flows to test numerical results and a new stand-off distance correlation.
2. High-enthalpy real-gas effects in boundary layer transition on a slender cone. Heat transfer measurements and resonantly enhanced flow visualization provide new data on the effect of reservoir enthalpy on transition. The effect is quite strongly stabilizing. The visualization shows the structure of high-enthalpy transitional and turbulent boundary layers.
3. Real-gas effects in shock-on-shock interaction. Flow visualization indicates that the range of shock impingement points for which enhanced heating occurs is increased by high-enthalpy real-gas effects. Some flow features are changed qualitatively.
4. A new diagnostics technique: Laser-induced thermal acoustics. This method provides accurate point measurement of the speed of sound, bulk viscosity, and susceptibility of a gas.

The experience with T5 over the first 700 runs shows that its operation in a university environment is a cost-effective way of improving the understanding of phenomena in hypervelocity gasdynamics.

1. INTRODUCTION

At the last AIAA Ground Testing Meeting, we presented the performance characteristics of the free-piston hypervelocity shock tunnel T5, the problems encountered during the shake-down period, its limitations, and some data on flow duration and repeatability, see Hornung (1992).

Further experience in operating T5 has led us to make a study of the limitations of high-enthalpy facilities, see Hornung (1993). One of the diagrams of this study is reproduced here to illustrate the relation of the two main types of hypervelocity facilities, the expansion tube and the reflected-shock tunnel, relative to each other. This is done in a Mollier chart, see Fig. 1.

The square symbols are the actual thermodynamic states reached by the test gas in an example of the free-piston shock tunnel operation. To achieve a reservoir specific enthalpy of 16 MJ/kg, say, the shock speed needs to be approximately 4 km/s. Thus, the specific enthalpy after the shock is 8 MJ/kg. This corresponds to $h/R = 28,000$ K, where R is the specific gas constant for air at room temperature. If the initial state of the gas in the shock tube is $s/R = 24$, and $T = 300$ K, the primary shock takes the gas to the state $s/R = 30$, $h/R = 24000$ K. These two points are connected schematically by a straight dashed line in the diagram. The test gas is then brought to rest by the reflected shock, which raises the entropy and enthalpy further, to $[33.5, 60000$ K], again shown by a square symbol and schematic dashed line. From this hot state, the gas is re-accelerated by a steady expansion, initially at constant entropy while the expansion proceeds at equilibrium, and with a slight entropy increase toward the end of the expansion. For simplicity, the expansion is drawn at constant entropy.

The expansion tube shares the first process with the shock tunnel. However, instead of then stopping the gas by a reflected shock, and converting the kinetic energy to thermal energy, and then re-accelerating it in a steady expansion, it processes the already moving gas by an unsteady expansion to the desired free-stream state. It therefore always retains some of its energy in kinetic energy form, so that the gas never sees the high temperature encountered in reflected-shock tunnels. At the same time, the entropy

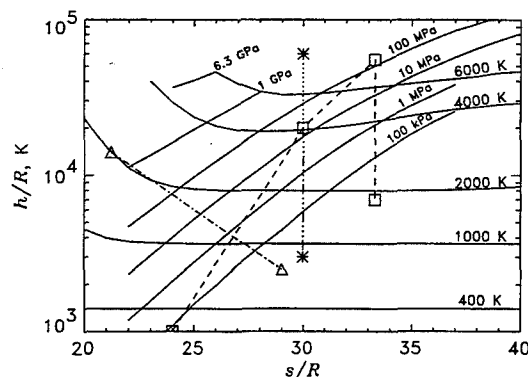


Fig. 1. Mollier diagram for equilibrium air, showing lines of constant pressure and temperature. An example of the processes in a reflected-shock tunnel is shown by the dashed line and square symbols. The lower asterisk represents the exit condition in an expansion tube that starts with the same shock tube conditions as in the reflected-shock example. The upper asterisk represents the effective reservoir state of the expansion tube. The triangles show reservoir and exit condition of the direct energy addition facility proposed at Princeton.

¹ Kelly Johnson Professor of Aeronautics, Director of GALCIT, Member, AIAA

² Graduate Research Assistant

³ Research Associate, NRC, Canada

⁴ Professor of Aeronautics, Member, AIAA

⁵ Student member, AIAA

remains considerably lower, so that the effective reservoir pressure is extremely high. The effective reservoir state of the expansion tube is shown as the top asterisk in the Mollier chart. This high pressure (>1 GPa) is also never seen by the facility, since the flow is never stopped.

The expansion tube has the important advantages that the material of the machine is not exposed to the extreme temperatures and pressures encountered in the shock tunnel, and that the test gas is not as highly dissociated, and therefore has less atomic oxygen in the free stream gas. These advantages are obtained at the expense of considerably smaller test time and size for a given shock tube diameter. The smaller test time is also bugged by uncertainties about the secondary diaphragm behavior, some of which have been studied by Roberts et al. (1993). To date, the largest expansion tube is one operated at the General Applied Sciences Laboratory in New York by a team headed by Dr. John Erdos. This has a shock tube (and test section) diameter of 150 mm. At present it has a cold helium driver, so that the enthalpy at which it can be run is limited to approximately 15 MJ/kg, see, e.g., Bakos et al. (1992). The largest free-piston reflected-shock tunnel is being operated by the group under Dr. Georg Eitelberg in the DLR, Göttingen, Germany, with a shock tube diameter of 150 mm, and a test section diameter of 800 mm.

(As a matter of interest, Fig. 1 also shows the approximate Mollier path of a proposed direct energy addition facility, which has the aim of producing a free stream completely free of atomic oxygen and NO, by avoiding temperatures higher than 2000 K.)

The relatively more rapid development of the reflected-shock tunnel is due in part to the perseverance in the field of hypersonics of groups like Calspan, Buffalo (Holden), and Australian National University (Stalker) during the 1970's and early 1980's, who developed and operated reflected-shock tunnels. T5 is very much a derivative of the development of the free-piston driven devices developed by Stalker in Australia. The Stalker group now operates free-piston reflected-shock tunnels and expansion tubes at Queensland University, see other presentations at this meeting.

During the last two years, T5 has been used in some 400 runs, mostly for graduate research, but also for a few proprietary tests for the European Space Agency, Hitachi, and Mitsubishi Heavy Industries. In this paper, we report on selected results from the graduate research projects on

1. Hypervelocity flow over spheres,
2. High-enthalpy real-gas effects in boundary layer transition on a slender cone,
3. Real-gas effects in shock-on-shock interaction,
4. A new diagnostics technique: Laser-induced thermal acoustics.

Two other projects on high-speed hydrogen injection and on the computation of the gas-dynamical processes in free-piston shock tunnels are being presented in separate papers at this conference, see Bélanger and Hornung (1994a&b).

2. HYPERVELOCITY FLOW OVER SPHERES

An extensive series of experiments on flow over spheres has been completed. This involved nitrogen, air and carbon dioxide flows covering the full range of enthalpy of T5, ranging from perfect-gas to near-equilibrium flow, and a large range of pressure. Differential interferometry and surface heat transfer constituted the diagnostics used. The experiments were accompanied by detailed numerical computations of the flow fields, which were used to construct interferograms for comparison with the experimental ones. Theoretical analysis of the problem led to a complete understanding of the correlation of the dimensionless stand-off distance with dimensionless reaction-rate parameter, and its extension to reacting gas mixtures. Numerical and experimental results support the correlation very well. A previous theoretical analysis of dissociating flow along a streamline downstream of a curved shock has been extended to include the effects of recombination. The limits of binary scaling were delineated. Initial exploratory experiments on the detection of the high vorticity layer and its stability were performed.

2.1 Interferometry and heat flux measurements

The experimental differential interferograms were compared with the images constructed from computational flow fields. Generally, good agreement of fringe pattern and shock shape was observed. Fig. 2 shows the comparison of experimental and computational differential interferograms of the flow of nitrogen over a 4 in. diameter sphere at a specific reservoir enthalpy of 16 MJ/kg and a reservoir pressure of 60 MPa. As may be seen, the features of the photo are faithfully reproduced by the computation, both qualitatively and quantitatively, in most of the flow field. Small differences near the shock give valuable information about the beginning of the dissociation process.

Experimental heat flux measurements show:

1. Good agreement among the measured stagnation point heat transfer rates, computational results and Fay and Riddell's theoretical predictions. This also provides confirmation of T5 enthalpy.
2. For nitrogen and air, the measured heat flux distributions were also in good agreement with numerical results and Lees' theory.
3. For carbon dioxide, large differences between experimental and theoretical heat flux distributions were observed. Early transition, tripped by surface roughness is a possible cause.

2.2 Binary scaling law

An approximate analytical solution was obtained for inviscid hypervelocity dissociating flow over spheres. The solution explains the correlation between the dimensionless stand-off distance and the dimensionless reaction rate parameter previously observed by Hornung (1972) for nitrogen. The physics of the correlation is equivalent to binary scaling. Based on the solution, a new dimensionless reaction rate parameter Ω is defined to generalize Hornung's correlation for more complex gases than nitrogen. The physical meaning of Ω is recognized as the ratio of

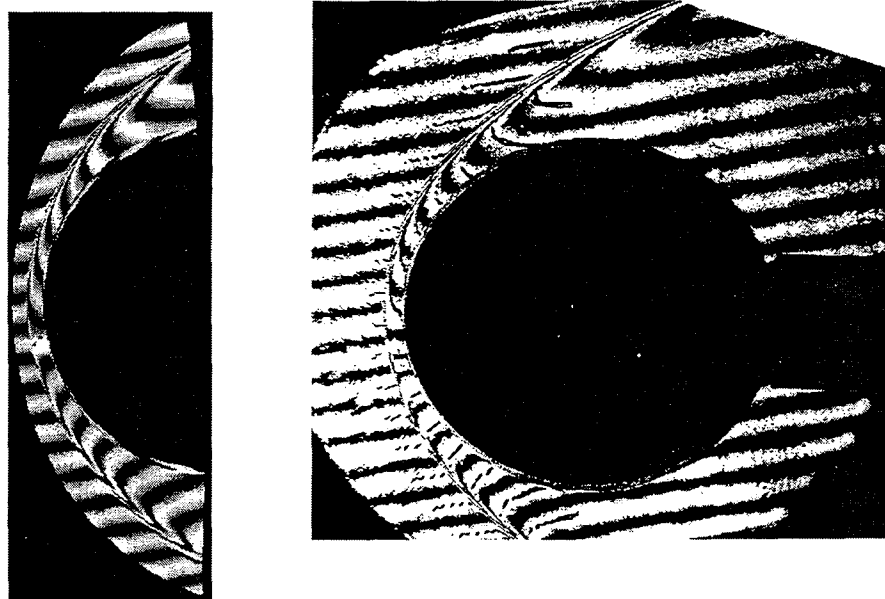


Fig. 2. Comparison of experimental and computed differential interferograms of nitrogen flow over a sphere. Free-stream conditions: 5.08 km/s, 0.04 kg/m³, 16.56 MJ/kg. The photograph on the right is a finite-fringe differential interferogram of nitrogen flow over a sphere. The picture on the left is a corresponding computed interferogram at the same conditions as the experiment. Except for a slight difference in the vicinity of the shock, the two pictures are virtually congruent. To show this, a line along the center of the calculated white fringe is superimposed on the photograph.

the energy absorption rate by chemical reactions just after the normal shock to the input rate of free-stream kinetic energy. This suggests that there exists a universal relationship which applies to all gases and free-stream conditions, provided that the Mach number is sufficiently high. The form of the function is also determined by the approximate analysis and is presented together with computational results for air in Fig. 3 and together with experimental results from T5 for carbon dioxide in Fig. 4. Experimental and numerical results confirm the new correlation.

The effect of nonequilibrium recombination downstream of a curved two-dimensional shock was also investigated. An analytical solution for an ideal dissociating gas was obtained, giving an expression for dissociation fraction as a function of temperature on a streamline. The solution agrees well with the numerical result and provides a rule of thumb to check the validity of binary scaling for the experimental conditions. The effects upon the binary scaling of the large difference in free-stream temperature between flight and free-piston shock tunnel conditions are discovered.

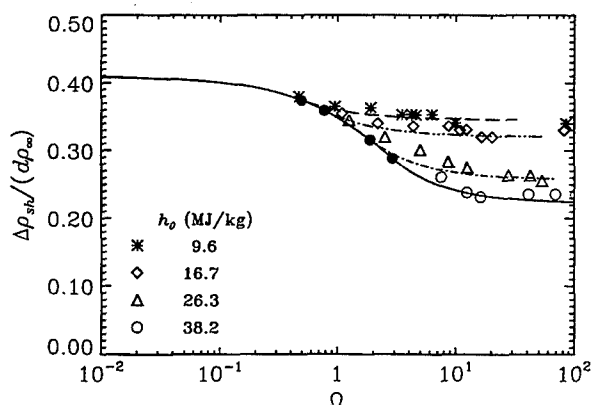


Fig. 3. Dimensionless stand-off distance plotted against reaction rate parameter for different specific reservoir enthalpies in air. The symbols represent computational results. The filled circle is the point at which the curve branches off from the solid line for each ρ_e/ρ_{sh} .

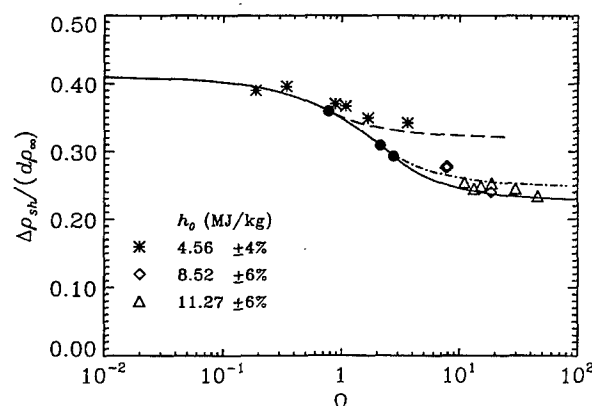


Fig. 4. Dimensionless stand-off distance plotted against reaction rate parameter for different specific reservoir enthalpies in carbon dioxide. The symbols represent experimental results.

Though theoretical and computational results show that recombination is important in parts of the flow field, binary scaling is a satisfactory model for global quantities such as the stand-off distance.

2.3 Vorticity generation by curved shock

Fig. 5 shows a partial view of a resonantly-enhanced shadowgraph of carbon dioxide flow over a sphere. Streamlines are marked by seeding the flow with sodium and using a light source tuned to one of the sodium D lines, see also section 3. At the side of the sphere these show similarities with the instability of a shear layer. The vortical structures may be the result of Kelvin-Helmholtz instability of the high-vorticity layer at the edge of the high-entropy layer near the body. If they are, to our knowledge, this resonantly-enhanced shadowgraph is the first visualization of this phenomenon. Further experiments are needed before definite conclusions may be reached. Nevertheless, the resonantly-enhanced shadowgraphic technique provides a promising tool for studying the vorticity-interaction problem in hypervelocity blunt-body flows.

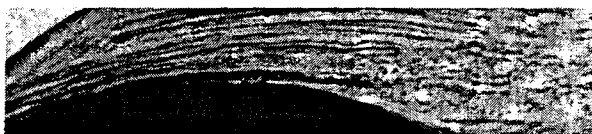


Fig. 5. Partial view of a resonantly-enhanced shadowgraph of CO₂ flow over a sphere of 4 in diameter. Free-stream condition: CO₂, 3.55 km/s, 0.081 kg/m³, 11.27 MJ/kg.

3. TRANSITION AT HIGH ENTHALPY

One of the most serious gaps in the knowledge of hypervelocity flows is that concerning transition to turbulence in the boundary layer. T5 created the opportunity to achieve Reynolds numbers in the right range at high enthalpy in a steady nozzle expansion. Reflected-shock tunnels can only provide a notoriously noisy environment. The question therefore needs to be addressed as to whether the mechanism of transition that occurs is the same as that occurring in flight. Nevertheless, an experimental study was undertaken, which yielded some interesting results.

A slender cone of half-angle 5 deg. was instrumented with thermocouple heat transfer gauges. Flows of air, nitrogen, carbon dioxide, and helium over this cone were studied at specific reservoir enthalpies ranging from 3 to 22 MJ/kg. Flow visualization was achieved with resonantly enhanced interferometry. The resonant enhancement is necessary to make the visualization technique sufficiently sensitive.

The experiments show that the mechanism of transition in the range studied is via the Tollmien-Schlichting instability. This is not surprising, since the frequency of the second mode at these conditions is approximately 1 MHz which is higher than any of the noise sources in the facility. On the other hand, the TS frequency is typically 150 kHz, a value which is abundantly present in the noise spectrum. Two flow visualization photographs of a transitional and of a turbulent boundary layer are shown in Fig. 6 and Fig. 7.



Fig. 6. Flow of nitrogen at $h_0 = 11$ MJ/kg and $p_0 = 60$ MPa (run 360). This resonantly enhanced interferogram shows the boundary layer on the top of the cone, starting on the left from $x = 510$ mm (corresponding to $Re = 2.75$ million) to $x = 680$ mm ($Re = 3.77$ million). The pictures below magnify portions of the one above three times ($3\times$). A wave in the laminar part of the flow appears distinctly and its wavelength is approximately 1.5 cm.



Fig. 7. Flow of nitrogen at $h_0 = 20$ MJ/kg and $p_0 = 55$ MPa. Resonantly enhanced interferogram showing a turbulent boundary layer.

The most interesting result of the study is that a clear trend may be observed in the behavior of the transition Reynolds number with specific reservoir enthalpy. This trend is stronger for air than for nitrogen, see Fig. 8. In this, the transition Reynolds number is evaluated at the reference temperature, in order to eliminate the separate dependence of the data on Mach number, specific heat ratio, and wall temperature. Since the lowest enthalpy at which dissociative real-gas effects are observed is lower in air than in nitrogen, this appears to indicate that the appropriate dimensionless variable to plot on the horizontal axis is h_0/D , where D is some representative dissociation energy. In the case of nitrogen, the value of D is, of course, the dissociation energy of nitrogen. If D is taken to be the dissociation energy for oxygen in the case of air, the two curves do not quite collapse when plotted against h_0/D , this procedure overcompensates slightly for the difference between air and nitrogen. To test the notion that the effect is proportional to h_0/D , a few experiments were carried out with carbon dioxide, with even lower first dissociation energy, and with helium, where ionizational real-gas effects appear only at very high enthalpy, well beyond the range tested. The carbon dioxide flows indeed showed a much stronger dependence of Re_{tr}^* on h_0 than nitrogen and air, and helium showed no dependence at all. Further experiments are planned to examine this effect in more detail.

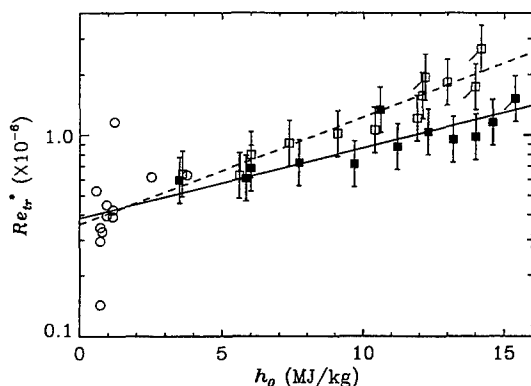


Fig. 8. Transition Reynolds number evaluated at the reference temperature. Our data are shown as square symbols (open for air and solid for nitrogen). The error bar shown is an approximation of the accuracy in determining Re_{tr}^* . The data shown as open circles come from DiCristina (1970) and Demetriades (1977). The two lines are least-squares-fit approximations of the open or the solid symbols respectively.

4. SHOCK-ON-SHOCK INTERACTION

4.1 Introduction

The impingement of shock waves on blunt bodies in steady supersonic flow is known to cause extremely high local heat transfer rates and surface pressures. Although this phenomenon has been studied in cold hypersonic flow, the effects of dissociative relaxation processes are unknown. Shock impingement phenomena, which constrain the development of hypervelocity vehicles, are discussed in the literature by many authors, notably by Edney (1968 a,b).

For the inviscid, compressible flow of a perfect gas a sufficient set of dimensionless parameters to describe any dimensionless quantity ϕ in the flow is,

$$\phi = \phi(M, \gamma, \beta_1, \Lambda, \Gamma),$$

where M is the free stream Mach number, γ is the ratio of specific heats, β_1 is the impinging shock angle, Λ describes the position of the impinging shock and Γ defines the body geometry. Consider the case of a given gas and fixed free stream condition, impinging shock strength and body geometry. The only remaining dependence is then the location of the impingement point relative to the body, i.e.,

$$\phi = \phi(\Lambda).$$

On the basis of an experiment such as this, Edney (1968 a,b) observed and categorized six interaction regimes known as types I–VI. Edney rationalized the observed flow fields through local analysis about shock wave intersection points in the pressure–flow deflection angle plane (p – δ plane). The key conclusion drawn from such an analysis is the role of the three-shock solutions. Based on the assumption of straight shocks in the vicinity of the interaction, the flow field for the global type IV interaction, whereby a supersonic jet penetrates a region of low subsonic flow [see Edney (1968 a,b) or Fig. 11], can be solved approximately as a free streamline flow up to some unknown length scale. Typically this length scale is specified in terms of the width of the jet.

According to Edney's model, the heat transfer is determined by the attachment at the body surface of the shear layers generated at the shock impingement points. A correlation was obtained between local pressure and local heat transfer rate at the surface. A further observation made by Edney is that the jet curvature increases as the intersection point moves closer to the normal-shock point. Some recent contributions to the literature are noted in the references.

4.2 Experiment and results

We have conducted an experimental investigation of the nominally two-dimensional mean flow that results from the impingement of an oblique shock wave on the leading edge of a cylinder. These initial experiments, comprising 35 shots, were conducted with nitrogen test gas at nozzle reservoir enthalpies of 3 MJ/kg and 12.5 MJ/kg and reservoir pressures of 12 MPa and 25 MPa, respectively. The reservoir gas was expanded through a contoured axisymmetric nozzle with area ratio 109.5 to yield a nominal Mach number of 5.5 in the test section. The cylinder was 37.5 mm in diameter with aspect ratio 4.5 and the flow was deflected 7 degrees by the incident planar shock wave.

The effects of variations in shock impingement geometry were visualized using infinite fringe differential interferometry with vertical beam shear. Figs. 9 to 11 illustrate type II, III and IV interactions, at stagnation enthalpies of 3 MJ/kg and 12.5 MJ/kg. The incident shock is curved in the transverse plane (concave down) at the edge of test section and some fringe shift is observed below this wave. However, the main centerline disturbance is generally at the top of the line-of-sight-integrated image.

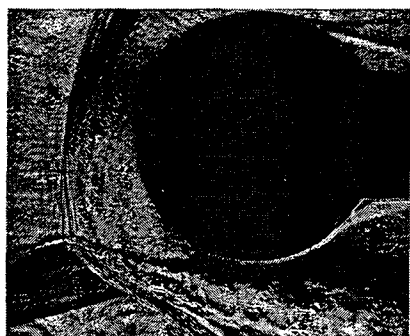


(a) 3 MJ/kg

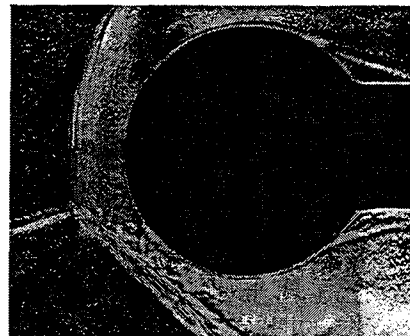


(b) 12.5 MJ/kg

Fig. 9. Differential interferograms of type II interactions.



(a) 3 MJ/kg

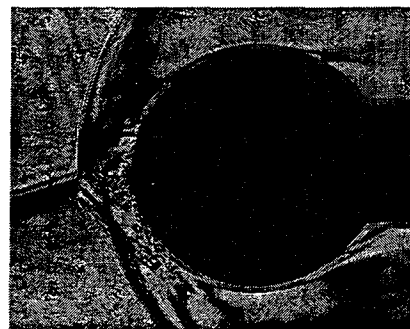


(b) 12.5 MJ/kg

Fig. 10. Differential interferograms of type III interactions.



(a) 3 MJ/kg



(b) 12.5 MJ/kg

Fig. 11. Differential interferograms of type IV interactions.

At the lowest impingement point reported in this paper the type I-II transition has already occurred with the incident shock wave impinging somewhat below the lower sonic line (Fig. 9). In the low enthalpy case a Mach stem connects the λ -shock pattern at the impingement point to the bow shock of the cylinder. At the intersection point a strong vortex sheet is generated, separating the upper region of subsonic flow from the lower region of supersonic flow. No transmitted wave is resolvable at the upper end of the Mach stem which appears to join smoothly into the bow shock in the vicinity of the sonic line. The upper portion of the bow shock remains symmetrical. In the high enthalpy case the bow shock remains undisturbed. However, a point of inflection is observed immediately above the intersection point.

In the type III experiments (Fig. 10) the incident shock wave intersects the bow shock wave in the subsonic region, somewhat below the geometric stagnation point. For both enthalpies the Mach stem has merged with the bow shock wave and the λ -shock pattern is preserved at the intersection point. The influence of the impinging shock wave is now global and both the radius of curvature and the stand-off distance of the asymmetrical upper portion of the bow shock have increased to match the λ -shock pattern at the impingement point. Dominated by the inertia of the supersonic stream, the shear layer is deflected only in the immediate vicinity of the cylinder.

Generally, the stand-off distance decreases with increasing enthalpy and this influences the impingement of

the shear layer on the body. In the high-enthalpy case, the resulting compression waves that are observed as a series of nearly vertical white lines below the impingement point, steepen the lower shock. Note the analogy between this phenomenon and the mechanism of complex Mach reflection.

When the incident shock wave impinges in the vicinity of the normal-shock point a type IV flow results (Fig. 11). The λ -shock pattern is preserved, and the supersonic transmitted portion of the bow shock forms a second inverted λ -shock with the subsonic continuation of the bow shock below the interaction. The flow behind the oblique shock wave connecting the two λ -shocks is supersonic and forms a jet that turns upwards under the action of the pressure gradient produced by the second λ -shock. The strongly curved shear layer generated at the upper λ -shock forms large plumes as it passes above the cylinder. The stand-off distance and jet width are reduced in the high-enthalpy case but this also depends strongly on the location of the impinging shock. A portion of the supersonic flow is now turned, so that it passes above the cylinder, and hence the stagnation streamline must pass through the supersonic jet. The stagnation density is higher for streamlines that pass through the supersonic jet than for streamlines that cross the adjacent strong bow shock. The higher density and large unsteady velocity gradients produced by the impingement of the supersonic jet provide the mechanism for local increase of the heat transfer rate.

4.3 Conclusions

Experiments conducted in T5 provided insight into real-gas effects on the global flow. Generally, real-gas effects are seen to increase the range of shock impingement points for which enhanced heating occurs. They further influence the Mach stem form in type II flows, the deflection of the shear layer in type III flows and the length scales associated with the type IV jet.

5. LASER-INDUCED THERMAL ACOUSTICS

5.1 Description of LITA diagnostic technique

Over the past year, work on optical diagnostics for T5 has progressed markedly with the development at GALTIT of laser-induced thermal acoustics, or LITA, a new technique superior in many respects to other laser diagnostic techniques. In the first series of experiments LITA has provided relatively simple, accurate, single-shot, spatially resolved measurements of sound speed, transport properties, and collisional thermalization rate in laboratory air. Current experiments apply LITA for single-shot measurement of these properties, as well as of the complex susceptibility, susceptibility spectra, and gas velocity. Absolute species concentration and temperature measurements may be extracted from susceptibility spectra. The work on LITA performed at GALTIT has the interest of the wider combustion diagnostics community because

- quantitative signal analysis is simple (cf., LIF, DFWM),
- exhaustive information about probed species is not required (cf., LIF),

- LITA excels in strongly quenching environments (e.g., where collision rates are high, a requirement for fast chemistry; cf., LIF),
- LITA requires only standard lasers and equipment, and
- LITA's capabilities exceed those of other techniques (e.g., single-shot transport-property, absolute concentration, and velocity measurements)
- LITA signals are relatively strong.

LITA is a four-wave mixing (FWM) technique related to coherent anti-Stokes Raman scattering (CARS) and degenerate FWM (DFWM). In FWM techniques, crossed-laser beams form electric-field interference "gratings" in the probed volume. Electric field gratings generate susceptibility (index-of-refraction) gratings via nonlinearities of the probed medium. These gratings scatter light from a third beam into the signal beam. If the intensity of the signal beam can be related to properties of the medium, FWM can be used to measure these properties remotely. The principal difference between the techniques is the type of nonlinearity used to form the susceptibility gratings. CARS and DFWM form gratings by quantum mechanical effects.* These gratings have short lifetimes (< 5 ns at STP), since they are destroyed by molecular collisions. LITA gratings are acoustic: crossed driver lasers generate acoustic pressure and temperature gratings via electrostriction and thermalization, two semi-classical opto-acoustic effects. Acoustic gratings are damped by thermal and viscous diffusion on a much longer time scale (e.g. 1 μ s) than quantum mechanical gratings. Longer time scales permit single-shot time resolution of the evolution of the signal which allows sound speed measurement. Furthermore, the formation and lifetime of acoustic gratings are *enhanced* by quenching, which has the opposite effect on quantum-mechanical gratings.

The mathematics of acoustic grating formation is generally far simpler than that of quantum-mechanical gratings. This makes the expression relating experimental LITA signals to gas properties simpler than that of DFWM or CARS. Thus, it was possible to predict the LITA signal with an analytical expression derived previously from the linearized equations of light scattering and hydrodynamics, see Cummings (1992). By fitting the experimental signal to the prediction, sound speeds could be obtained to an accuracy within the uncertainty of independent determinations ($\sim 0.5\%$). Transport properties obtained this way matched published quantities to within $\sim 30\%$. A finite-beam-size effect neglected in the predictive analysis limited the accuracies of these measurements. The analysis has since been extended to include this additional effect, the effect of electrostriction, and the effect of finite laser linewidth.

* Thermal or acoustic gratings often contribute to DFWM signals, especially at high densities. However, the contribution to the signal from these gratings is generally regarded as "interference" with the (desired) signals from the quantum-mechanical gratings. For this reason, the distinction is made that DFWM gratings are purely quantum-mechanical and LITA gratings are purely acoustic, i.e., LITA signals often interfere with DFWM signals.

5.2 Results of demonstration experiments

Experiments conducted to date use the setup schematized in Fig. 12. A pulsed narrowband dye laser pumped by a Q-switched, frequency-doubled Nd:YAG laser drives the acoustic waves. The dye laser emits about 40 mJ of light tuned between 587 nm and 592 nm in approximately 5 ns pulses. Three-millimeter-wide driver beams are formed from the dye laser emission by a 50% beamsplitter (B.S.) and a mirror m_1 . The driver beams intersect at the focus of the 400 mm lens where they approximate finite plane waves about 200 μm in diameter. The distance between the parallel beams, adjusted using micrometer translation stages, sets the beam-crossing angle. Three-dimensional phasematching (BOXCARS) geometries with crossing an-

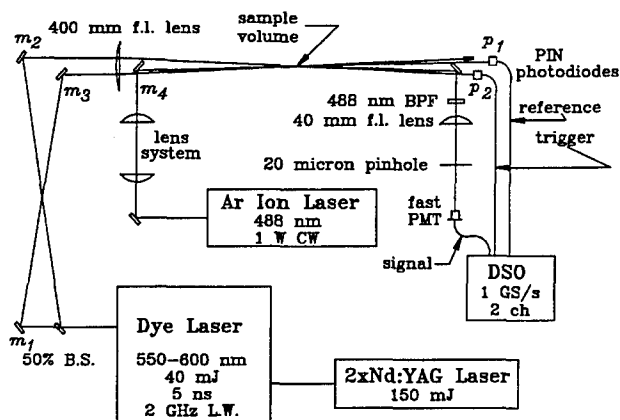


Fig. 12. Schematic diagram of LITA operation. For notation see text.

gles ranging from 1.0° to 2.3° were used in these experiments. The acoustic gratings are formed in the sample volume defined by the intersection of these beams. Detection of the driver beam pulse by a silicon PIN photodiode, p_1 , triggers the acquisition of the LITA signal. Light from a 1W CW argon ion "source" laser operating at 488 nm scatters coherently off the acoustic gratings into the signal beam. A two-lens system adjusts the source beam diameter, which ranged from about 200 μm to 2 mm. Phase-matching adjustments are made using a micrometer-driven translation stage under m_4 . A silicon PIN photodiode, p_2 , monitors the intensity of the source beam.

The signal beam detection system consists of a fast photomultiplier tube (PMT) with at least 500 MHz signal bandwidth. Optical filters, including a 10 nm interference filter at 488 nm and a 40 mm lens/20 μm spatial filter, prevent signal contamination. The LITA signal path-length to the detector is about 2.5 m. Data are recorded using a fast digital storage oscilloscope (DSO). This records typically 500-to-2000-sample time histories of signals from the PMT and p_2 .

The first LITA experiments used laboratory air. Non-resonant electrostriction generated LITA signals with a signal-to-source beam intensity ratio, or reflectivity, of $\sim 10^{-8}$. An average over 256 shots yields the nonresonant data plotted as the dotted curve in Fig. 13. The modulation or "ringing" results from beating between Doppler-

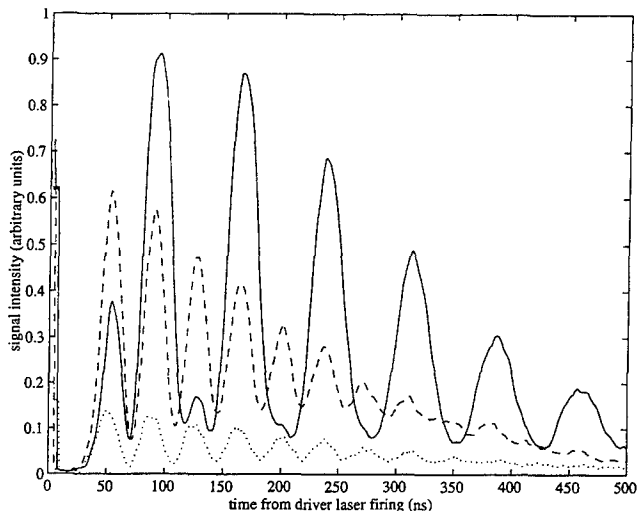


Fig. 13. LITA signals averaged over 256 shots in room air near a weak line of NO_2 which is present to about 50 ppb. Full line: Signal recorded near the peak of the spectral line. Dashed line: Resonantly enhanced signal near the spectral line. Dotted line: Non-resonant signal. By fitting these to the theoretical prediction, the speed of sound is obtained to $\pm 0.5\%$, and the bulk viscosity to $\pm 10\%$.

shifted light scattered off the laser-induced acoustic waves. This occurs at a frequency proportional to the sound speed and known geometrical and optical parameters. The frequency of the modulation (about 26 MHz) yields a sound speed accurate within the uncertainty of the knowledge of the laboratory sound speed ($\sim 0.5\%$). Electrostriction is resonantly enhanced near absorption lines. The resonantly-enhanced signal recorded near a weak line of NO_2 appears as a dashed curve in Fig. 13 for comparison. When the driver laser is tuned to an absorption line of the gas, molecules absorb light energy and release thermal energy through inelastic collisions, generating a thermal grating. If thermal gratings form rapidly, expansion of the gas emits acoustic waves. The signal recorded near the peak of the absorption line is the solid curve plotted in Fig. 13, which shows the difference in signature between electrostriction and thermalization signals. These signals are proportional to the real and imaginary parts of the complex gas susceptibility respectively, so that this provides a measurement of the complex susceptibility. The high sensitivity of LITA is demonstrated by this experiment, since the ambient air contained less than 50 ppb of NO_2 according to the Southern California Air Quality Management District.

Seeding the gas with NO_2 provided LITA signals that were several orders of magnitude stronger than the signals obtained from room air, with estimated reflectivities around 10^{-4} . A sample single-shot LITA signal is presented in Fig. 14 with the theoretical fit plotted as a dashed curve. The sound speed and transport coefficients used in the fit are published values for dry air. Clearly, the theoretical model gives an excellent prediction. Here, the thermalization process is treated as the superposition of two single-rate thermalizations: A fast ~ 10 ns process and a

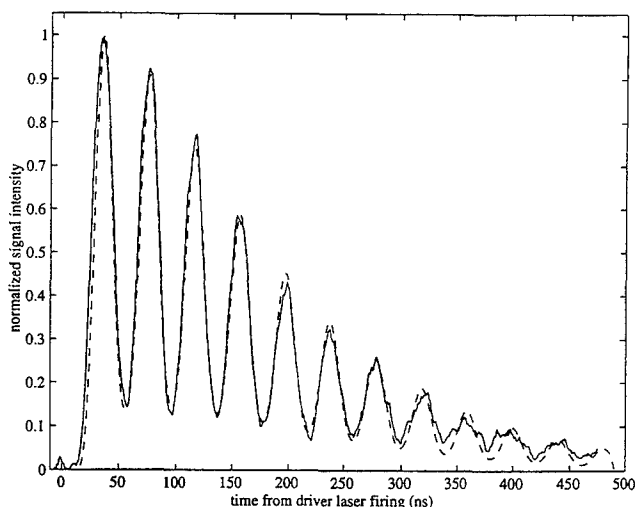


Fig. 14. Single-shot LITA record in room air seeded with NO_2 . Dashed curve shows theoretical prediction.

slow ~ 100 ns process. A better fit to the data could be obtained by adopting a more accurate thermalization model and source-beam-profile model in the analysis (a top-hat profile is assumed) and by including the effect of source-beam phase noise. These improvements are presently being incorporated into a computer fitting routine for LITA signals.

Information gained from these experiments has guided plans for future experiments. The accuracy of the simple analytical model and the relative strength of LITA signals have opened new paths of exploration: multiplex LITA and LITA velocimetry. Absolute species population and concentration measurements may be extracted from spectra obtained by LITA experiments in which the source laser is scanned across a band of species spectral lines. Such scanning techniques are common in laser diagnostics; however, they are not yet applicable to pulsed facilities such as T5. Alternatively, a broadband source laser can be used along with dispersion of the signal beam in a spectrometer to obtain single-shot "multiplex" spectra. Multiplexing using conventional FWM techniques has two drawbacks avoided by LITA:

- Analyzing multiplex spectra from "quantum-mechanical" grating techniques is complicated by quantum interferences, etc. Because LITA uses classical gratings, quantum mechanical complications are avoided. The simple analysis already experimentally verified extends readily to multiplex LITA.
- Much of the energy of the source laser falls between lines and is wasted, thus a high reflectivity is needed. Spectrometer losses compound this effect. LITA signals with reflectivities of 10^{-4} can be used in multiplex experiments studying even trace species. Furthermore, a long-pulse, broadband source laser such as a flashlamp-pumped dye laser may be used. These are available inexpensively with high pulse energies (> 1 J).

Multiplex experiments are currently under construction. A flashlamp-pumped dye laser with about 2.5 J per pulse is being modified for less mode structure. Laser mode structure interferes with all multiplex measurements. A high resolution echelle spectrometer with multiple inputs has been aligned and focused. Spectra fall on a computer-controlled precision CCD array. The spectrometer has a dynamic range of at least 2000:1 and a frequency resolution measured to be better than 3 GHz at 589 nm ($> 10^5:1$).

LITA velocimetry, by analogy with laser Doppler velocimetry (LDV), is also actively being pursued at GALCIT. In this technique, the Doppler shift of light scattered off convecting acoustic gratings is measured relative to an unshifted reference. This should make single-shot velocimetry possible in pulsed experiments with flow velocities from 50 to 3000+ m/s (estimation based on detector frequency response, beam size and duration effects etc.) For these experiments, a windowed test section with optical access from four sides has been designed and built. The test section is designed to be used in connection with a variety of test articles including a small combustion-driven shock tunnel capable of generating exit velocities of 3000 m/s in air and 7000 m/s in hydrogen. Alignment and testing will first be performed on a steady Mach 2 jet of air from the laboratory air supply.

LITA tests in T5 have been postponed until Spring 1995 to allow experimental development and exploration of the potential for LITA diagnostics. The risk reduction from this measured development and knowledge gained about the use of this promising diagnostic technique will enhance T5 LITA tests. In addition, timely development of generic LITA capabilities such as spectral multiplexing and velocimetry is in the broad interest of the combustion diagnostics community.

6. CONCLUSION

Results from four selected graduate research projects conducted in the T5 laboratory in the last two years have been presented. These have produced extensive new data that have widened the understanding of hypervelocity flows significantly. In addition a new laser diagnostic technique for sound speed and transport property measurement has been developed. The operation of T5 in a university environment has demonstrated that small-scale research of this style is very cost-effective in the advancement of hypervelocity gasdynamics. At the same time, the facility is large enough to make it suitable for some hypervelocity testing for industry.

Acknowledgements

This work was supported by AFOSR Grant F49610-92-J-0110 (Dr. L. Sakell) and AFOSR grant F49620-93-1-0338 (Dr. J. Tishkoff).

References

- Bakos R. J., J. Tamagno, O. Ryszkalla, M. V. Pulsonetti, W. Chinitz, and J. I. Erdos, 1992 "Hypersonic mixing and combustion studies in the Hypulse facility," *J. Propulsion and Power*, 8 900-906.

- Bélanger J. and H. G. Hornung 1994a "Transverse jet mixing and combustion experiments in the hypervelocity shock tunnel T5", AIAA paper 94-2517.
- Bélanger J. and H. G. Hornung 1994b "Numerical prediction and actual behavior of the free-piston shock tunnel T5", AIAA paper 94-2527.
- Candler G.V. 1988 "The computation of weakly ionized hypersonic flows in thermo-chemical nonequilibrium", Ph.D. Thesis, Stanford University.
- Cummings, E. B. 1992 "Techniques of Single-shot Thermometry by Degenerate Four-wave mixing (DFWM)", GALCIT Fluid Mechanics Report FM 92-2, Caltech, Pasadena, CA.
- Cummings, E. B. 1994 "Laser-induced Thermal Acoustics (LITA): Simple Accurate Gas Measurements", to be published in *Optics Letters*.
- Demetriades, A. 1977 "Laminar boundary layer stability measurements at Mach 7 including wall temperature effects", Rept. AFOSR-TR-77-1311, Air Force Office of Scientific Research, Washington, D. C.
- DiCristina, V. 1970 "Three-dimensional laminar boundary-layer transition on a sharp 8° cone at Mach 10", *AIAA Journal* 8, 852-856.
- Edney B.E. 1968a "Effects of Shock Impingement on the Heat Transfer Around Blunt Bodies". *AIAA Jour* 6 15-21.
- Edney B.E. 1968b "Anomalous heat transfer and pressure distributions on blunt bodies at hypersonic speeds in the presence of an impinging shock". FFA-115, The Aeronautical Research Institute of Sweden.
- Eitelberg G. 1992 "The high-enthalpy shock tunnel in Göttingen", AIAA Paper No. 92-3942, Nashville.
- Germain, P. 1993 "The boundary on a sharp cone in high enthalpy flow", Ph.D. thesis, California Institute of Technology.
- Germain P., Cummings E. and Hornung H. 1993 "Transition on a sharp cone at high enthalpy; new measurements in the shock tunnel T5 at GALCIT. AIAA 93-0343, Reno, Nevada.
- Germain P., and Hornung H. 1993 "The boundary on a sharp cone in high enthalpy flow", *Proc. 19th Int Symp on Shock Waves*, Marseille, Springer Verlag, to appear.
- Hornung, H. G. 1972 "Nonequilibrium dissociating nitrogen flows over spheres and circular cylinders", *J. Fluid Mech.*, 53, 149-176.
- Hornung, H. G. 1992 "Performance data of the new free-piston shock tunnel at GALCIT", AIAA 92-3943.
- Hornung H. G. 1993 "Hypervelocity flow simulation, needs, achievements and limitations", *Proceedings, 1st Pacific International Conference on Aerospace Science and Technology*, Tainan, Taiwan, pp. 1-10.
- Klopfer G.H. and Yee H.C. 1988 "Hypersonic shock-on-shock interaction on blunt cowl lips". AIAA Paper 88-0233.
- Lukasiewicz, J. 1973 "Experimental Methods of Hypersonics", Marcel Dekker.
- Roberts G. T., R. G. Morgan, and R. J. Stalker 1993 "Influence of the secondary diaphragm on flow quality in expansion tubes", *Proceedings of 19th International Symposium on Shock Waves*, Marseille, France, July, 1993, Springer-Verlag, to appear.
- Wen C.Y. and Hornung H.G. 1993 "Non-Equilibrium Recombination after a Curved Shock Wave," *Proceedings of 1st Pacific International Conference on Aerospace Science and Technology*, Vol. 2, 639-647, Tainan, Taiwan, Dec., 1993.
- Wen C.Y. and Hornung H.G. 1993 "Experiments on Hypervelocity Dissociating Flow over Spheres," *Proceedings of 19th International Symposium on Shock Waves*, Marseille, France, July, 1993, Springer-Verlag, to appear.
- Wen C.Y. "Hypervelocity flow over spheres", Ph.D. thesis, California Institute of Technology.
- Wieting A.R. and Holden M.S. 1989 "Experimental shock wave interference heating on a cylinder at Mach 6 and 8". *AIAA Jour.* 27 1557-1565.

Shock Wave Interactions in Hypervelocity Flow

S. R. Sanderson and B. Sturtevant

California Institute of Technology, Pasadena, CA 91125, USA

Abstract. The impingement of shock waves on blunt bodies in steady supersonic flow is known to cause extremely high local heat transfer rates and surface pressures. Although these problems have been studied in cold hypersonic flow, the effects of dissociative relaxation processes are unknown. In this paper we report a model aimed at determining the boundaries of the possible interaction regimes for an ideal dissociating gas. Local analysis about shock wave intersection points in the pressure-flow deflection angle plane with continuation of singular solutions is the fundamental tool employed. Further, we discuss an experimental investigation of the nominally two-dimensional mean flow that results from the impingement of an oblique shock wave on the leading edge of a cylinder. The effects of variations in shock impingement geometry were visualized using differential interferometry. Generally, real gas effects are seen to increase the range of shock impingement points for which enhanced heating occurs. They also reduce the type IV (Edney 1968 a,b) interaction supersonic jet width and influence the type II-III transition process.

Key words: Shock-on-shock interaction, Shock impingement, Hypervelocity flow

1. Introduction

Shock impingement phenomena, which inhibit the further development of hypervelocity vehicles, are discussed in the literature by many authors, notably by Edney (1968 a,b). For the inviscid, compressible flow of a perfect gas a sufficient set ϕ of dimensionless parameters to describe any quantity in the flow is, $\phi = \phi[M, \gamma, \beta_1, \Lambda, \Gamma]$, where M is the freestream Mach number, γ is the ratio of specific heats, β_1 is the impinging shock angle, Λ describes the position of the impinging shock and Γ is a set of parameters defining the body geometry. Consider the case of a given gas and fixed freestream condition, impinging shock strength and body geometry. The only remaining dependence is then the location of the impingement point relative to the body, i.e., $\phi = \phi[\Lambda]$. As the incident shock wave is translated relative to the body it potentially intersects with all possible shock strengths of both positive and negative slope. On the basis of an experiment such as this, with spherical and modified spherical bodies, Edney (1968 a,b) observed and categorized six interaction regimes; known as types I-VI. Edney rationalized the observed flowfields through local analysis about shock wave intersection points in the pressure-flow deflection angle plane (p - δ plane). The key conclusion drawn from such an analysis is the role of the three-shock solutions (or λ -shocks) and this is discussed further in §2. Based on the assumption of straight shocks in the vicinity of the interaction, the flow field for the global type IV interaction, whereby a supersonic jet penetrates a region of low subsonic flow (see Edney 1968 a,b or Fig.4), can be solved approximately as a freestreamline flow up to some unknown length scale. Typically this length scale is specified in terms of the width of the jet.

According to Edney's model, the heat transfer is determined by the attachment at the body surface of the shear layers generated at the shock impingement points. A correlation was obtained between local pressure and local heat transfer rate at the surface. A further observation made by Edney is that the jet curvature increases as the intersection point moves up. Some recent contributions to the literature are noted in the references of this paper.

2. Local analysis for an ideal dissociating gas

Local analysis about shock-surface intersection points in the p - δ plane is well known in the Mach reflection literature (e.g. Hornung 1986). Our purpose here is to generalize these tools to the case of oblique translational shock waves where both the upstream and downstream conditions are non-equilibrium states with respect to the internal degrees of freedom of the gas. This analysis is performed for a one-dimensional shock and subsequently extended to oblique waves.

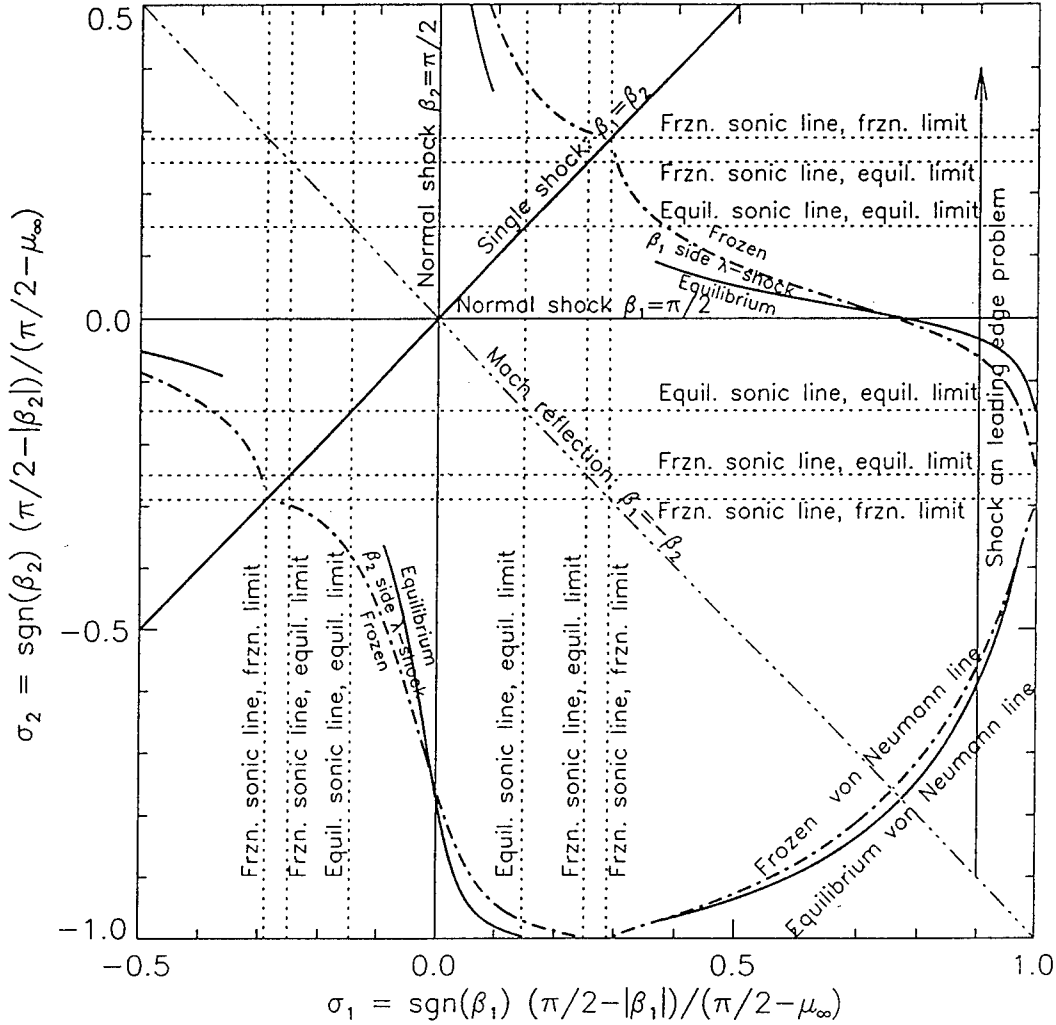


Fig. 1. Map of interaction regimes for two intersecting oblique shock waves of angles β_1 and β_2 . Shock angles are normalized so that $\sigma = 0$ corresponds to a normal shock wave. Mach waves correspond to $\sigma = \pm 1$. The freestream conditions are taken as $H_0 = 0.5$, $P = 0.03$ (or $M_\infty = 5$ with $\gamma = 4/3$), $\alpha_1 = 0$ and $\hat{p}_d = 10^6$.

Consider the dimensionless form of the continuity and momentum equations that apply across a one-dimensional translational discontinuity and throughout the downstream relaxation zone,

$$\hat{p}\hat{u} = 1, \quad \hat{p} = 1 + \frac{1}{P} \frac{\hat{p} - 1}{\hat{p}}, \quad (1, 2)$$

where $P = p_1/\rho_1 u_1^2$. The symbols have the usual meanings and generally $\hat{\phi} = \phi_2/\phi_1$.

We use Lighthill's (1957) model for the thermodynamics of an ideal dissociating gas (IDG):

$$p = \frac{k}{2m}(1 + \alpha)\rho T, \quad h = \frac{k}{2m}[(4 + \alpha)T + \alpha\theta_d], \quad (3, 4)$$

where k is Boltzmann's constant, m is the mass of one atom of the gas, θ_d is a temperature characterizing the dissociation energy and α is the dissociated mass fraction. Using Eq.4 the dimensionless energy conservation equation becomes,

$$(4 + \alpha_2) \frac{\hat{T}}{D} + \alpha_2 + \frac{K}{\hat{\rho}^2} = H_0, \quad (5)$$

where the dimensionless parameters are $D = \theta_d/T_1$, $K = mu_1^2/k\theta_d$ and $H_0 = 2mh_0/k\theta_d$. H_0 is the conserved stagnation enthalpy.

For a nonequilibrium binary mixture, it is sufficient to specify P , H_0 and α_1 . The remaining parameters are then given by the following identities, obtained from H_0 written in terms of conditions upstream of the discontinuity,

$$K = \frac{H_0 - \alpha_1}{1 + 2P \frac{4+\alpha_1}{1+\alpha_1}} \quad D = \frac{4 + \alpha_1}{H_0 - K - \alpha_1}. \quad (6,7)$$

From Eq.3 it follows that $\hat{T} = \frac{\hat{p}(1+\alpha_1)}{\hat{\rho}(1+\alpha_2)}$ and, eliminating \hat{T} and D from Eq.5, with the pressure given by Eq.2, leads to the following quadratic equation for the density,

$$(H_0 - \alpha_2)\hat{\rho}^2 - \frac{\lambda(P+1)}{P}\hat{\rho} + \frac{\lambda - KP}{P} = 0, \quad \lambda = 2KP \frac{4 + \alpha_2}{1 + \alpha_2}. \quad (8)$$

One solution describes the variation of density downstream of a translational shock. The remaining solution describes relaxation of the (possibly) nonequilibrium upstream state without any discontinuity. Both solutions are parameterized in terms of the dissociation mass fraction α_2 .

Eq.8 may be combined with an equilibrium expression (Lighthill 1959) to obtain the asymptotic state far downstream from the translational shock.

The extension to oblique shock waves is obtained in the usual way. The normal components of P and K are given in terms of β , the angle of the oblique shock wave, by

$$P_{1N} = \frac{P_1}{\sin^2 \beta}, \quad K_{1N} = K_1 \sin^2 \beta. \quad (9,10)$$

These are used in Eqs.6, 8, and 2, and the flow deflection δ is given by $\hat{\rho} = \tan \beta / \tan(\beta - \delta)$.

To facilitate the computation of multiple shock jumps for the interaction problem we must find a convenient means of determining P and H_0 downstream of the oblique shock. Trivially $H_{02} = H_{01}$. It can be shown that $K_2 = K_1(\cos^2 \beta + \sin^2 \beta / \hat{\rho}^2)$. P_2 then follows from Eq.6.

3. Continuation of singular solutions

One technique for reducing the amount of information that arises as the number of parameters is increased is to consider only the singular cases that delineate regions of solutions with similar forms. Various special cases arise that are significant in terms of transition to Mach reflection (e.g. Hornung 1986). Now generalize these cases to the asymmetrical interaction of oblique shock waves:

- i. Interaction of shock waves that produce a Mach stem with zero curvature. This is a generalization of the von Neumann condition in Mach reflection.
- ii. Sonic flow downstream of the transmitted shock waves.
- iii. Coalescence of the strong and weak regular solutions such that the shock loci intersect only tangentially. This is a generalization of the maximum deflection condition in Mach reflection.
- iv. Sonic flow downstream of the incident shock waves.
- v. One transmitted shock wave— λ -shocks.

Given the solution for one such set of these singular points, solutions for neighboring values of the parameters may be determined using path-following techniques (Keller 1987). The frozen solution

applies in regions near the shock wave intersection point and the equilibrium solution is valid far from the shock waves. The regular 4-shock intersections map into the 2nd and 4th quadrants of Fig.1 and lie on the surface bounded by the axes and the von Neumann curves. Outside this region the only solutions are the λ -shocks which exist only along lines. If the impingement point on a blunt body maps to a region of Fig.1 where no regular solution exists then the flow must deform in such a way that the λ -shock condition is maintained at the intersection point. This highlights the physical mechanism determining the gross nature of the flowfield. For weak impinging shock waves, shown by the vertical line in Fig.1, the separation of the frozen and equilibrium λ -shock solutions is relatively large. This suggests some effect on the transition from type II to type III. This occurs in the vicinity of the sonic line which is itself sensitive to non-equilibrium processes.

4. Experimental results

We have conducted an experimental investigation of the nominally two-dimensional mean flow that results from the impingement of an oblique shock wave on the leading edge of a cylinder. These initial experiments, comprising 35 shots, were conducted in the GALCIT T5 free piston reflected shock tunnel with nitrogen test gas at nozzle reservoir enthalpies of 3 MJ/kg and 12.5 MJ/kg and reservoir pressures of 12 MPa and 25 MPa, respectively. The reservoir gas was expanded through a contoured axisymmetric nozzle with area ratio 109.5 to yield a nominal Mach number of 5.5 in the test section. The cylinder was 37.5 mm in diameter with aspect ratio 4.5 and the flow was deflected 7 degrees by the incident planar shock wave. The effects of variations in shock impingement geometry were visualized using infinite fringe differential interferometry with vertical beam shear. Figs.2-4 illustrate type II, III and IV interactions at stagnation enthalpies of 3MJ/kg and 12.5 MJ/kg. The incident shock is concave down at the edge of test section and some fringe shift is observed below this wave. However, the main centerline disturbance is generally at the top of the line-of-sight-integrated image.

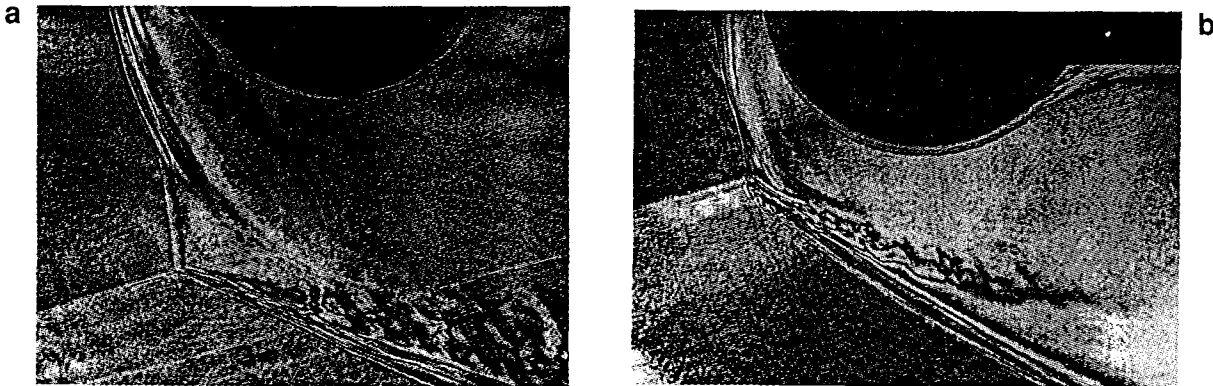


Fig. 2. Differential interferograms of type II interactions. (a) 3 MJ/kg (b) 12.5 MJ/kg

At the lowest impingement point reported in this paper the type I-II transition has already occurred with the incident shock wave impinging somewhat below the lower sonic line (Fig.2). In the low enthalpy case a Mach stem connects the λ -shock pattern at the impingement point to the bow shock of the cylinder. At the intersection point a strong vortex sheet is generated separating the upper region of subsonic flow from the lower region of supersonic flow. No transmitted wave is resolvable at the upper end of the Mach stem which appears to join smoothly into the bow shock in the vicinity of the sonic line. The upper portion of the bow shock remains symmetrical.

In the high enthalpy case the bow shock remains undisturbed. However, a point of inflection is observed immediately above the intersection point.

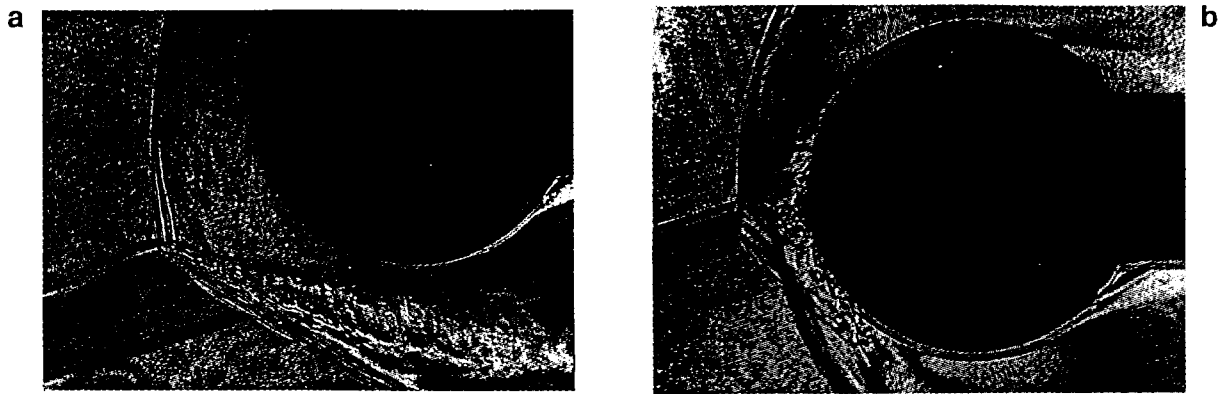


Fig. 3. Differential interferograms of type III interactions.

(a) 3 MJ/kg (b) 12.5 MJ/kg

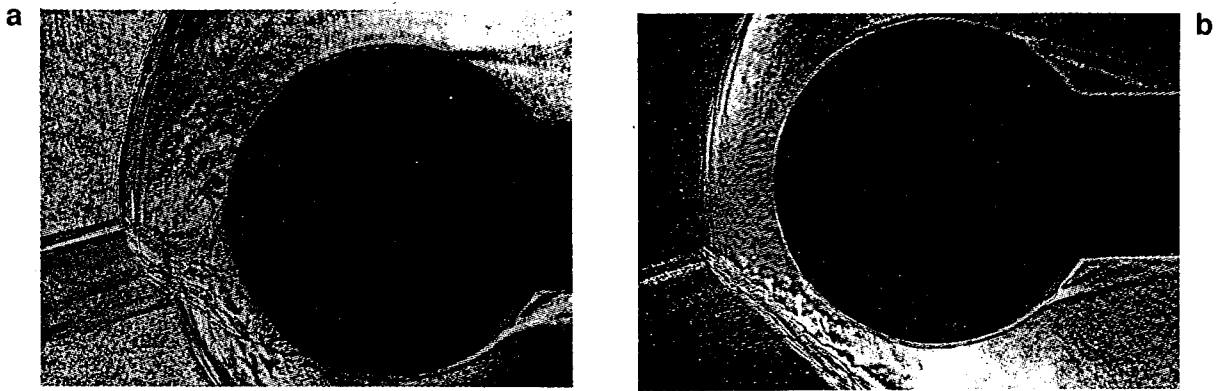


Fig. 4. Differential interferograms of type IV interactions

(a) 3 MJ/kg (b) 12.5 MJ/kg

In the type III experiments (Fig.3) the incident shock wave intersects the bow shock wave in the subsonic region, somewhat below the geometric stagnation point. For both enthalpies the Mach stem has merged with the bow shock wave and the λ -shock pattern is preserved at the intersection point. The influence of the impinging shock wave is now global and both the radius of curvature and the standoff distance of the asymmetrical upper portion of the bow shock has increased to match the λ -shock pattern at the impingement point. Dominated by the inertia of the supersonic stream, the shear layer is deflected only in the immediate vicinity of the cylinder. Generally, the standoff distance decreases with increasing enthalpy and this influences the impingement of the shear layer on the body. In the high enthalpy case, the resulting compression waves, that are observed as a series of nearly vertical white lines below the impingement point, steepen the lower shock. Kinks are observed where these waves meet the supersonic continuation of the bow shock. Weak reflected expansions are observed as horizontal disturbances emanating from the intersection points. Note the analogy between this phenomenon and the mechanism of complex Mach reflection.

When the incident shock wave impinges in the vicinity of the geometrical stagnation point a type IV flow results (Fig.4). The λ -shock pattern is preserved and the supersonic transmitted

portion of the bow shock forms a second inverted λ -shock with the subsonic continuation of the bow shock below the interaction. The flow behind the oblique shock wave connecting the two λ -shocks is supersonic and forms a jet that turns upwards under the action of the pressure gradient produced by the second λ -shock. The strongly curved shear layer generated at the upper λ -shock forms large plumes as it passes above the cylinder. The standoff distance and jet width are reduced in the high enthalpy case but this also depends strongly on the location of the impinging shock. A portion of the supersonic flow is now turned so that it passes above the cylinder and hence the stagnation streamline must pass through the supersonic jet. The stagnation density is higher for streamlines that pass through the supersonic jet than for streamlines that cross the adjacent strong bow shock. The higher density and large unsteady velocity gradients produced by the impingement of the supersonic jet provide the mechanism for local increase of the heat transfer rate.

5. Conclusions

Local analysis about shock wave intersection points in the p - δ plane has been extended to the ideal dissociating gas model. The application of continuation methods to singular solutions illustrated the role of λ -shocks and determined the influence of real gas effects on local analysis. Experiments conducted in a free piston shock tunnel provided insight into real gas effects on the global flow. Generally, real gas effects are seen to increase the range of shock impingement points for which enhanced heating occurs. They further influence the Mach stem form in type II flows, the deflection of the shear layer in type III flows and the length scales associated with the type IV jet.

Acknowledgement

This work was supported by the Air Force Office of Scientific Research under Grant No. F 49620-92-J-0110.

References

- Edney BE (1968a) Effects of shock impingement on the heat transfer around blunt bBodies. AIAA J. 6:15-21
- Edney BE (1968b) Anomalous heat transfer and pressure distributions on blunt bodies at hypersonic speeds in the presence of an impinging shock. FFA-115, The Aeronautical Research Institute of Sweden
- Hornung HG (1986) Regular and Mach reflection of shock waves. Ann. Rev; Fl. Mech. 18:33-58
- Keller HB (1987) Numerical methods in bifurcation problems. Springer-Verlag
- Klopfer GH, Yee HC (1988) Hypersonic shock-on-shock interaction on blunt cowl lips. AIAA Paper 88-0233
- Lighthill MJ (1957) Dynamics of a dissociating gas. Part I. Equilibrium flow. J. Fluid Mechs. 2:1-32
- Wieting AR, Holden MS (1989) Experimental shock wave interference heating on a cylinder at Mach 6 and 8. AIAA J. 27:1557-1565

Shock-interference heating in hypervelocity flow

S. R. Sanderson* and B. Sturtevant
Graduate Aeronautical Laboratories
California Institute of Technology
Pasadena, CA 91125 USA

Abstract: The interaction of a weak oblique shock with the strong bow shock ahead of a blunt body in supersonic flow produces extreme heat-transfer rates and surface pressures. Experiments are conducted in a free-piston shock tunnel to determine the effects of thermochemistry on the problem at high enthalpy. The flow topology is simplified by studying the nominally two-dimensional flow about a cylinder with a coplanar impinging shock wave. Increases in shock-interference heating rates due to real-gas effects are observed to be significantly less than previously expected. A model is discussed that describes the thermochemical processes occurring in the interaction region. The model accurately reproduces the experimental observations.

Key words: Shock interference, Shock impingement, Shock-on-shock

1. Introduction

Although the shock-interference heating problem has been studied extensively in low-enthalpy flows (Edney 1968), the influence of high-enthalpy real-gas effects is poorly understood. Edney (1968) observed and classified six distinct interaction regimes that are known as types I–VI. Severe heating occurs for the type-IV flow where the interaction causes the formation of a supersonic jet that impinges on the surface of the body (Fig. 1). By mapping the shock-wave interactions that occur in the supersonic jet into the pressure-flow deflection angle (p - δ) plane, Edney (1968) studied the variation of the pressure at the jet-impingement point for a perfect gas. It was demonstrated that reductions of the ratio of specific heats, γ , at high enthalpy produce greatly increased surface pressures. The jet-impingement pressure also increases strongly with Mach number. Although the ratio of specific heats is only a crude measure of the influence of equilibrium thermochemistry, the magnitude of the effect predicted by Edney (1968) motivated the current experiments. The objective of the present work was to utilize the capabilities of the GALCIT T5 free-piston

*Present address: GE Corporate Research & Development, P.O. Box 8, Schenectady, NY 12301.

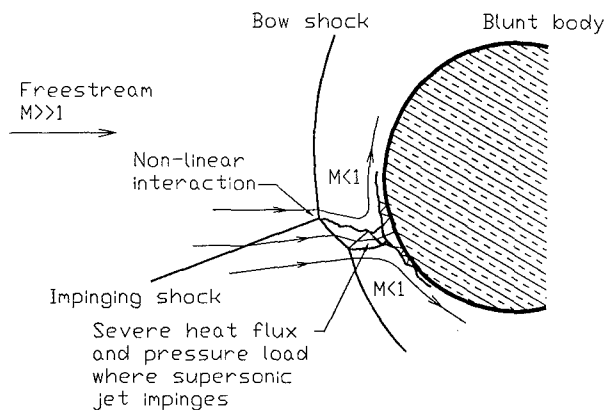


Figure 1. Schematic representation of the type-IV interaction.

shock tunnel to determine the quantitative effects of thermochemistry on the shock-impingement phenomenon.

2. Experimental investigations

The experimental arrangement is shown in Fig. 2. High-temperature and pres-

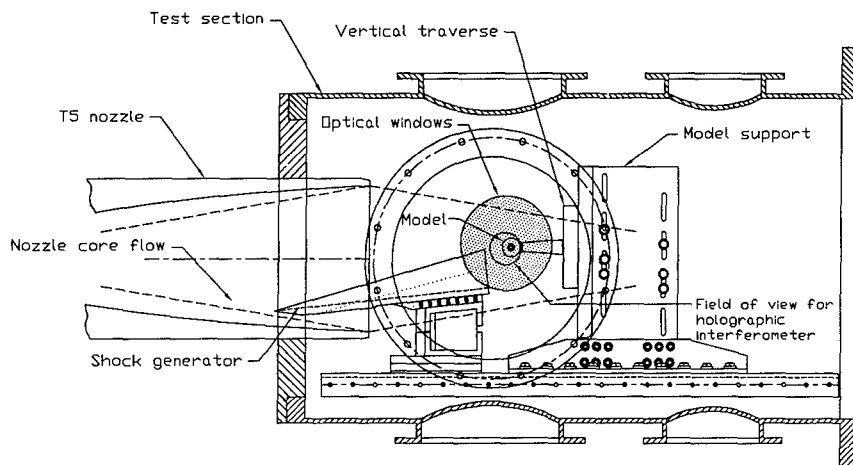


Figure 2. Layout of apparatus in the test section of T5.

sure gas was generated in the nozzle reservoir by the T5 hypervelocity shock tunnel. Nitrogen test gas was used for all experiments (Table 1).

The cylindrical model ($\phi 40 \text{ mm} \times 180 \text{ mm}$) was positioned in the free-jet test section and a large shock generator was partially inserted into the uniform nozzle core flow upstream of the nozzle exit. Holographic interferometry was used to investigate variations in the shock-impingement flow field as the model was vertically translated with respect to the exit of the shock genera-

Table 1. Summary of the free-stream conditions.

Test condition		A	B	C
Test section conditions	Velocity (m/s)	2540	4450	5350
	Density (kg/m ³)	0.0218	0.0155	0.0157
	Pressure (kPa)	1.03	5.48	11.4
	<i>N</i> concentration (mole/kg)	9.9×10^{-5}	6.9×10^{-1}	3.65×10^0
	M_∞	9.9	6.3	5.3
	<i>Re</i> per mm	5500	1600	1350

tor. Surface-junction thermocouple gauges provided time-resolved heat-transfer measurements at 24 circumferential locations around the model forebody. Figure 3 shows a holographic interferogram of a type-IV interaction at the high-



Figure 3. Holographic interferogram of type-IV interaction; condition C.

enthalpy condition, C. Two mutually inverted λ -shocks are observed along with a terminating strong shock and the region of elevated density behind it. The peak heat fluxes recorded during the entire sequence of shots at each test condition are listed in Table 2. The high bandwidth of the heat-flux gauges used for these experiments permitted examination of the temporal characteristics of the heat-transfer signals. Sanderson (1995) discusses observations of coherent unsteady fluctuations of the type-IV jet that are consistent with oscillations observed in recent numerical simulations (Gaitonde 1993, Zhong 1994). Additional data are reported in detail by Sanderson (1995).

Table 2. Measured and predicted peak heat-transfer intensification for type-IV flows.

Test condition		A	B	C
Peak measured $\frac{\dot{q}_{jet}}{\dot{q}_{body}}$	Instantaneous	15.2	10.8	7.9
	100 μs averaged	13.5	7.6	6.0
Predicted $\frac{\dot{q}_{jet}}{\dot{q}_{body}}$	Frozen	14.1	7.2	5.1
	Nonequilibrium	14.1	6.7	4.4
	Equilibrium	14.1	7.4	7.2

The conclusion of the experimental investigation was that the stagnation density and heat-flux intensification decreased at high enthalpy. Care must be exercised in the interpretation of this trend since the Mach number of the flow in T5 decreased as the stagnation enthalpy was increased (Table 1). The net result was that further increases in the large heat fluxes produced by shock impingement, due to real-gas effects, were observed to be much lower than those predicted by existing models (Section 1).

3. Model of the influence of real-gas effects

Modeling of the influence of real-gas effects followed the pattern of the existing perfect-gas model of the type-IV flow (Edney 1968). Normal shock solutions were obtained using the ideal dissociating gas model of Lighthill (1957). The normal shock solutions were extended to oblique waves and p - δ plane methods were used to obtain locally valid solutions for the λ -shock points. These inviscid shock-interaction solutions determine the state of the gas in the type-IV jet. Heating due to impingement of the type-IV jet was modeled using the equilibrium reacting-flow similarity solution of Fay and Riddell (1958). Sanderson (1995) shows that the heat-transfer intensification at the jet-impingement point has the following functional dependence:

$$\frac{\dot{q}_{jet}}{\dot{q}_{body}} \sqrt{\frac{\Delta x}{D} \frac{\zeta_{1body}^2 \zeta_{2body}}{\zeta_{1jet}^2 \zeta_{2jet}}} = \text{func}(P_\infty, H_{0_\infty}, \hat{p}_d, \alpha_\infty, \beta_1). \quad (1)$$

The parameters are $P_\infty = p_\infty / \rho_\infty u_\infty^2 \sim 1/M_\infty^2$, H_{0_∞} is the stagnation enthalpy normalized with respect to the dissociation energy of the gas, \hat{p}_d is the equilibrium constant, α_∞ is the dissociated mass fraction of the free stream, and β_1 is the angle of the impinging wave. The geometrical terms on the left-hand side specialize the result for a particular configuration. The similarity coefficients, ζ , are determined from the work of Fay and Riddell (1958) and the Newtonian solution for the velocity gradient at the outer edge of the boundary layer. The

jet-width-to-body-diameter ratio, $\Delta x/D$, is empirically scaled with the undisturbed shock standoff distance, χ/D , and the divergence angle of the oblique wave and shear layer at the shock-impingement point, δ ;

$$\frac{\Delta x}{D} = \frac{\chi}{D} \sin \delta. \quad (2)$$

All of the quantities appearing in Eqs. (1) and (2) may be predicted a priori.

The behavior of the local solution (1) with stagnation enthalpy, $H_{0\infty}$, is illustrated in Fig. 4 for typical values of the remaining parameters. Three solutions are obtained using different thermodynamic models to demonstrate the influence of nonequilibrium thermochemistry. The dotted lines represent chemically frozen solutions that apply when the reaction rates are slow with respect to the rate of flow over the body. The dash-dot curves are equilibrium solutions that apply when the reaction rates are fast and are obtained using the Lighthill (1957) model for the shock-jump computations. The dashed curves represent an approximate nonequilibrium solution that is motivated by the disparate shock strengths produced at the λ -points. The weak oblique waves in the supersonic jet are assumed to remain frozen whilst the strong bow shock and terminating jet shock relax to equilibrium. The validity of the nonequilibrium approximation is assessed by computing the reaction rates (Freeman 1958) immediately downstream of the translational discontinuities. Figure 4 shows that equilibrium real-gas effects increase the heat-transfer intensification with respect to the frozen solution. This occurs because of the increased density ratio across the weak oblique jet shocks due to dissociation. Dissociation across the jet shock waves is precluded in the nonequilibrium approximation and the heat-transfer intensification decreases slightly with respect to the frozen solution. Within the scope of the approximation, non-monotonic behavior with the reaction rate is indicated. The significance of real-gas effects declines at higher Mach numbers because the oblique jet shocks become weaker relative to the bow shock and terminating jet shock. This causes reduced dissociation levels and reaction rates in the supersonic jet. Heating rates initially increase with impinging shock strength before reaching a maximum for modest-strength waves. Further analysis (Sanderson 1995) demonstrates that the relative influence of real-gas effects is minimized at this maximum heating condition.

Specific predictions of the model for the test conditions listed in Table 1 are compared with the experimental data in Table 2. The extent of chemical reactions at the low-enthalpy condition A was negligible and so only the frozen solution is shown. Reaction rates for condition C were sufficiently high that departures from equilibrium were expected to be slight. The calculated values accurately reproduce the experimental heat-transfer measurements.

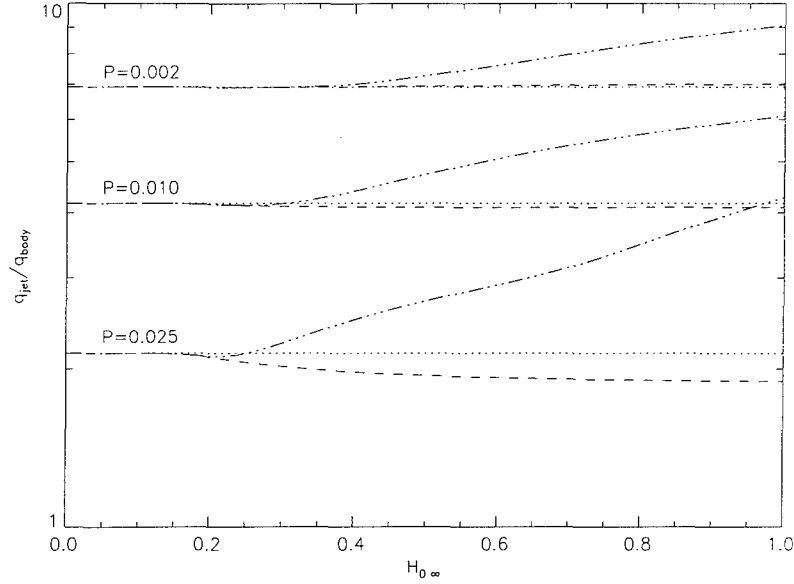


Figure 4. Influence of dimensionless stagnation enthalpy, $H_{0\infty}$, Mach number, $\sim 1/P_{\infty}^{0.5}$, and reaction rate on type-IV heat-transfer intensification, $\frac{q_{jet}}{q_{body}} (\Delta x \zeta_{1body}^2 \zeta_{2body} / D \zeta_{1jet}^2 \zeta_{2jet})^{0.5}$. The parameters are $\hat{\rho}_d = 1 \times 10^7$, $\alpha_{\infty} = 0$, and $\beta_1 = 16^\circ$.

Acknowledgement. This work was supported by the Air Force Office of Scientific Research under Grant Nos. F 49620-92-J-0110 and F 49620-93-1-0338.

References

- Edney BE (1968) Anomalous Heat Transfer and Pressure Distributions on Blunt Bodies at Hypersonic Speeds in the Presence of an Impinging Shock, FFA Report 115.
- Fay JA, Riddell FR (1958) Theory of stagnation point heat transfer in dissociated air. *Journal of the Aeronautical Sciences* 25:73.
- Freeman NC (1958) Non-equilibrium flow of an ideal dissociating gas. *J Fl Mech* 4:407.
- Gaitonde D (1993) Calculations on Unsteady Type IV Interaction at Mach 8, Wright Laboratory, WL-TR-93-3002.
- Lighthill MJ (1957) Dynamics of a dissociating gas. Part I. Equilibrium flow. *J Fl Mech* 2:1.
- Sanderson SR (1995) Shock Wave Interaction in Hypervelocity Flow, Ph.D. Thesis, California Institute of Technology.
- Zhong X (1994) Application of essentially non-oscillatory schemes to unsteady hypersonic shock-shock interference heating problems. *AIAA J* 32:1606.

Appendix B

Ph. D. Thesis of Chih-Yung Wen, see separately bound volume

Appendix C

Ph. D. Thesis of Simon Sanderson, see separately bound volume